Opto-Electronic Advances

CN 51-1781/TN   ISSN (Print) 2096-4579   ISSN (Online) 2097-3993

Overcoming challenges in InP-based quantum dots: from nucleation mechanisms to high-performance quantum dot light-emitting diodes

Yangyang Bian, Qian Li, Fei Chen*, Chunhe Yang*, Huaibin Shen and Aiwei Tang*

Citation: Bian YY, Li Q, Chen F, Yang CH, , Tang AW. Overcoming challenges in InP-based quantum dots: from nucleation mechanisms to high-performance quantum dot light-emitting diodes. *Opto-Electron Adv* **9**, 250270 (2026).

https://doi.org/10.29026/oea.2026.250270

Received: 10 October 2025;   Accepted: 16 December 2025;   Published online: 27 February 2026

OEA | Opto-Electronic Advances

Review

March 2026, Vol. 9, No. 3

Overcoming challenges in InP-based quantum dots: from nucleation mechanisms to high-performance quantum dot light-emitting diodes

Yangyang Bian[1], Qian Li[1], Fei Chen[2]*, Chunhe Yang[1]*, Huaibin Shen[2] and Aiwei Tang[1]*

Abstract: Indium phosphide-based quantum dots (InP-based QDs) have emerged as promising candidates for next-generation display and optoelectronic technologies, offering exceptional photoluminescent (PL) properties including high efficiency, narrow emission spectra, and precisely tunable wavelengths. Nevertheless, their widespread commercialization encounters substantial obstacles, primarily stemming from persistent challenges in synthetic control and material processing. Critical performance parameters—including photoluminescence quantum yield (PL QY, currently<90% for most systems), emission linewidth (typically>35 nm) as well as external quantum efficiency (EQE) and operational stability of device—continue to show only incremental improvements, highlighting the urgent need for fundamental breakthroughs in QDs synthesis, surface engineering and device optimization. This review systematically examines the nucleation mechanisms governing InP core formation and outlines key strategies for optimizing InP-based core/shell QDs. Furthermore, we present a comprehensive analysis of recent breakthroughs in red, green, and blue-emitting InP-based QD light-emitting diodes (QLEDs) development, focusing on modulation of charge transport engineering and suppression of charge leakage. Finally, we critically evaluate the remaining commercialization challenges and future prospects for InP-based QLEDs in next-generation display and optoelectronic technologies, outlining potential pathways for overcoming current limitations.

Keywords: indium phosphide; quantum dot; nucleation mechanism; core/shell engineering; ligand engineering; quantum dot light-emitting diode

DOI: 10.29026/oea.2026.250270 | CSTR: 32247.14.oea.2026.250270

Citation: Bian YY, Li Q, Chen F et al. Overcoming challenges in InP-based quantum dots: from nucleation mechanisms to high-performance quantum dot light-emitting diodes. *Opto-Electron Adv* **9**, 250270 (2026).

1 Introduction

In recognition of the seminal contributions to the "discovery and synthesis of quantum dots (QDs)," Bawendi, Brus, and Ekimov were jointly awarded the 2023 Nobel Prize in Chemistry. QDs, also known as semiconductor nanocrystals, exhibit unique quantum confinement effects and size-tunable optical/electronic properties that distinguish them from both traditional molecules and bulk materials[1−5]. At present, significant progress has been made in fundamental QD research, focusing on facile and economical synthesis approaches. Their exceptional solution processability allows seamless integration with various matrices while preserving high charge carrier mobility, making them ideal for next-generation optoelectronic applications[6−10]. Following Samsung's landmark development of a low-power, high-luminance QD display prototype in 2012, industry leaders like Samsung have now successfully developed "quantum dot light-emitting diodes (QLEDs)" television. In these displays, QDs serve as highly efficient emitters for the green and red subpixels, delivering enhanced color vibrancy at competitive price points.

Currently, II-VI and IV-VI semiconductor QDs, along with metal halide perovskites ($CsPbX_3$, where X is a halide: Cl, Br, or I), exhibit outstanding photoluminescent (PL) properties, especially in terms of their full-width half maximum (FWHM) and photoluminescence quantum yield

Received: 10 October 2025

Accepted: 16 December 2025

[1]Key Laboratory of Luminescence and Optical Information, Ministry of Education, School of Physical Science and Engineering, Beijing Jiaotong University, Beijing 100044, China; [2]Key Laboratory for Special Functional Materials of Ministry of Education, National & Local Joint Engineering Research Center for High-efficiency Display and Lighting Technology, School of Nanoscience and Materials Engineering, Henan University, Kaifeng 475004, China.

*Correspondence: F Chen, E-mail: chenfei.henu@henu.edu.cn; CH Yang, E-mail: chy@bjtu.edu.cn;
AW Tang, E-mail: awtang@bjtu.edu.cn

(PL QY)[11−16]. Significant progress has also been made in red, green, and blue-emitting Cd-based QLEDs, with external quantum efficiencies (EQEs) exceeding 20%[11−13]. These devices exhibit impressive operational stability, particularly for red and green-emitting devices, which demonstrate T_{95} (time for the luminance decreasing by 95%) @1,000 cd·m^{-2} > 72,900 h and 29,100 h, respectively[17,18]. These performance parameters approach or even meet the stringent requirements for commercial display technologies. However, the widespread adoption of these QDs faces substantial challenges due to the presence of heavy metals such as Cd and Pb, which pose significant risks to human health and the environment. The European Union's restriction of the Hazardous Substances (RoHS) directive has further limited their commercial application. Therefore, the development of high-performance, environmentally friendly QDs is crucial for next-generation energy, environmental, and biomedical technologies.

Currently, numerous non-toxic QD materials have been developed, including lead-free perovskites[19,20], copper indium sulfide ($CuInS_2$)-based QDs[21,22], zinc selenide (ZnSe)-based QDs[23,24], and indium phosphide (InP)-based QDs[25−28]. However, each material system presents distinct challenges: lead-free perovskites suffer from poor environmental stability, leading to rapid efficiency degradation[29]; $CuInS_2$-based QDs exhibit broad emission spectra due to the defects states arising from cation disorder[21]; and ZnSe-based QDs, while exhibiting excellent performance in the blue-to-violet emission range, are constrained by their wide bandgap for broader display and lighting applications[30]. Among these environmentally friendly alternatives, InP-based QDs stand out with exceptional structural and optical advantages. InP possesses a small effective electron mass (0.08 m_0) and a large dielectric constant (12.9), facilitating strong delocalization of electrons and yielding a large exciton Bohr radius of approximately 10 nm[31−33]. Meanwhile, with a bulk bandgap of 1.35 eV, InP-based QDs can be tuned to emit across a wide spectral range, from near-infrared (~750 nm) to blue (~480 nm), by precisely controlling their core size[33]. The high covalency of the In-P bonds also provides superior optical stability compared to II-VI QDs that primarily feature ionic bonding[34−36], ensuring robust resistance to degradation under sustained excitation.

Since the first synthesis of InP-based QDs and systematic investigation of their optical properties by Micic et al. in 1994[37], followed by the groundbreaking demonstration of InP-based QLEDs by Li et al. in 2011[38]—which ingeniously adapted the structural design of Cd-based QLEDs—InP has gradually emerged as a promising material for next-generation optoelectronic applications. Over the past three decades, significant efforts have been devoted to developing various precursors and synthetic strategies for high-quality InP cores, alongside extensive research into lattice-matched shell materials for effective surface passivation and enhanced optical properties[25−28,39−42]. These concerted efforts have yielded extraordinary achievements: red and green-emitting InP-based QDs now exhibit near-unity PL QY, outstanding narrow emission linewidths (FWHM <36 nm), and exceptional photostability[25,26]. Capitalizing on these material breakthroughs and concurrent advancements in device architecture engineering, state-of-the-art red and green-emitting InP-based QLEDs have achieved remarkable performance, including EQE exceeding 20%, operational lifetimes (T_{95}@1,000 cd·m^{-2}) surpassing 1,000 h, and peak luminance values reaching 120,000 cd·m^{-2} [26,28]. While their overall performance remains slightly inferior to Cd-based counterparts, particularly in the blue-emitting QLEDs[43], the rapid progress in InP-based technologies underscores their tremendous potential as environmentally sustainable alternatives for future display and solid-state lighting applications.

In this review, we systematically discuss the key strategies employed in high-performance InP-based QDs and their application in QLEDs. We first explore the nucleation mechanisms of InP cores, covering classical nucleation theory, emerging non-classical nucleation pathways, and strategies for decoupling the nucleation and growth stages. Subsequently, we focus on optimization methodologies for enhancing the quality of the InP cores, emphasizing the critical roles of physical size sorting, zinc salts, and core surface treatment in enhancing crystallinity and monodispersity. Furthermore, we provide a detailed discussion of the key elements of core/shell engineering. This includes the selection and optimization of shell structure to balance lattice mismatch, precise shell thickness regulation for optimal exciton confinement and photoluminescence, and kinetic regulation of shell growth to realize defect-free surface passivation. Additionally, the critical impact of ligand engineering in modulating QD dispersibility, stability, and charge transport properties within devices is highlighted and analyzed. Finally, we comprehensively review the recent advances in InP-based QLEDs, outlining the direction for the future development of high-performance, stable InP-based QLEDs. We firmly believe that with sustained efforts, the application of efficient and stable heavy-metal-free QLEDs in displays will soon transition from laboratory breakthroughs to large-scale commercial implementation.

2 Development challenges of InP-based core/shell QDs

InP-based QDs are considered ideal candidates for display and lighting technologies due to their eco-friendly composition and outstanding optoelectronic properties[25,26]. However, their development has faced substantial challenges, including inconsistent core quality, interfacial strain in core/shell structures, and inefficient surface passivation[27,28,39]. Through sustained research efforts, significant progress has been made in refining InP core synthesis, optimizing shell architectures, and advancing ligand engineering[40–42]. These breakthroughs have dramatically improved the performance of InP-based QDs, accelerating their commercialization in high-end applications such as QLED displays. In the following sections, we systematically analyze the key challenges in InP-based QD development and present the most effective strategies to address them.

2.1 Nucleation mechanism for InP cores

2.1.1 Classical nucleation theory

The quality of InP core has long been recognized as a crucial factor affecting the performance of InP-based core/shell QDs and their corresponding QLEDs. Among the key challenges in synthesizing high-quality InP-based QDs, achieving cores with uniform particle size distribution is of utmost importance[25,28,39,40]. To design a rational and feasible synthesis strategy, it is essential to understand the nucleation kinetics and the underlying chemical reactions involved in the process. According to LaMer's nucleation theory (Fig. 1(a)), burst nucleation and diffusion-controlled growth are the primary factors governing particle size distribution[44]. In homogeneous nucleation, precursor conversion generally occurs before nanocrystal nucleation and growth. As a result, burst nucleation occurs once the monomer concentration reaches a critical level. However, nucleation and growth often proceed simultaneously. A high supersaturation level promotes both uniform nucleation and crystal growth. Consequently, the initially formed cores grow faster and larger compared to those formed later, resulting in a broad size distribution[45]. To obtain monodisperse colloidal QDs, it is crucial to minimize the duration of the nucleation phase, ensuring that all cores undergo nearly identical growth trajectories during crystallization. Over time, this approach leads to a narrowing of the size distribution, a phenomenon known as size focusing[46]. Under diffusion-controlled growth conditions, the system's behavior is highly dependent on monomer concentration relative to particle solubility. When monomer concentration substantially exceeds solubility, the solute rapidly diffuses to the nanocrystal surface and precipitates. Conversely, sub-solubility monomer concentrations induce mass transfer reversal and subsequent crystal dissolution. According to the Gibbs-Thomson relationship, smaller particles possess higher chemical potential. At lower monomer concentrations, the dissolution rate of smaller cores surpass their

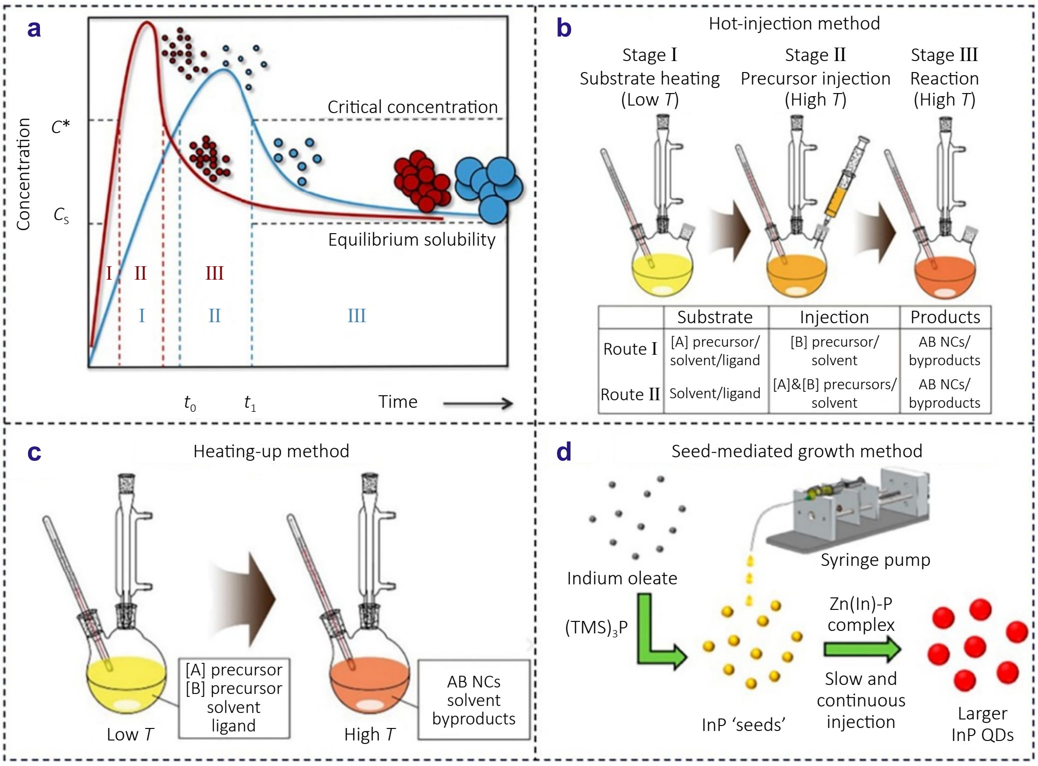

	Substrate	Injection	Products
Route I	[A] precursor/ solvent/ligand	[B] precursor/ solvent	AB NCs/ byproducts
Route II	Solvent/ligand	[A]&[B] precursors/ solvent	AB NCs/ byproducts

[A] precursor
[B] precursor
solvent
ligand

AB NCs
solvent
byproducts

Fig. 1 | (a) The preparation of monodisperse particles is divided into the following three stages. (I) Precursor conversion and monomer concentration increase, exceeding the critical concentration (C^*); (II) nucleation; (III) nanocrystal growth from solution when the monomer concentration is supersaturated ($C^*>C>C_S$). A high precursor concentration (red curve) yields smaller final particle sizes than a low precursor concentration (blue curve). (b) Schematic diagram of QD synthesis by the hot-injection method. (c) Schematic diagram of QD synthesis by the heating-up method. (d) Schematic diagram of larger InP-based QD synthesis by the seed-mediated growth method. Figure reproduced with permission from: (a) ref.[44], American Chemical Society; (b) ref.[49], John Wiley & Sons; (c) ref.[49], John Wiley & Sons; (d) ref.[40], American Chemical Society.

precipitation rate, while larger cores exhibit greater stability and continue growing by absorbing monomers from dissolving smaller cores. This process, known as Ostwald ripening, reduces the total number of core and monomer concentration while increasing the average particle size[47]. By carefully controlling these thermodynamic and kinetic factors, a more uniform size distribution of InP cores can be achieved, ultimately enhancing the performance of InP-based core/shell QDs.

2.1.2 The strategy to separate the nucleation and growth stages

2.1.2.1 Selection of synthesis methods

From the discussion above, it is evident that separating the nucleation and growth stages is critical for obtaining monodisperse InP cores. Significant efforts have been devoted to achieving this goal, and various synthetic strategies for preparing highly uniform nanocrystals have been developed[28,39,40,48]. One representative approach is the hot-injection method, which typically involves rapidly injecting precursor [B] into a hot reaction solution containing precursor [A] (Method I), or simultaneously injecting both precursors [A] and [B] into a hot solvent (Method II)[49] (Fig. 1(b)). This approach operates on the principle of inducing instantaneous monomer supersaturation through rapid precursor injection, which triggers burst nucleation[50]. The subsequent rapid depletion of monomers reduces the supersaturation level, creating conditions favorable for size-focusing growth. Since the thermodynamic energy barrier for homogeneous nucleation is significantly higher than that for subsequent growth, nanocrystals begin to grow under size-focusing conditions. However, when the monomer concentration decreases below a critical threshold, Ostwald ripening becomes dominant, resulting in broadening of the size distribution. Overall, the sudden induction of high initial supersaturation provides the necessary kinetic driving force for burst nucleation and subsequent size focusing in hot-injection synthesis[45]. Pioneering work by the research groups of Peng and Prasad demonstrated the application of Method I for InP-based QDs synthesis. In their approach, tris(trimethylsilyl)phosphine ($P(SiMe_3)_3$) was injected into an octadecene (ODE) solution containing indium acetate and fatty acids. Through systematic experimentation, they identified palmitic acid and myristic acid as optimal ligands for both nucleation and growth[51,52]. While Method I has seen substantial progress, the development of Method II has been relatively slow, possibly due to the poor room-temperature solubility of In precursors in nonpolar solvents. Recently, Peng Xiaogang's group addressed this challenge by demonstrating that adding an equimolar amount of trioctylphosphine (TOP) to an ODE solution of indium stearate ($In(St)_3$) dramatically enhances its solubility. When the resulting $In(TOP)(St)_3$ complex was employed in hot-injection synthesis, QDs with well-defined absorption peaks and a narrow size distribution were successfully obtained[53].

The heating-up method is another approach for synthesizing highly uniform nanocrystals. In this method, the reaction mixture is first prepared at room temperature and then gradually heated to the required reaction temperature for nanocrystal formation[49] (Fig. 1(c)). During the initial nucleation stage, the monomer concentration increases without nucleation due to the presence of a nucleation energy barrier[54]. Once a critical temperature and monomer concentration are reached, nucleation occurs. As monomers are consumed, nucleation ceases, leaving only the growth phase to proceed. This growth regime enables size focusing, leading to rapid narrowing of the size distribution. Once the monomers are nearly depleted, Ostwald ripening dominates the remaining reaction time[45]. Due to the involved complex reaction processes during heating, key experimental variables, such as precursor composition, reaction temperature, and heating rate, must be carefully optimized to effectively separate the nucleation and growth stages[54]. To decouple these two stages, Taylor et al. proposed a staged heating protocol: the reaction solution is slowly heated from room temperature to 130 °C to prioritize nucleation, followed by a temperature ramp to 300 °C to control nanocrystal growth[39]. This innovative approach significantly suppresses Ostwald ripening. Combined with optimizing the In/P molar ratio (1.5) to regulate reaction kinetics, the method achieves an effective separation of nucleation and growth, thereby effectively suppressing Ostwald ripening. Ultimately, this strategy yields a highly monodisperse InP cores with an exceptionally narrow size distribution. Currently, both the heating-up and hot-injection methods can produce monodisperse nanocrystals with a relative standard deviation (σ_r) of less than 10%[26,39,52,55], where size focusing is driven by the controlled nucleation and growth conditions.

The seed-mediated growth method offers a promising alternative for the preparation of monodisperse InP cores[25,28,40,48]. Unlike homogeneous nucleation in the hot-injection and heating-up methods, this approach employs heterogeneous nucleation by depositing the target material (monomers or ions) onto pre-synthesized small nanoparticle seeds[48,56,57]. This mechanism circumvents the nucleation energy barrier, thereby enabling highly controllable nanocrystal growth and effective size focusing[54]. However, secondary nucleation and Ostwald ripening during growth can still introduce size heterogeneity if not properly suppressed. To mitigate these effects and improve diffusion kinetics, precise optimization of reaction parameters, such as reaction volume, precursor concentration, and precursor injection rate, must be carefully optimized[58,59]. Conventional synthesis methods often face challenges in producing large InP cores with narrow size distributions, particularly due to the high reactivity of P precursors[60–62]. These limitations typically result in red-emitting InP-based QDs with FWHM values exceeding 60 nm[51,52]. The seed-mediated growth method not only ensures a narrow FWHM but also overcomes the size limitations (<5 nm) often encountered in conventional solution-phase nanocrystal growth due to limited monomer reactivity[58]. A notable example of this approach is the two-step seed-mediated growth strategy developed by Ramasamy et al.[40] (Fig. 1(d)). In their method, Zn(In)-P complexes were injected into pre-synthesized InP-based QDs with a narrow size distribution (initial absorption peak at 490 nm). Through this approach, they successfully shifted the absorption peak from 490 nm to 650 nm, corresponding to an increase in particle size from 1.9 nm to 4.5 nm. Subsequent coating of these InP cores with ZnSe/ZnS shells yielded emission spectra with an FWHM below 40 nm across all wavelengths. Therefore, by slowly injecting precursors onto highly dispersed small InP seeds, seed-mediated growth provides precise control over InP core growth and size focusing, making it a highly effective strategy for synthesizing large InP cores with superior optical properties.

2.1.2.2 Choice of phosphorus source

Currently, InP-based QDs face several key performance challenges, particularly in color purity, where they significantly lag behind CdSe-based QDs[11−13,26,28,43]. However, Cui et al. employed solution-based photon-correlation Fourier spectroscopy to reveal that the intrinsic emission linewidth (the linewidth of an individual QD) of InP-based QDs is comparable to that of CdSe-based QDs[63]. This indicates that InP-based QDs inherently possess the capability to achieve a similarly narrow emission linewidth. Nevertheless, the ensemble emission linewidth of InP-based QDs remains substantially broader than that of CdSe-based QDs in practice. This discrepancy primarily stems from deviations in the nucleation and growth mechanisms of InP-based QDs from classical pathways, resulting in heterogeneous size distributions[62,64]. The underlying mechanisms can be systematically explained through two critical aspects. Firstly, the chemical bonds of III-V semiconductors exhibit high covalency (e.g., the covalent component of In-P bonds exceeds 70%), significantly greater than those in II-VI semiconductors like CdSe[34]. This strong covalent character elevates the activation energy required for the commonly used precursor dissociation into monomers. For instance, In precursors require prolonged reaction times at high temperatures (>280 °C) to initiate nucleation, whereas CdSe precursors can rapidly dissociate at ~240 °C[51,65,66]. Such thermodynamic constraints prevent the strict temporal separation between nucleation and growth phases essential for achieving LaMer-type growth in the synthesis of InP-based QDs. Second, the consumption rate of precursor molecules becomes excessively rapid at elevated temperatures[60−62]. As demonstrated by Allen et al., $P(SiMe_3)_3$—the most commonly used P precursor —rapidly depletes at high temperatures, leaving insufficient residual precursor available during the critical growth phase[62]. In this scenario, growth can only proceed via Ostwald ripening, leading to extremely poor size monodispersity of the QDs.

In current high-yield synthetic approaches, $P(SiMe_3)_3$ paired with indium carboxylates has emerged as the predominant precursor combination[25−28]. Despite the various challenges mentioned above, Taylor et al. made significant progress by employing zinc acetate ($Zn(Ac)_2$) to precisely control nucleation and growth kinetics[39]. Additionally, by employing strain-minimized homogeneous shells to enhance monodispersity and optimizing ligand exchange protocols for improved surface passivation, they ultimately achieved exceptional size uniformity. Through further rigorous size-selection techniques, they achieved InP-based QDs with a remarkably narrow FWHM of ~33 nm, representing the best monochromaticity achieved for InP-based QDs to date (Fig. 2(a)). Their systematic investigation further revealed that the concentration of P precursors also plays a critical role in size distribution, with In:P ratios of 0.5 or 1 being widely used in the literature. Interestingly, the addition of TOP as a co-precursor with $P(SiMe_3)_3$ was found to further enhance size uniformity. This is because TOP, as a strong coordinating ligand, can not only modulate reaction kinetics by slowing nucleation rates, but also provide improved surface stabilization during growth[27,39,53,67]. These findings establish important design principles for achieving narrow size distributions in the synthesis of InP-based QDs.

Before the research of Allen and Bawendi[62], several alternative P precursors to $P(SiMe_3)_3$ had been investigated to reduce synthesis costs, including sodium phosphide (Na_3P)[68], phosphorus trichloride (PCl_3)[69], phosphine (PH_3)[70] and white phosphorus (P_4)[71,72]. Although InP-based QDs synthesized using Na_3P precursor exhibited distinct optical absorption spectra, their particle size and bandgap remained challenging to control[68]. The low-temperature synthesis employing PCl_3 and indium acetate mixed solution with $LiBHEt_3$ as a reducing agent could produce size-tunable InP-based QDs, but their size distribution still failed to match the exceptional monodispersity achieved with $P(SiMe_3)_3$[69]. Alternative studies demonstrated that in situ generation of PH_3 gas through the reaction of M_3P_2 (M=Ca or Zn) with mineral acids (sulfuric acid (H_2SO_4) or hydrochloric acid (HCl)) could provide a more economical P source. By bubbling generated PH_3 into an indium acetate and myristic acid-containing ODE solution, InP-based QDs with emission peaks ranging from 570 to 720 nm were obtained[70]. However, this approach faced limitations, including the high toxicity of PH_3, operational complexity, and potential constraints on QD performance. In another strategy, when using P_4 as the simplest phosphorus source, syntheses were typically performed under hydrothermal or solvothermal conditions[71,72]. However, it typically yielded polydisperse, aggregated InP-based QDs of poor quality.

The reactivity of P precursor plays a pivotal role in the synthesis of high-quality InP-based QDs, driving significant research efforts toward developing less reactive P precursors. Notably, the thermal and air stability of Group IVA elements exhibits a marked increase along the series from silicon to germanium to tin[73]. In a seminal study, Bawendi

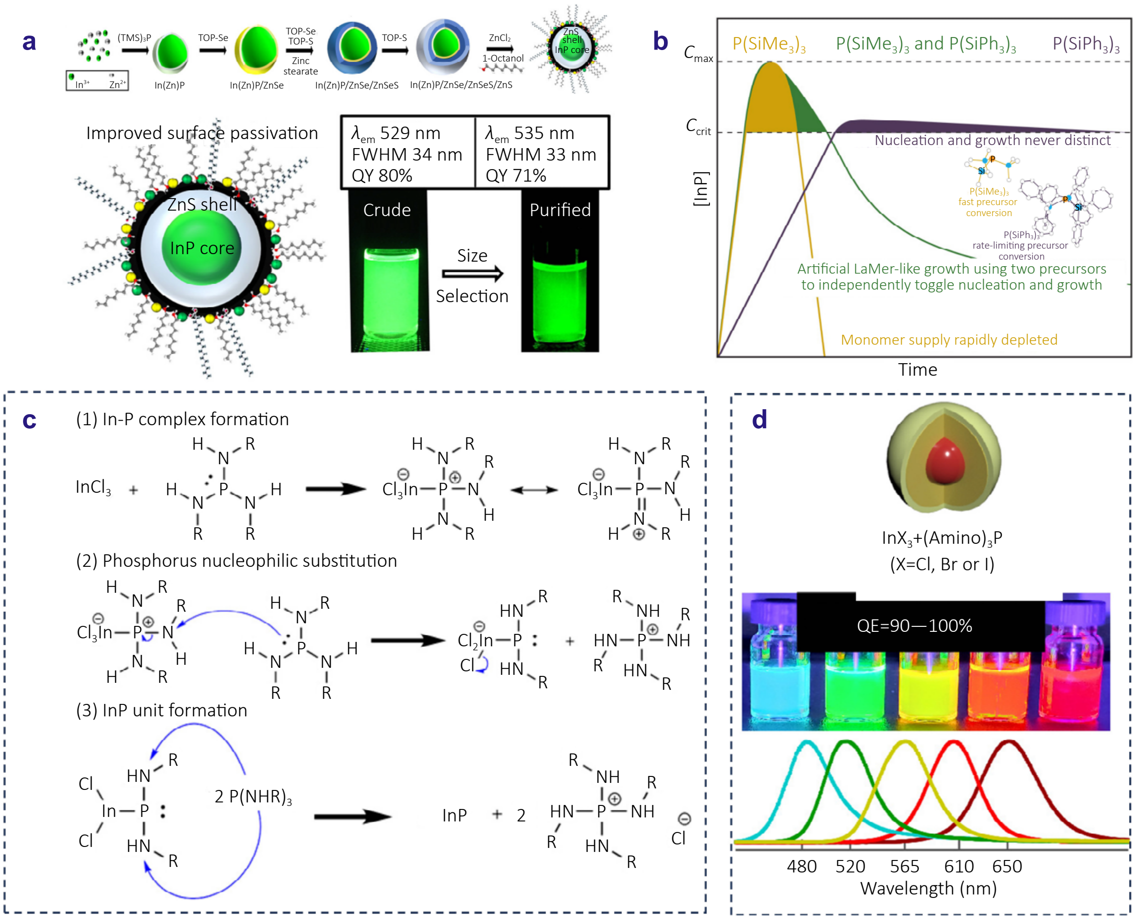

Fig. 2 | (a) Schematic diagram of synthesizing InP-based QDs using $P(SiMe_3)_3$. (b) LaMer-like growth for synthesizing InP cores using two P precursors with different reactivities. (c) Formation mechanism of InP using aminophosphine as P precursor. (d) Schematic diagram of preparing InP-based QDs with different emission peaks using different halogen species and aminophosphine. Figure reproduced with permission from: (a) ref.[39], (b) ref.[75], (c) ref.[85], (d) ref.[77], American Chemical Society.

and colleagues demonstrated an effective strategy to mitigate precursor reactivity by utilizing P precursors devoid of unstable Si-P bonds[61]. Their experimental results revealed that $P(GeMe_3)_3$ exhibited a fourfold slower reaction rate compared to $P(SiMe_3)_3$, while simultaneously yielding nanoparticles with an superior size distribution. Nevertheless, achieving optimal size focusing necessitated reaction temperatures that exceeded the boiling points of conventional solvents, presenting an additional synthetic challenge. To achieve more precise control over precursor reactivity, Joung et al. developed an alternative strategy involving the replacement of the methyl groups in $P(SiMe_3)_3$ with sterically hindered tert-butyl groups to moderate the reaction kinetics[74]. Additionally, Gary et al. employed a mixed-precursor strategy where $P(SiPh_3)_3$ acted as a monomer reservoir, while $P(SiMe_3)_3$ facilitated rapid nucleation in a single injection[75] (Fig. 2(b)). This innovative method created a synergistic system that allowed independent tuning of nucleation and growth through precise stoichiometric control. Surprisingly, despite these sophisticated modifications, the final QD size distribution showed no substantial improvement over conventional $P(SiMe_3)_3$-based synthesis.

In recent years, aminophosphines have gradually become an ideal alternative to $P(SiMe_3)_3$ due to their low cost and high stability[67,76–80]. The synthesis of InP-based QDs using tris(dimethylamino)phosphine ($P(NMe_2)_3$) has attracted growing research interest[41,67,76,78–80]. A significant advancement was made in 2004 by Maenosono and co-workers, who developed a novel synthetic route involving the thermal decomposition of indium trichloride and $P(NMe_2)_3$ in a mixture of TOP and trioctylphosphine oxide (TOPO)[81]. This method offers notable advantages over previous synthesis protocols, including enhanced safety and cost-effectiveness. Unlike conventional strategies that rely on controlling precursor concentration, ligand concentration, or chain length to regulate the size of QDs[50,51,82], this innovative route enables effective size tuning through simple variation of the halide precursor (InX_3 or ZnX_2, where X = Cl, Br, or I)[77,83]. Additionally, the use of halides with higher atomic numbers tends to yield smaller QDs. This phenomenon may be attributed to the decreased adsorption capacity of larger halide ions on the QD surface, which consequently reduces the surface reaction rate during particle growth[83].

Notably, reactions almost entirely fail when indium acetate serves as the precursor or when ODE is employed as the solvent. Extensive studies have shown that InP can only be successfully synthesized when the solvent is a primary amine[64,77,83−85]. Tessier et al. proposed a transamination reaction, further supporting that primary amines not only act as solvents or ligands but also play a crucial role in the precursor chemistry[85]. Furthermore, it was found that when the molar ratio of amido-phosphine to InX_3 is 3.6 or higher, the chemical yield can reach 100%[64,83,85]. Excess aminophosphine plays a dual role in the reaction, serving as both the P precursor and the reducing agent for P(V) phosphine salts[85]. The specific reaction mechanism is as follows (Fig. 2(c)): 1) One molecule of $P(NHR)_3$ reacts with $InCl_3$ to form a complex; 2) The positively charged complex undergoes a nucleophilic substitution with another molecule of $P(NHR)_3$, forming an InP intermediate; 3) Two $P(NHR)_3$ molecules reduce the P in the intermediate, yielding InP. The steric hindrance of bulky amines hinders complex formation and subsequent nucleophilic substitution, so the solvent must be a primary amine. Compared to other P precursors, the optical properties of InP-based QDs synthesized from $P(NMe_2)_3$ are closest to those made with high-quality $P(SiMe_3)_3$[26,41]. As a representative case, Avermaet et al. demonstrated aminophosphine-derived InP-based QDs exhibiting tunable emission across 480–630 nm while maintaining near-unity PL QY (>90%)[77] (Fig. 2(d)). Despite these advances, key performance metrics —particularly emission linewidth —require further enhancement[25,86]. This may be attributed to the need for further optimization in nucleation quality control (e.g., particle size distribution) with $P(NMe_2)_3$[64]. Nevertheless, through material design and process innovation, the performance gap between $P(NMe_2)_3$ and $P(SiMe_3)_3$ routes is gradually narrowing, demonstrating greater potential for future applications.

2.1.3 Emerging nucleation mechanism

Despite significant advancements in precursor reactivity that have improved the quality of InP-based QDs, achieving monodispersity remains challenging[60,61,74,75]. This is because many synthesis modifications still deviate from the classical LaMer model. A breakthrough occurred in 2009 when Xie et al. first synthesized InP magic-sized clusters (MSCs) through the reaction of indium carboxylate, corresponding carboxylic acid, and $P(SiMe_3)_3$[87,88]. These clusters were found to maintain their morphology over a specific temperature range, indicating that the nanocrystal growth mechanisms are not solely governed by thermodynamic favorability during nucleation[65,88−90]. Instead, under conditions of high reactivity and solute concentration, MSCs can form directly without overcoming a significant thermodynamic barrier[88,91]. The existence of these InP intermediate clusters was later confirmed by Gary et al. through X-ray crystallography. They identified a cluster with the stoichiometry $In_{37}P_{20}(O_2CR)_{51}$, in which a $[In_{21}P_{20}]^{3+}$ core is passivated by 16 In^{3+} ions and 51 carboxylate ligands, resulting in an overall neutral structure[92,93]. These clusters, typically smaller than 2 nm, exhibit a short-wavelength lowest-energy electronic transition (LEET) at 386 nm[65,94]. Given that the final product of a complete reaction is the InP nanocrystal, these MSCs can act as excellent single-source precursors for the generation of highly monodisperse InP cores[40,65]. The nucleation mechanism of InP-based QDs involves two distinct pathways: either through the dissolution of MSCs back into monomers for secondary nucleation, or via the direct aggregation of MSCs into QDs. However, in either case, the earlier efforts to maintain a low-activity P precursor for preserving the InP monomer reservoir are undermined. Cossairt et al. developed a two-step nucleation and growth model for InP core synthesis via MSCs (Fig. 3(a)), demonstrating that the direct growth of QDs from MSCs occurs through a second nucleation event, where MSCs undergo destabilization and decomposition into monomers[65]. These InP cores then precipitate from the supersaturated monomer solution. Importantly, this process cannot be controlled merely by modulating the P precursor reactivity to maintain the monomer supply for continued growth. The two-step model highlights the critical role of MSCs' thermal stability in governing nucleation and growth of QDs. Further studies have revealed that ligand type and concentration significantly influence MSC stability and dissolution kinetics, thereby affecting the balance between nucleation and growth rates[90,95,96]. For instance, Hu et al. found that both insufficient and excessive amounts of TOP lead to poorly controlled size distributions in InP cores[27] (Fig. 3(b)). This is because InP MSC intermediates undergo a decomposition process. Therefore, only in the presence of an optimal amount of TOP can the decomposition, nucleation, and growth of InP MSCs reach a dynamic equilibrium. Under these conditions, InP cores with superior size uniformity can be obtained.

2.2 The strategy for improving the quality of the InP cores

2.2.1 Screening of core size by physical means

To achieve precise control over the QD size distribution, physical methods for stepwise size selection of QD cores offer an effective solution by exploiting the size-dependent solubility of QDs in different solvents. This approach involves the gradual introduction of an antisolvent, which selectively induces the precipitation of larger-sized cores, thereby enabling efficient size fractionation. Through multiple cycles of antisolvent addition and precipitation, InP cores with significantly enhanced size uniformity can be obtained. A notable demonstration by Heesun Yang's group showed that after four rounds of size sorting with incremental

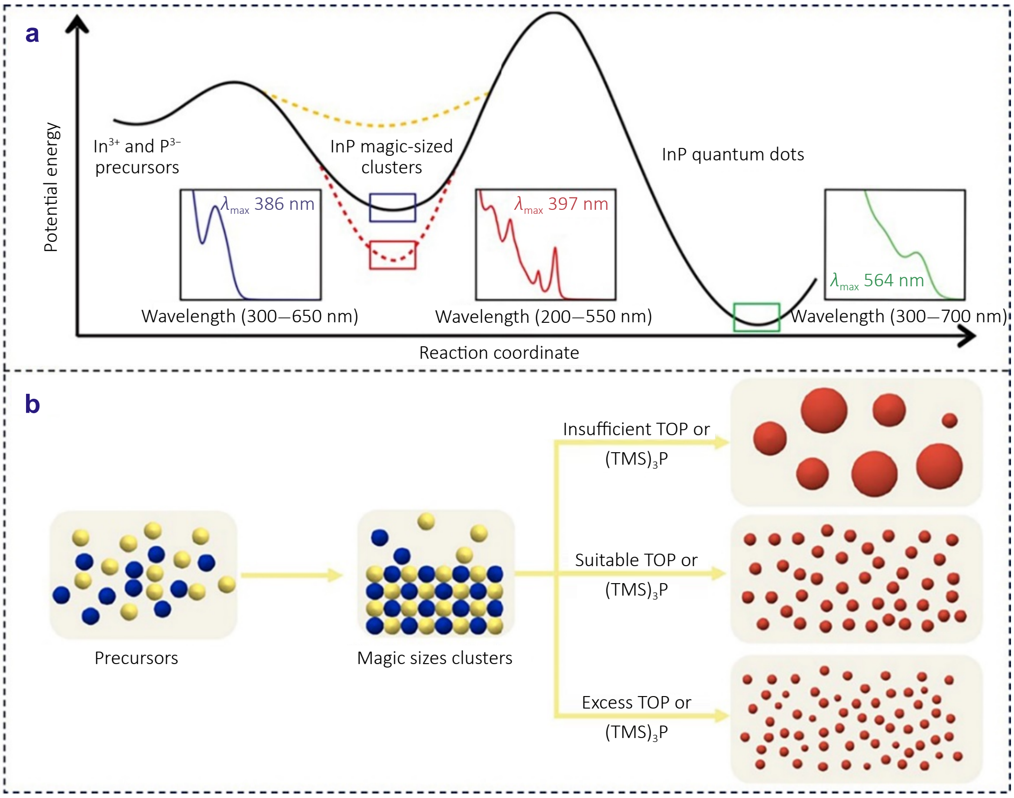

Fig. 3 | (a) Schematic illustration of the two-step nucleation mechanism for the growth of InP-based QDs from precursors, illustrating the MSC as a separable intermediate specie. (b) Schematic depicting the regulation of the conversion process from MSCs to InP cores and the uniformity of core size by varying the TOP addition amount. Figure reproduced with permission from: (a) ref.[65], (b) ref.[27], American Chemical Society.

ethanol addition to an InP core solution, about 70% of the original QDs remained. Subsequent shell coating of these size-selected cores yielded an emission spectrum with a remarkably narrow FWHM of 37 nm —a remarkable improvement over InP-based QDs synthesized using aminophosphines[97]. Importantly, this achieved FWHM approaches that of $P(SiMe_3)_3$-derived QDs, highlighting the exceptional effectiveness of the size-sorting method in enhancing the monodispersity of InP-based nanocrystals.

2.2.2 Modulation of InP cores by Zinc carboxylates

The size uniformity of the InP cores plays a dominant role in determining the color purity of QDs, while the crystallinity of the cores fundamentally governs their stability and efficiency. Poor crystallinity of the cores leads to lattice defects, making QDs susceptible to oxidation and photodegradation[98–100]. For instance, P vacancies on the InP surface create deep-level traps, which act as non-radiative recombination centers and significantly reduce the PL QY[99]. In contrast, QDs with high crystallinity exhibit longer exciton lifetimes and faster carrier migration rates, both of which are crucial for electroluminescent devices[100]. Numerous factors influence the crystallinity of InP cores, including the optimization of precursors and the selection of synthesis methods mentioned above. Recent studies demonstrate that incorporating Zn sources during InP nanocrystal synthesis yields significant improvements, as In(Zn)P QDs demonstrate superior size uniformity and emission color purity compared to bare InP counterparts[33,48,98,100,101]. For instance, Thuy et al. reported bare InP-based QDs with an FWHM of 90 nm, while In(Zn)P QDs achieved a narrower FWHM of 50 nm, along with an enhanced PL QY caused by improved crystallinity[98]. However, the beneficial effects of Zn primarily stem from two distinct, though potentially co-existing, mechanisms.

(1) Surface passivation and reaction kinetics modulation. Some studies suggest that Zn primarily passivates surface traps to enhance band-edge emission[82,98,101]. Stein et al., for example, observed PL enhancement upon post-synthetic treatment of pure InP-based QDs with zinc salts, supporting the surface passivation hypothesis[101]. Crucially, Zn plays a key role in moderating precursor reactivity and controlling growth kinetics[102,103]. Koh et al. investigated the role of the Zn source during the precursor conversion stage, revealing that Zn-P complexes form preferentially due to their higher thermodynamic stability compared to In-P complexes[103]. Density functional theory (DFT) and electrostatic potential charge analyses also confirmed the lower reactivity of Zn-P complexes compared to that of In-P complexes. As a result, the more stable Zn-P complex gradually releases P

monomers for controlled growth at high temperatures, which moderates the high reactivity of $P(SiMe_3)_3$, leading to improved monodispersity[103] (Fig. 4(a)).

(2) Alloying. The incorporation of Zn ions into the InP crystal lattice can lead to the formation of an In(Zn)P alloy[33,98,102,104,105]. Kirkwood et al.'s synchrotron X-ray absorption spectroscopy revealed that while most Zn exists as surface-bound zinc carboxylates, even trace amounts of Zn doping can induce lattice contraction[105] (Fig. 4(b)). The degree of alloying and its subsequent effects are strongly influenced by both the reactivity of Zn precursor and its concentration. For instance, highly active precursors (such as $Zn(Ac)_2$) achieve efficient doping of Zn into InP cores through low steric hindrance, reducing core/shell lattice mismatch[100,105]. Excessive Zn incorporation (Zn/In >1) leads to significant blue-shifted and broadened absorption spectra, along with X-ray diffraction (XRD) peak shifts, confirming alloy formation. Such uncontrolled alloying adversely impacts optical performance[104]. However, a notable example is the work by Yuan et al., who achieved controllable Zn doping and alloying by using the small-molecule precursor ($Zn(Ac)_2$). The study demonstrated that the low steric hindrance and moderate coordination strength of $Zn(Ac)_2$ facilitated the effective incorporation of Zn ions into the InP lattice, enabling better lattice matching with the ZnSeS/ZnS shell. This controlled alloying approach enhanced the PL QY of QDs to nearly 100% while maintaining a narrow emission spectrum[100].

2.2.3 Passivation on the surface of InP cores

Compared to bulk materials, QDs possess a significantly larger specific surface area, where surface atoms often exhibit incomplete coordination with ligands[106,107]. These uncoordinated atoms can generate trap states within the QD's band gap, leading to the capture of charge (electrons or holes), and possibly even quenching the PL of QDs[108–110]. The exposed P atoms are especially problematic due to their high oxidation susceptibility, forming an $InPO_x$ layer on the InP core surface[111–114]. This oxide layer not only deteriorates the optical properties of InP cores but also introduces electron traps and impedes the epitaxial growth of shell materials[115]. To date, water has been identified as the primary source of oxidation[113,116,117]. Intriguingly, even under rigorously controlled inert conditions, where oxygen and moisture are meticulously excluded, an oxide layer persists on the surface of InP-based QDs[117,118]. This observation strongly suggests that, in the absence of external oxidants, the oxidation likely originates from internally sourced water within the reaction system.

The most well-established method for synthesizing InP-based QDs involves the high-temperature reaction between excess indium carboxylate and $P(SiMe_3)_3$[25–28,39]. However,

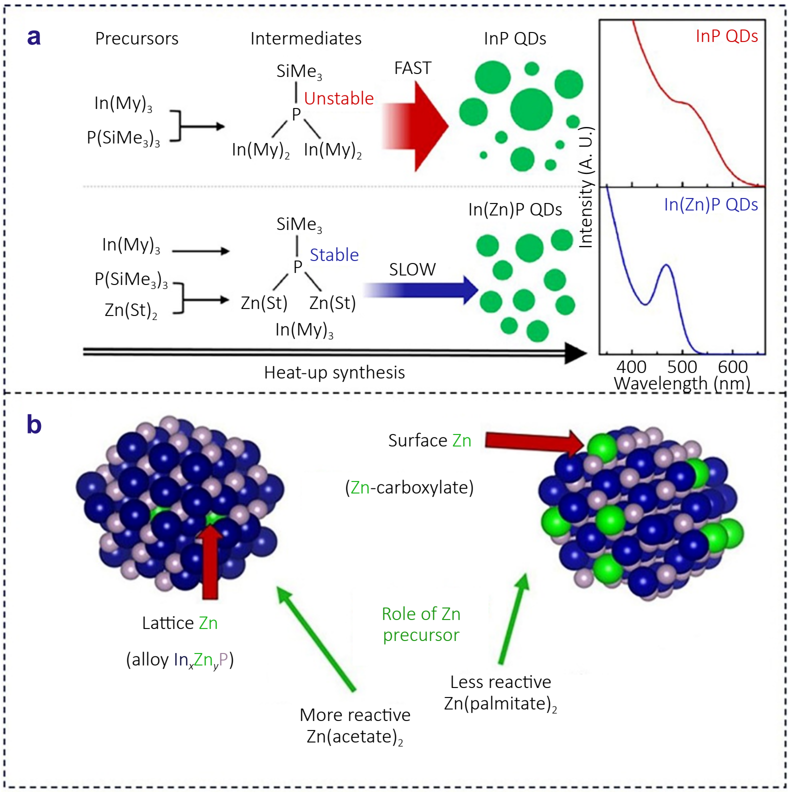

Fig. 4 | (a) Synthesis kinetics and UV-Vis absorption spectra of InP-based QDs in the absence and presence of Zn precursor. (b) The distribution of Zn within the InP core is dependent on the reactivity of the Zn precursor. Figure reproduced with permission from: (a) ref.[103], (b) ref.[105], American Chemical Society.

this approach presents a significant challenge as fatty acids tend to undergo ketonization reactions at elevated temperatures, generating dialkyl ketones and water as byproducts[33,112,113]. This in situ-generated water can partially oxidize the surface of InP core, resulting in the formation of an InP/$InPO_x$ heterostructure. To prevent surface oxidation of the InP core caused by free acids, researchers have explored alternative P sources, such as aminophosphines[117–119], which are more cost-effective, stable, and safer to handle. In principle, this synthetic approach should yield oxidation-free InP cores. However, despite the efforts of Cossairt et al., who successfully minimized in situ oxidation using aminophosphines and a rigorously degassed core/shell synthesis method, the phosphorus oxidation rate in InP/Zn(Se, S) QDs remained as high as 85%[114]. This suggests that even in the absence of free carboxylic acids, significant interfacial oxidation is still present at the core/shell interface. Further investigations by Vikram et al. revealed a plausible oxidation mechanism during shell growth[117]. Their studies identified that stearates (derived from shell precursor) and oleylamine (acting as both a solvent and ligand) undergo an amido-hydrolysis reaction, generating oleylstearamide and an intermediate -O-Zn-OH. During the high-temperature shelling process, this hydroxide intermediate (-O-Zn-OH) can further decompose, producing zinc oxide and water, both of which contribute to oxidation at the core/shell interface. To prevent such occurrences in aminophosphine-based synthesis systems, Long et al. employed a carboxylic acid-free method during the synthesis process, replacing zinc carboxylate with zinc chloride ($ZnCl_2$) as the zinc precursor[86]. This modification not only eliminated the detrimental effects of carboxylic acids but also established a low-oxygen, low-moisture environment for subsequent shell growth, ultimately improving the PL QY and stability of the InP-based QDs.

The oxidation of QD surfaces induced by free acids and primary amines is well-documented[112,113,117]. However, synthesizing InP-based QDs without carboxylic acids and primary amines presents a challenge, making the passivation of defect states generated by unsaturated surface atoms essential for improving the PL QY of InP cores. To address oxidized surface states and passivate unsaturated surface atoms, researchers have investigated various ligands to reduce surface trap states.

2.2.3.1 Fluoride (F^-) passivation

F^- has been extensively demonstrated to significantly enhance the PL QY of InP-based QDs. The pioneering work by Micic et al. in 1996 introduced the hydrogen fluoride (HF) etching as an effective method, which achieved a remarkable PL QY exceeding 40% for InP cores[120]. Subsequent studies have revealed that the mechanisms underlying PL QY improvement vary significantly depending on HF concentration. At lower HF concentrations, fluorination is thermodynamically favored[106]. Currently, researchers have proposed two passivation mechanisms targeting P and In dangling bonds respectively to explain their performance improvement. On the one hand, researchers have shown that F^- reacts with P dangling bonds, converting P^{3-} to PF_3, thereby eliminating anionic trap states[110,121,122]. This reaction leads to a surface reconstruction where InP cores are predominantly terminated with In atoms, which are further passivated by other ligands. After treatment, the resulting InP cores achieve a PL QY increased by approximately three orders of magnitude, reaching nearly 40% at room temperature. On the other hand, F^- acts as an X-type ligand to passivate unsaturated In surface sites[106,123]. As evidenced by Kim et al. in 2018, HF treatment facilitates an organic-inorganic ligand exchange process, wherein hydrophobic organic ligands are replaced by F^- ligands. This exchange results in a higher surface passivation density, significantly improving the passivation of In-dangling bonds. Consequently, the PL QY of InP cores exhibits a dramatic increase from 3% to 36%[106] (Fig. 5(a)). In addition, at higher HF concentrations, HF can play a crucial role in etching the surface oxide layer[25,122,124]. A seminal study by Pu et al. in 2021 systematically investigated the effect of the interfacial oxide layer on carrier recombination dynamics in InP-based QDs[124]. As shown in Fig. 5(b), the photogenerated carriers in InP cores undergo two distinct recombination pathways: a minor fraction recombines radiatively via the conduction band and valence band, and a dominant fraction is captured by the electron traps in the surface oxide layer. This trapping mechanism results in non-radiative recombination, dramatically suppressing the PL QY to below 1% for bare InP cores. However, by employing HF to remove the majority of the oxide layer while subsequent Zn^{2+} passivation effectively addresses P vacancies, the number of electronic defects at the QD interface is significantly reduced. Following shell encapsulation, the non-radiative recombination of photogenerated electron-hole pairs at the core/shell interface oxide layer is substantially suppressed, while the radiative recombination pathways become dominant, ultimately yielding InP-based QDs with a higher PL QY of 80% and a narrower FWHM of 52 nm. These findings were further validated by Won et al., who demonstrated that HF-mediated oxide removal enables the growth of highly uniform and symmetric ZnSe/ZnS shells, ultimately achieving QDs with near-unity PL QY[25].

However, the high toxicity and corrosiveness of HF, coupled with the rapid pressure increase during high-temperature injection, poses significant safety hazards. To mitigate these risks, researchers have actively pursued safer alternatives to conventional HF solutions[28,125–130]. For instance, Shen et al. have developed an innovative approach employing inorganic salt ZnF_2 in combination with carboxylic acid to generate HF in situ at high temperature[28]. This method not only improves operational safety but also produces QDs with narrower emission linewidths and superior thermal stability compared to those treated with

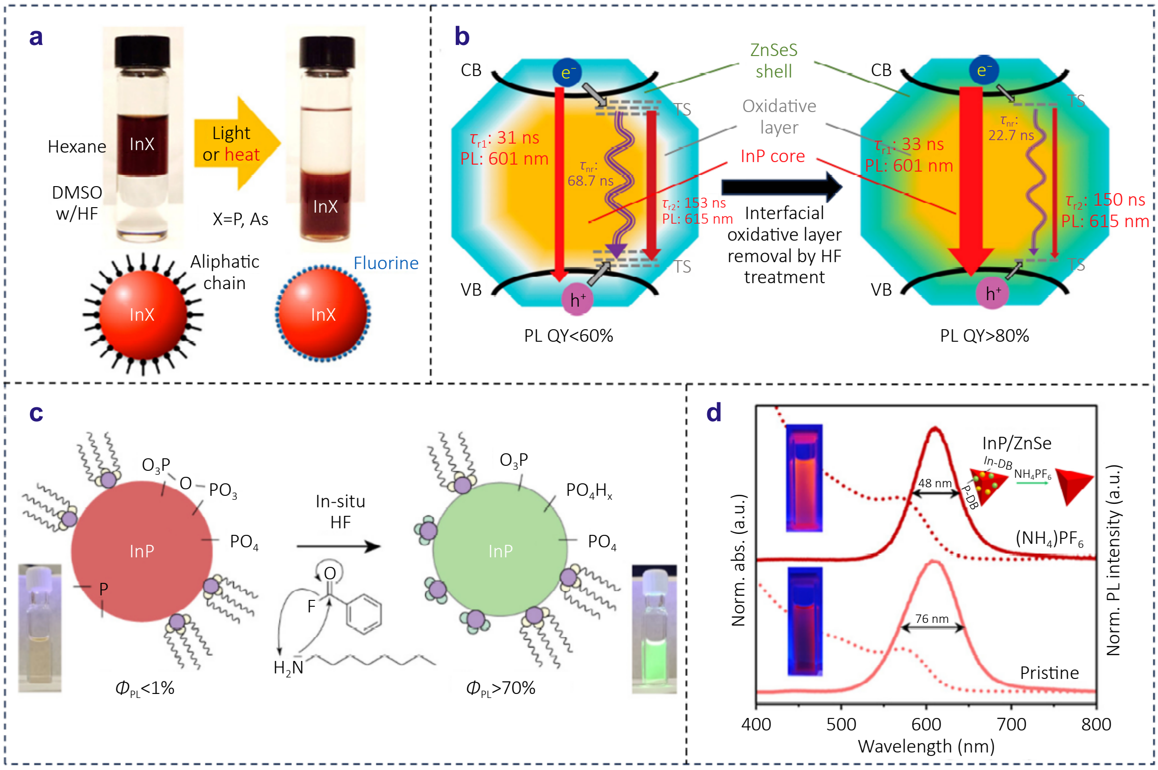

Fig. 5 | (a) Schematic illustration of HF treatment promoting the organic-inorganic ligand exchange process. (b) Schematic illustration of energy band structures and proposed assignment of lifetimes for charge carrier recombination processes before and after HF treatment. (c) Schematic diagrams of InP-based QDs before and after benzoyl fluoride treatment. (d) Absorption and PL spectra of InP/ZnSe QDs before and after $(NH_4)PF_6$ treatment. Figure reproduced with permission from: (a) ref.[106], (b) ref.[124], (c) ref.[125], (d) ref.[130], American Chemical Society.

conventional HF. In a related advancement, Ubbink et al. utilized benzoyl fluoride to generate HF in situ for removing polyphosphates from the InP surface, while coordinating the Z-type ligand $ZnCl_2$ with surface P atoms, achieving a remarkable PL QY enhancement up to 85%[125] (Fig. 5(c)). Other HF alternatives include fluorinated ionic liquids[126,127], ammonium hydrogen fluoride[128], metal fluorides[129], and hexafluorophosphate ions[130], all of which have been proven effective in improving the PL QY of InP cores. Among these, ammonium hexafluorophosphate (NH_4PF_6) employs a dual-ion synergistic mechanism, where the NH_4^+ and PF_6^- ions generated upon thermal decomposition cooperatively passivate the InP core. The NH_4^+ binds to P atoms, forming P-NH_4 bonds, eliminating In dangling bonds and passivating hole traps. Simultaneously, the PF_6^- etches the oxide layer and binds to In atoms, forming In-PF_6 bonds, removing P dangling bonds, and passivating electron traps. The surface-treated QDs provide a clean interface for subsequent ZnSe shell growth. Ultimately, this process achieves a PL QY enhancement to 70%, a FWHM narrowing to 48 nm, and significantly improved QD stability[130] (Fig. 5(d)).

2.2.3.2 Z-type ligands

An inevitable issue is that the use of HF to treat InP cores may cause over-etching and broaden the emission spectra of InP-based QDs, significantly reducing their practicality in luminescence applications relying on narrow emission[28,125,131]. In seeking alternative treatments that avoid HF while enhancing ligand surface coverage on InP cores, Z-type ligands appear to be promising candidates[132,133]. These ligands can bind to undercoordinated P atoms on InP cores, passivate hole-related defects, and thereby improve the QDs' optical performance. For instance, introducing zinc carboxylate prior to shell coating reportedly increases the PL QY of InP cores by up to 20%[82,134,135]. Similarly, the introduction of Cd^{2+} can increase the PL QY of InP cores to 54%[123]. Several mechanisms have been proposed to explain the observed improvement in PL QY, including surface passivation[101], Zn-induced etching[134], or doping effects[136]. A comprehensive mechanistic study conducted by Stein et al. provided critical insights into the underlying principles of PL QY enhancement[101]. Through systematic optical and structural characterizations, they demonstrated that the primary mechanism involves the passivation of P dangling bonds on the QD surface. Further insights into resolving surface complexity have been gained through the introduction of Ga^{3+} during post-treatment of InP cores. The enhancement of InP core luminescence is achieved through multiple mechanisms: gallium phosphide (GaP) shell formation[137] and passivation[79,138]. Notably, researchers have identified that Ga^{3+} treatment facilitates the elimination of surface phosphorus dangling bonds that act as hole traps. However, optimal enhancement of the overall PL QY and slight narrowing of the FWHM occur only under moderate Ga^{3+} concentrations, which do not interfere with inner shell growth. Conversely, excess Ga incorporation degrades both PL QY and FWHM[79].

Additionally, Chen et al. made a significant discovery that using metal oleates (Zn^{2+} or Cd^{2+}) with excess oleic acid can effectively remove surface oxides from InP cores and directly bind to surface In atoms. This approach simultaneously passivates surface P atoms through simple coordination by the metal ions. These dual-functional metal oleates, exhibiting both etching and passivation capabilities, dramatically enhanced the PL QY of InP cores from ~0.1% to 9% prior to shell growth[139] (Fig. 6(a)). The key advantage of this method lies in its ability to maintain oxide-free InP surfaces for extended periods, though this method is currently limited to aminophosphine-derived InP synthesis. However, *Z*-type ligand passivation has inherent limitations in improving optical performance and cannot achieve near-unity PL QY enhancement. Stam et al. proposed that severe surface oxidation of QDs may hinder complete ligand coverage. Furthermore, they innovatively developed indium fluoride (InF_3) as a *Z*-type ligand to thoroughly passivate P dangling bonds on InP cores, achieving a record PL QY of 93%[131] (Fig. 6(b)). This breakthrough, however, was only applicable to QDs with minimal surface oxidation. Researchers have hypothesized that surface-engineered InP-based QDs exhibiting high PL QY without shells could unlock significant application potential[106,123]. In a notable advancement, Gwak et al. addressed the undercoordination issues of In and P atoms by employing a combination of zinc carboxylate and gallium chloride. Their approach achieved remarkable PL QY exceeding 95% in core-only InP-based QDs, eliminating the need for traditional shell structures[138] (Fig. 6(c)). Furthermore, they successfully implemented electroluminescent devices using these core-only InP-based QDs. Although the brightness remained below 1000 cd·m^{-2}, this achievement represents a pivotal milestone in the field of QD technology.

2.3 Core/shell engineering for InP core/shell QDs

While surface ligand etching or passivation can effectively eliminate trap states on InP core surfaces and enhance PL QY to over 90%[131,138], the single surface modification strategy faces several key challenges, including poor environmental stability and oxide layer regeneration. To construct

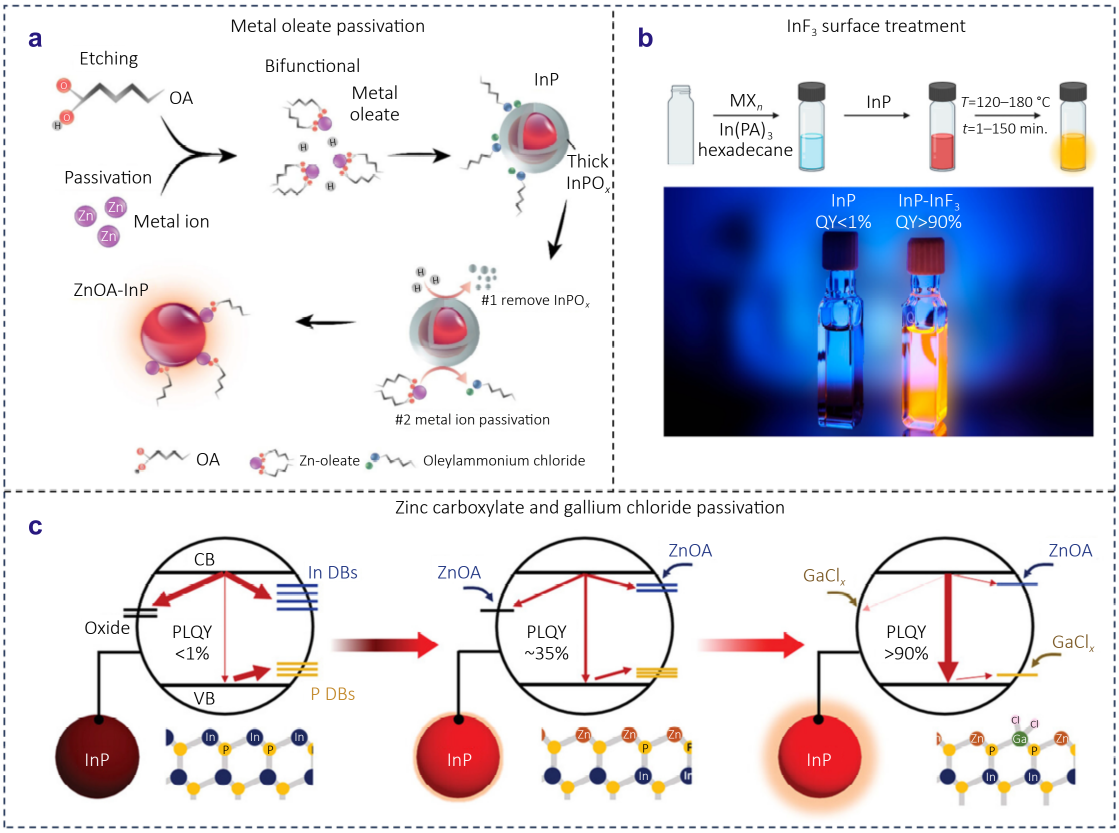

Fig. 6 | (a) Schematic illustration of dual-functional metal oleate passivating InP surfaces and etching surface oxides. (b) Schematic illustration of InF_3 surface treatment. (c) Schematic diagrams of bare and surface-passivated InP-based QDs. Figure reproduced with permission from: (a) ref.[139], MDPI; (b) ref.[131], American Chemical Society; (c) ref.[138], John Wiley and Sons.

QD systems with both high stability and efficiency, core/shell structural engineering demonstrates unique advantages. The outer shell achieves synergistic enhancement through multiple mechanisms. First, the dense shell forms a physical barrier that effectively blocks environmental degradation factors like oxygen and water molecules, thereby significantly improving the thermal- and photostability of QDs[28,140]. Second, while surface ligand passivation can mitigate some defects, uncoordinated dangling bonds (e.g., In^{3+} or P^{3-}) often persist on InP core surfaces. The epitaxial growth of shell materials like ZnSe or ZnS enables comprehensive passivation of residual defects, substantially reducing surface trap states[25,26,28]. Third, thick-shell designs confine carrier wavefunction distribution, suppressing their diffusion toward surfaces and thereby reducing Auger recombination probabilities[141−144]—a critical limitation in high-brightness QLED applications. Simultaneously, the band alignment of shell materials modulates the overall energy level structure of QDs, effectively buffering interfacial potential barriers between InP cores and charge transport layers (CTL)[41,145]. This integrated mechanism, combining physical protection, defect passivation, and energy-level engineering, not only compensates for the inherent limitations of surface ligands alone but also unlocks the potential of QDs for advanced applications. Through systematic optimization, core/shell engineering paves the way for QD-based technologies with enhanced performance and reliability.

In recent years, extensive studies have been conducted on the parameters of shell growth (composition[25,41,145], thickness[26,140], temperature[25,76], etc.) for InP-based QDs, leading to significant improvements in their optoelectronic performance. The essence of this optimization lies in the precise manipulation of shell parameters, which directly affects the spatial distribution of electrons and holes wavefunctions within the QDs, thereby significantly enhancing their photophysical properties. For InP-based QDs, the relatively large effective mass of holes in InP (m_h=0.64) makes the valence band level insensitive to changes in core size, so the hole wavefunction remains predominantly localized within the InP core[146]. In contrast, the much smaller effective electron mass (m_e=0.08) results in a rapid increase of conduction band edge energy with decreasing core size, facilitating electron wavefunction delocalization into the shell layer, particularly the ZnSe shell[146,147] (Fig. 7(a)). When the size of the InP core further decreases, this electron delocalization effect becomes more pronounced. Under such conditions, even small differences in the composition or thickness of the shell can significantly change the overlap of the electron-hole wavefunction, thereby determining the probability of radiative recombination[148]. As is well known, the PL QY is defined as the ratio of the radiative recombination rate (k_{rad}) to the sum of radiative and non-radiative recombination rates (k_{non}). According to Fermi's golden rule, k_{rad} is directly proportional to the transition dipole moment, $\mu = \langle \varphi_h | \hat{\mu} | \varphi_e \rangle$, where φ_e and φ_h represent electron and hole wavefunctions, respectively, and $\hat{\mu}$ denotes the electric dipole operator. Meanwhile, k_{non} is mainly related to surface trap states[147,148]. Therefore, synergistic optimization of shell parameters to simultaneously enhance the overlap of electron-hole wavefunctions and suppress defect-induced non-radiative recombination has become a key strategy for achieving high luminescence efficiency of InP-based QDs.

2.3.1 Shell structure

2.3.1.1 Single ZnS or ZnSe shell

In the pioneering development of InP-based core/shell QDs, ZnS emerged as the most widely adopted shell material due to its wide band-gap properties, which effectively confined charge carriers within the narrower band-gap InP core[84,94,135,149,150]. This InP/ZnS structure was extensively explored in foundational studies. For example, Brown et al. achieved precise tuning of emission wavelengths (515–577 nm) in In(Zn)P/ZnS QDs by regulating the Zn/In ratio in the InP core[94]. However, their research also revealed that the thermal and chemical stability of these QDs remained substantially inferior to that of CdSe-based counterparts, primarily due to suboptimal ZnS shell quality, rendering

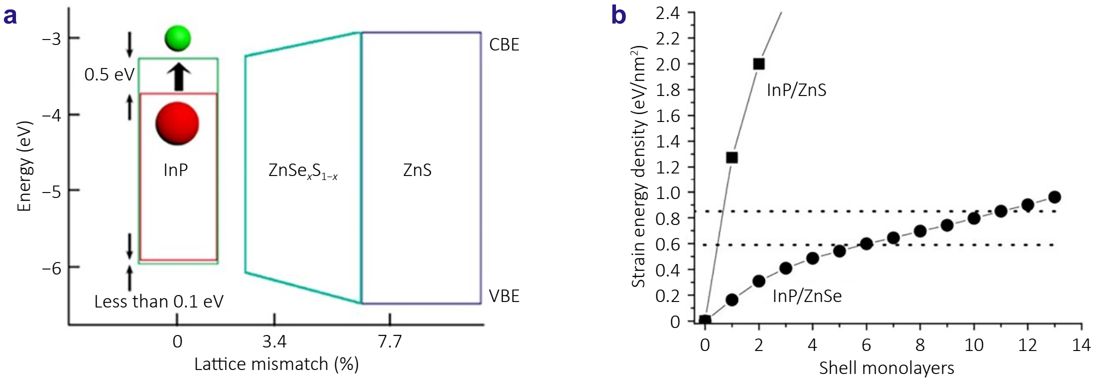

Fig. 7 | (a) Band energy levels and lattice mismatch between shell materials and InP cores. (b) Lattice strain energy density versus shell thickness for InP/ZnS and InP/ZnSe QDs. Figure reproduced with permission from: (a) ref.[147], (b) ref.[152], American Chemical Society.

them susceptible to degradation under operational conditions. Leveraging the strong confinement effect of ZnS, Cui et al. made significant advancements in blue-light efficiency and color purity of InP/ZnS QDs by controlling halogen ions and shell growth temperature, utilizing anion-exchange-mediated interface formation to create an In-S/S$_x$-In-P$_{1-x}$ graded layer. These resulting QDs exhibited an emission wavelength at 473 nm, a PL QY of 50%, and a narrow FWHM of approximately 47 nm[150]. However, the significant lattice mismatch (7.7%) between InP and ZnS creates considerable interface strain[151], which negatively impacts the optical properties of InP/ZnS QDs, resulting in a PL QY of approximately 20%–80% and a FWHM of 45–80 nm across different studies[84,94,135,149,150].

Compared to ZnS, ZnSe has a smaller lattice mismatch with InP, making it more likely to mitigate lattice strain[151]. The extent of lattice mismatch plays a crucial role in determining both the coherence of the core/shell interface and the shell thickness[152,153]. Research by Lange et al. showed that InP/ZnSe QDs, benefiting from their minimal lattice mismatch, can maintain coherent interfaces and achieve uniform growth even with thick shell layers. In contrast, InP/ZnS QDs, with a larger mismatch, fail to form coherent interfaces due to excessive strain energy, resulting in non-uniform shell growth[152] (Fig. 7(b)). Therefore, InP/ZnSe QDs exhibit narrower FWHM compared to their InP/ZnS counterparts[94,154]. Although the ZnSe shell significantly reduces lattice mismatch, Se is inherently prone to photooxidation, making the final heterostructure prone to degradation over time[155–158]. Moreover, InP/ZnSe QDs possess a deep valence band offset (>0.7 eV) coupled with a shallow conduction band offset, leading to quasi-Type II behavior characterized by electron delocalization and hole localization[159]. Notably, reducing the core size substantially diminishes the valence band offset, causing the hole wavefunction to extend into the shell layer, which adversely affects stability. Therefore, to address these stability concerns, passivation with a ZnS outer shell on the surface of InP/ZnSe would provide effective environmental protection.

2.3.1.2 Double ZnSe/ZnS shell or GaP/ZnS shell

To fully exploit the lattice-matching benefits of ZnSe while maintaining the superior stability of ZnS, a double ZnSe/ZnS shell is essential for both interfacial strain mitigation and overall stability enhancement[25,26,28,160,161]. Kim et al. conducted a comprehensive investigation of the steady-state PL spectra for InP/ZnS, InP/ZnSe, and InP/ZnSe/ZnS core/shell QDs across a wide temperature range (77–297 K)[160] (Fig. 8(a)). Their study particularly emphasized the role of thermal population dynamics in emission states, which serves as a crucial parameter for elucidating charge transfer mechanisms between neutral and charged trap states. The study revealed that InP cores showed strong trap-state emissions within the range of 600–750 nm, indicating severe surface defects in unpassivated InP cores. As the temperature decreased, both InP/ZnS and InP/ZnSe QDs began to show low-energy trap emissions. Remarkably, however, the InP/ZnSe/ZnS QDs exhibited no trap-state emissions even at the very low temperature of 77 K, underscoring the exceptional passivation capability of the multilayer ZnSe/ZnS shell. This effective defect suppression contributed to an outstanding PL QY of up to 95%. These findings offer critical guidance for the strategic design of shell architectures to optimize the optical properties of InP-based QDs, paving the way for high-performance QD applications.

In contrast to ZnSe, GaP demonstrates superior chemical stability (due to the stronger Ga-P bond) and more pronounced quantum confinement effects (owing to its smaller exciton Bohr radius)[162–164]. These advantageous properties have attracted significant research interest, leading to the incorporation of GaP into InP-based QDs, forming either GaP inner shells[164–167] or InGaP alloyed cores[163,168–171]. The existence form of Ga element inside InP-based QDs is highly related to the preparation method, with a key differentiating factor being the different reaction activity between In and Ga precursors[162,164,167,172]. In 2015, Park's research demonstrated a marked reactivity contrast between In and Ga precursors, with InP forming below 100 °C while GaP nucleation required temperature exceeding 200 °C[167,173]. This significant disparity enables the sequential formation of InP cores followed by GaP shell deposition during a controlled heating process, even when all precursors are initially present. Leveraging this approach, the researchers successfully synthesized InP/GaP/ZnS core/shell QDs exhibiting tunable emission across the entire visible spectrum from blue to red[167]. Further investigations have revealed that the selection of metal precursors plays a pivotal role in governing reaction kinetics and ultimately dictating QD morphology[162,172]. For example, the Reiss group demonstrated that gallium oleate (Ga(OA)$_3$) yields distinct InP/GaP core/shell structure, whereas gallium acetylacetonate (Ga(acac)$_3$) facilitates the formation of InGaP alloyed QDs. This difference stems from the substantially enhanced reactivity of Ga(acac)$_3$, which promotes Ga incorporation into the InP lattice[172]. In 2024, Yoo et al. conducted a more systematic study on the influence of the relative reactivity of metal carboxylate complexes on synthesis results[162] (Fig. 8(b)). Their findings revealed that when In and Ga precursors share identical alkyl carboxylate ligands, the inherent higher reactivity of In (consistent with Kim's earlier observations) dominates, resulting in InP/GaP core/shell structure. However, when Ga carboxylate complexes are prepared with shorter-chain alkyl carboxylate ligands, the reduced steric hindrance dramatically boosts Ga precursor reactivity. This adjustment balances the formation kinetics of In-P and Ga-P bonds, ultimately leading to the production of homogeneous InGaP alloyed QDs.

In addition to enhancing the reactivity of Ga precursors, cation exchange plays a pivotal role in enabling precise compositional tuning of pre-synthesized InGaP-based QDs[163,168,169,171]. However, the inherent challenge lies in the

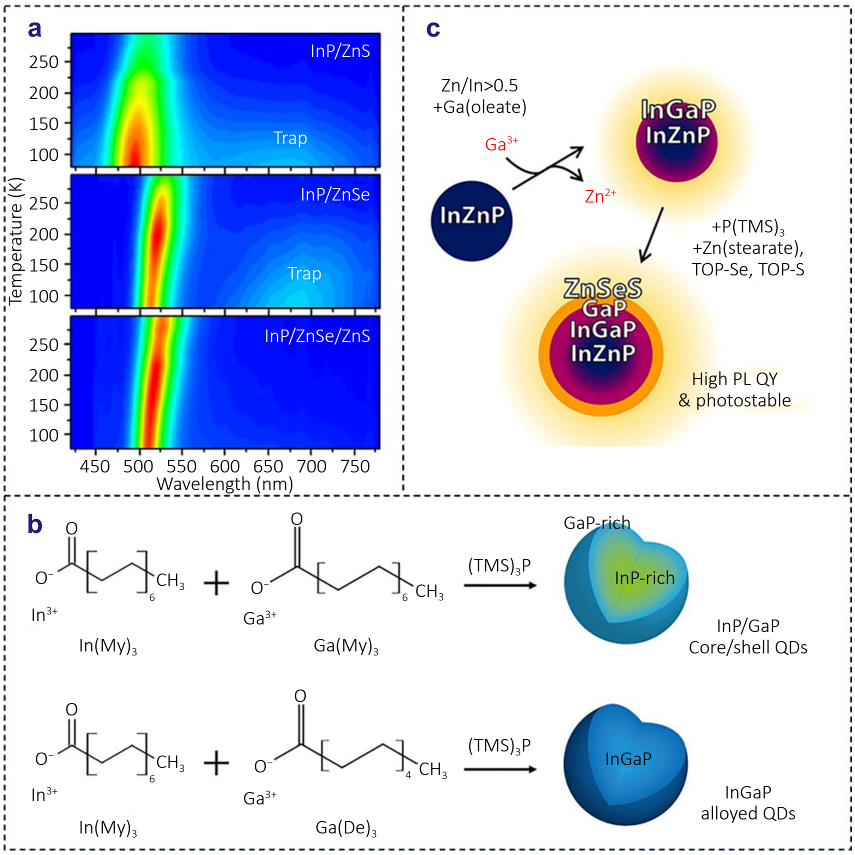

Fig. 8 | (a) Two-dimensional PL spectra of InP/ZnS, InP/ZnSe, and InP/ZnSe/ZnS QDs from 77 K to 297 K. (b) Synthetic schematic of InP-based QDs using metal carboxylate precursors with varied alkyl chain lengths. (c) Synthetic scheme for InZnP/InGaP/ZnSeS QDs. Figure reproduced with permission from: (a) ref.[160], (b) ref.[162], (c) ref.[169], American Chemical Society.

highly covalent nature of III-V QDs, which typically exhibit strong resistance to cation exchange[163]. Conventional approaches to achieve substantial Ga alloying in InP cores necessitate extreme conditions, requiring cation exchange in molten salts at elevated temperatures ranging from 380 °C to 450 °C[163,168]. Although this high-temperature process successfully reduces lattice constants and increases band gaps, thereby inducing the desired spectral blue shift, its harsh operational conditions significantly restrict broader practical applications. Consequently, the development of cation exchange technology that can be achieved in low temperature has significant practical implications[169,171]. A notable example is the work by Pietra et al., who discovered that in InZnP-based QD systems with a Zn/In molar ratio exceeding 0.5, Ga^{3+} preferentially exchanges with Zn^{2+}, forming an InZnP/InGaP core/shell structure[169] (Fig. 8(c)). Even in the absence of excess Ga, this exchange induces a significant spectral blue shift and enhances the PL QY from approximately 10% to 50%. Subsequent coating with a GaP/ZnSeS shell further increases the PL QY to 75%. In comparison, the highest reported PL QY for InP/GaP/ZnS core/shell QDs currently reaches 85%[166]. Meanwhile, the development of InGaP alloy cores as blue emitters represents a particularly promising direction. Unlike binary InP, ternary InGaP enables the synthesis of larger-sized QDs capable of blue emission, thereby providing a viable strategy for reliably producing bright blue-emitting InGaP QDs. A striking example is the work by Yang et al., who reported InGaP/ZnSeS/ZnS QDs exhibiting blue emission at 465 nm with an exceptional PL QY of 80%–82%, and the corresponding QLEDs exhibiting a high EQE of 2.5%, representing one of the best blue-emitting InP-based devices to date[171].

2.3.1.3 Alloyed shell

To integrate the advantages of ZnSe (alleviating lattice strain) and ZnS (preventing oxidation and degradation) and obtain QDs with high PL QY, researchers introduced an alloyed ZnSeS interfacial buffer layer. By leveraging the higher reactivity of TOP-Se compared to TOP-S[174,175], a thick and uniform ZnSeS shell with a radial composition gradient was successfully grown on the InP core[38] (Fig. 9(a)). The resulting InP/ZnSeS QDs exhibited superior photochemical stability compared to both InP/ZnS and InP/ZnSe QDs. This enhanced stability is attributed to the improved uniformity of the composition-gradient shell, effective confinement of exciton wavefunctions, and minimized surface oxidation and non-radiative recombination. To further prevent surface defects and electron trapping, a thin ZnS passivation layer was applied as the outermost shell, forming a core/shell/shell structure of InP/ZnSe$_x$S$_{1-x}$/ZnS[41,76,78,86,147]. The Se/S ratio in the ZnSeS alloy plays a critical role in determining both the QDs' morphology and PL QY[147] (Fig. 9(b)). Experimental optimization revealed that an S-rich ZnSe$_x$S$_{1-x}$ inner shell, with its wider bandgap, effectively confines carriers within the InP core, thereby increasing PL QY. However, the significant lattice mismatch between ZnS and InP often

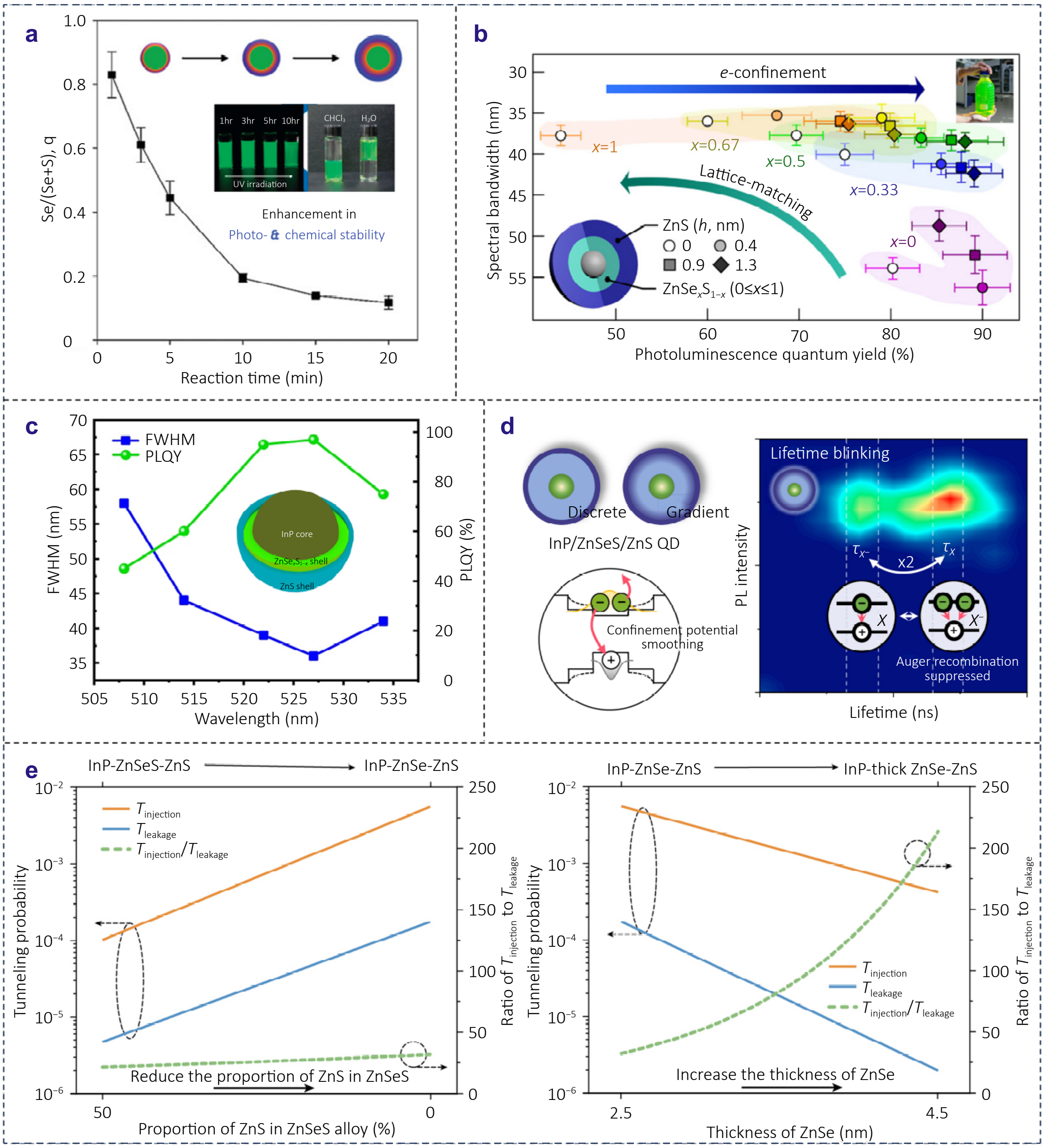

Fig. 9 | (a) Radial Se gradient evolution in ZnSeS shell during growth, with inset showing photochemical stability of InP/ZnSeS QDs. (b) PL QY and FWHM for InP/ZnSeS/ZnS QDs with varied Se/S ratios in intermediate ZnSeS shells and different outer ZnS shell thicknesses. (c) Evolution of FWHM and PL QY with Se/S composition in graded ZnSeS interlayers. (d) Non-radiative Auger recombination schematic (left) and fluorescence lifetime intensity distribution (FLID) plots (right) for InP/ZnSe/ZnS and InP/ZnSeS/ZnS QDs. (e) Simulations of the tunnelling probabilities of injection and leakage and their ratios. The left plot represents the case when the ZnS proportion is reduced. The right plot illustrates the effect of thickening the ZnSe shell. Among them, the electron injection current density J_I is approximately proportional to the electron injection tunnelling probability $T_{injection}$. The electron leakage current density J_L is proportional to the electron leakage tunnelling probability $T_{leakage}$. The ratio of $T_{injection}$ to $T_{leakage}$ determines the EQE. Figure reproduced with permission from: (a) ref.[38], American Chemical Society; (b) ref.[147], American Chemical Society; (c) ref.[41], Springer Nature; (d) ref.[144], American Chemical Society; (e) ref.[26], Springer Nature.

leads to irregular morphology. Conversely, a Se-rich alloy shell facilitates more uniform growth of thicker shells, ensuring better photochemical stability. Consequently, high-quality gradient shells require a ZnSe content exceeding 50% in the intermediate layer[41,147]. For example, Zhao et al. achieved optimal performance with a 7:3 Se/S ratio in the ZnSeS inner shell, obtaining InP-based QDs with the narrowest FWHM of ~35 nm and a record-high PL QY of ~97%[41] (Fig. 9(c)). Compared to discrete-shell InP/ZnSe/ZnS QDs, where an additional interfacial trap site exists due to incomplete lattice strain relief between the ZnSe middle shell and ZnS outer shell, gradient-shell QDs have been proven to significantly suppress Auger recombination. This was experimentally verified by Lee et al. through the observation of the "lifetime blinking" phenomenon[144] (Fig. 9(d)). Although single-particle QDs with the InP/$ZnSe_{0.75}S_{0.25}$/ZnS structure exhibit narrower spectral linewidths, the ensemble FWHM remains comparable to that of discrete-shell InP/ZnSe/ZnS QDs, which may be attributed to slightly higher compositional inhomogeneity in gradient-shell QDs[176]. Although gradient-shell QDs show marginally better optical performance, discrete-shell InP/ZnSe/ZnS QDs with slightly reduced ZnS content may offer more advantages for device applications. According to our quantum tunneling model[26], although the ZnSeS interlayer with a higher ZnS component provides a certain electron blocking capability, its excessively high injection barrier leads to insufficient electron injection, becoming a performance bottleneck. In contrast, using a pure ZnSe interlayer effectively reduces the injection barrier and improves electron injection. Furthermore, by increasing the thickness of the ZnSe layer, the tunneling probability of electron leakage can be significantly reduced. This approach effectively suppresses leakage while maintaining efficient injection, ultimately achieving a notable improvement in EQE (Fig. 9(e)).

2.3.2 Shell thickness

Comparative analysis of different shell structures in InP-based QDs reveals that the selection of shell materials significantly influences both band alignment and surface passivation effects[25,26,147]. While optimal shell material can be identified for specific applications, the ultimate optical performance and stability of these QDs are critically dependent on precise control over shell thickness. To enhance the performance of InP-based QDs, the growth of ultra-thick shells on the InP core surface is essential to address the issues of poor stability and rapid PL QY degradation[140,177], while simultaneously suppressing non-radiative Förster resonance energy transfer (FRET) processes between small-sized QDs[161].

Thick ZnS shells play a crucial role in effectively isolating oxygen, moisture, and chemicals, thereby significantly reducing the risk of oxidation or photodegradation of the InP core, and exhibiting exceptional performance stability in harsh environments (e.g., high temperatures or acidic conditions). For blue-emitting applications, the wide bandgap (3.68 eV) of ZnS is particularly advantageous as it provides strong exciton confinement within the InP core[151,178]. For instance, Zhang et al. successfully synthesized InP/ZnS/ZnS QDs with a dual-shell structure, achieving stable pure blue emission at the shortest wavelength of 468 nm with an FWHM of 47 nm[178]. Furthermore, thick ZnS shells serve as an effective strategy to mitigate stability degradation resulting from surface ligand detachment during QD purification[177]. Partial removal of surface ligands during purification generates electron trap states, which promote carrier wavefunction leakage and subsequent non-radiative recombination, ultimately diminishing PL QY[179]. The introduction of thicker ZnS shells establishes a higher energy barrier, effectively confining carriers within the InP core and preventing their migration to surface defect states, thereby enhancing luminescence efficiency[177] (Fig. 10(a)).

However, the significant lattice mismatch between InP and ZnS (~7.7%) presents a critical challenge[151]. Excessive shell thickness may exacerbate interfacial strain, potentially leading to the formation of dislocations or cracks that introduce new non-radiative recombination pathways[152]. This trade-off becomes particularly consequential in applications requiring carrier injection or energy transfer (e.g., QLEDs, FRET sensors), where overly thick shells may form energy barriers that compromise device efficiency. The presence of a GaP interfacial layer effectively minimizes lattice mismatch and reduces interfacial defects, but it also requires a thick ZnS outer shell to enhance electron confinement. The thick ZnS shell suppresses FRET between densely packed QDs, ensuring high PL QY and stability[164,165]. Shen et al. effectively capitalized on these properties by developing green-emitting QLEDs based on such structures, which demonstrated performance with peak EQE and current efficiency reaching 6.3% and 13.7 cd·A^{-1}, respectively[165]. Despite these advances, further optimization of this structure is still needed to achieve even higher device performance.

To reduce the lattice mismatch between InP and ZnS, a thick and uniform ZnSe shell layer is crucial for suppressing Auger recombination and energy transfer between QDs films[141–144]. Research has found that the difference in the ZnSe intermediate shell thickness significantly influences the band structure and electronic behavior of QDs[25,26,154]. Both excessive and insufficient shell layers can widen FWHM and reduce PL QY[180]. For red-emitting QDs, the significant conduction band offset between the ZnSe intermediate shell and InP core results in both the ZnSe intermediate layer and ZnS outer shell functioning as electron confinement layers. Here, thicker ZnSe shells demonstrate superior performance in both PL QY and electroluminescence (EL) efficiency[25,140,154]. In contrast, for green-emitting QDs, the proximity of conduction band minima between the InP core and ZnSe intermediate shell leads to increased electron delocalization as the intermediate shell thickens, accompanied by a red shift in PL[148,180]. When the ZnSe intermediate shell is too thin, the degradation of FWHM and PL QY arises from

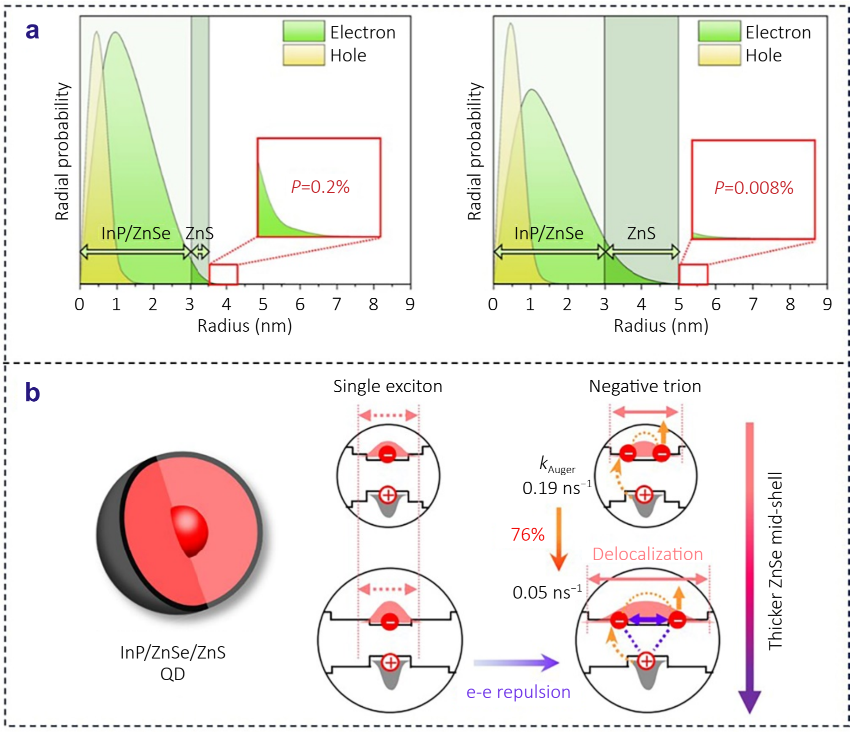

Fig. 10 | (a) Carrier wave function probability distributions in InP/ZnSe/thin ZnS (left) and InP/ZnSe/thick ZnS (right) structures, with insets depicting electron wave function leakage from surface. (b) Schematic of hot carrier dynamics in InP/ZnSe/ZnS QDs with thin (up) and thick (down) ZnSe interlayers. Figure reproduced with permission from: (a) ref.[177], (b) ref.[141], American Chemical Society.

insufficient lattice strain relief between InP and ZnS due to inadequate ZnSe thickness or coverage. Conversely, an excessively thick ZnSe shell deteriorates FWHM and PL QY by increasing the probability of delocalized electrons encountering defects at the core/shell interface[181]. Kim et al. provided a more detailed explanation of the advantages of thickening the ZnSe intermediate shell[141]. The expanded space afforded by the thick ZnSe intermediate shell promotes delocalization of excess electrons —particularly those in negative trions—into the shell region. This delocalization is governed by electron-electron Coulomb repulsion, facilitating electron diffusion into the ZnSe layer. Simultaneously, the thick ZnSe midshell weakens electron-hole Coulomb interactions, substantially reducing the Auger recombination rate of negative trions —by 76% in photochemical doping measurements and 67% in single QD measurements (Fig. 10(b)). Consequently, this mechanism effectively suppresses non-radiative energy losses during QLED operation, significantly enhancing EQE, luminance, and operational lifetime.

2.3.3 Kinetic regulation of shell growth

The generation of interfacial lattice strain during the growth of thick shells is indeed a critical challenge. This strain originates from the inherent lattice mismatch between core and shell materials, potentially inducing interfacial defects, structural distortions, and even catastrophic material fracture—all of which can affect the physicochemical properties of the emitting material[182−184]. Consequently, precise control over shell growth kinetics emerges as a critical strategy for strain mitigation and the realization of defect-free thick-shell architectures[76,140,185−187]. In a notable advancement, Chen et al. recently demonstrated a breakthrough in synthesizing ultra-large red-emitting InP-based QDs with shield-like morphology (PL QY ≈ 90%). Through a carefully controlled slow-injection protocol for shell precursors, the researchers maintained thermodynamic equilibrium throughout the shell growth process. This innovative approach enabled the fabrication of defect-free thick-shell InP/ZnSe/ZnSeS/ZnS QDs (>20 nm) that exhibit exceptional photo- and thermal-stability, representing a significant milestone in QD technology[140] (Fig. 11(a)).

In zinc-blende structure crystals, the inherent thermodynamic disparities among different crystal facets make temperature a crucial determinant of shell morphology[188]. By modulating atomic surface diffusion rates, regulating facet-dependent growth kinetics, and controlling precursor decomposition and reaction dynamics, temperature drives the system toward thermodynamic equilibrium[25,140,182,189]. Extensive experimental investigations have unequivocally demonstrated temperature's pivotal role in morphological control[25,76,143,160,186]. For instance, Won et al. revealed that low-temperature ZnSe/ZnS shell growth resulted in pod-like morphologies and incomplete passivation due to lattice

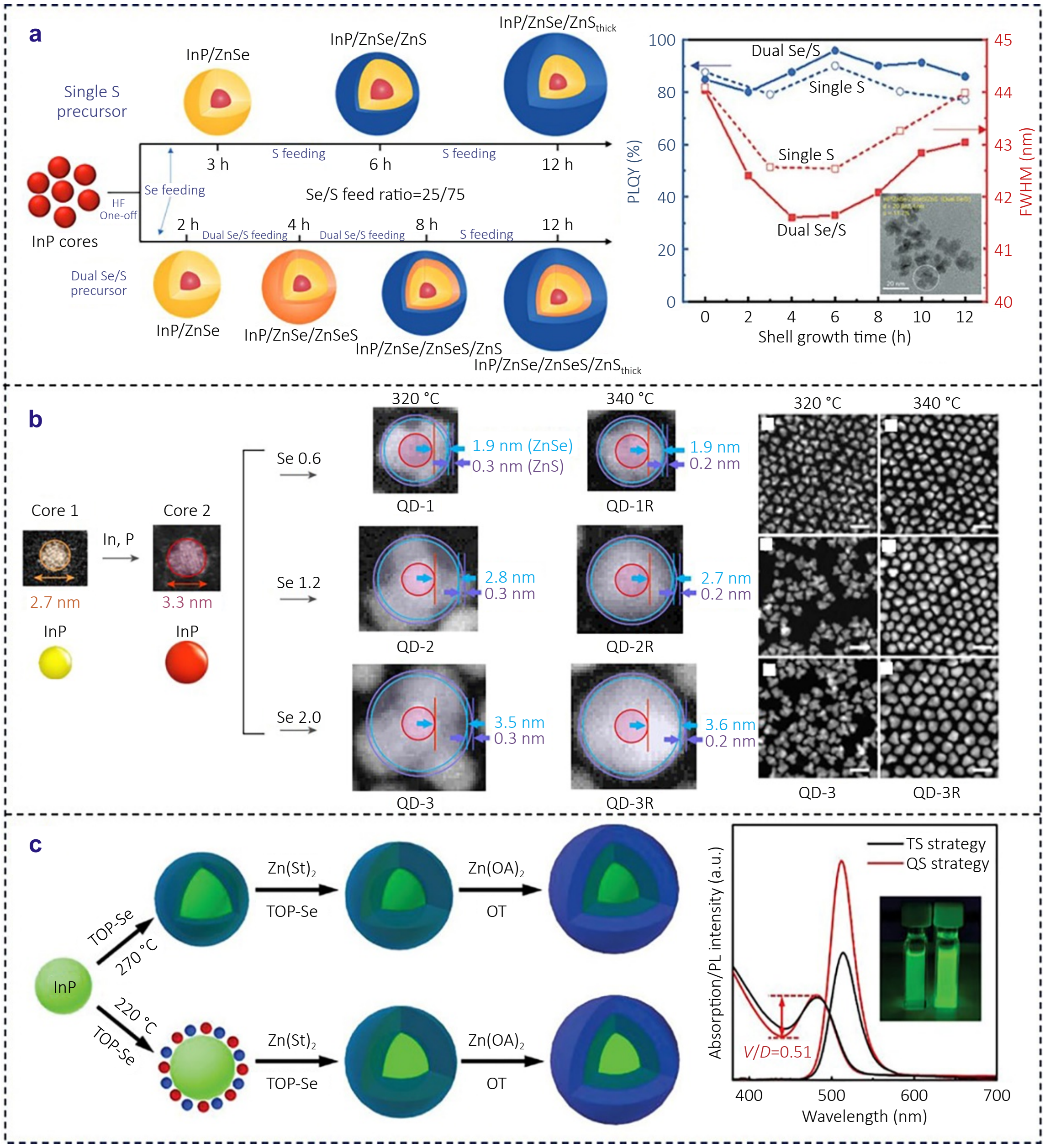

Fig. 11 | (a) Ultra-large-sized InP-based QDs with morphological shell grown via two different growth strategies, i.e., single S and dual Se/S precursor. (b) Synthesis schematics (left) and scanning transmission electron microscopy (STEM) images (scale bar: 20 nm, right) of InP/ZnSe/ZnS QDs as functions of temperature and shell thickness. (c) Schematic diagrams of InP/ZnSe/ZnS QDs synthesis using the traditional synthetic strategy (top) and the quasi-shell-growth strategy (bottom) (left), and absorption and PL spectra (right). Insets show luminescence photographs of the QDs prepared by the two strategies. Figure reproduced with permission from: (a) ref.[140], John Wiley and Sons; (b) ref.[25], Springer Nature; (c) ref.[186], John Wiley and Sons.

mismatch, limiting the optical performance of QDs. Remarkably, elevating the temperature to 340 °C dramatically enhanced surface diffusion and reaction kinetics, promoting equilibrium growth conditions that produced spherically uniform QDs with perfect passivation and 100% PL QY[25] (Fig. 11(b)). Similarly, Kim et al. also successfully employed a high-temperature shell coating strategy that achieved unprecedented passivation of green-emitting InP cores, producing InP/ZnSe/ZnS QDs with record-breaking performance (95% PL QY, 36 nm FWHM)[160]. The researchers further optimized the synthesis by injecting the P precursor at a moderate temperature to narrow the core size distribution to 12%, and precisely controlling Se/S precursor injection parameters at elevated temperatures to accelerate shell growth while suppressing parasitic nucleation, thereby enhancing crystallinity and uniformity. Furthermore, research by Park et al. also demonstrated that rapidly growing the ZnSe shell at elevated reaction temperatures promotes isotropic QD formation, eliminating stacking faults and minimizing hole trap states, which substantially improved the PL QY of InP/ZnSe/ZnS QDs[143].

Recent studies have demonstrated that while elevated temperatures facilitate the epitaxial growth of high-quality semiconductor shells, a delicate equilibrium must be maintained to minimize thermal degradation of the core[76,147,187]. A breakthrough was achieved by Yang's team through their innovative cyclic gradient heating protocol, which enabled the layer-by-layer growth of 15 nm InP/ZnSe/ZnS core/shell QDs[187]. This approach utilized periodic temperature modulation coupled with a low-reactivity sulfur precursor (1-dodecanethiol (1-DDT)) and gradient heating to enhance molecular thermal activation while suppressing anisotropic growth through controlled precursor supply. The kinetic optimization successfully prevented Ostwald ripening of InP cores while facilitating thick shell growth, yielding exceptionally stable QDs with a PL QY of 73%, a narrow FWHM of 40 nm, and tunable emission ranging from 549 nm to 617 nm.

This finding was further validated by subsequent research. Zhao et al. demonstrated that thermal treatment exceeding 240 °C induces structural degradation in InP cores[76]. Building upon this insight, they developed a temperature gradient solution growth (TGSG) methodology. By progressively increasing the reaction temperature from 240 °C to 280 °C during the growth of InP/ZnSeS/ZnS multishell structures, the gradual thermal profile effectively prevented core overheating and ripening while ensuring shell densification, ultimately achieving remarkable optical properties with a high PL QY of 91% and an ultra-narrow FWHM of 36 nm. Similarly, to suppress the non-uniform particle size distribution and broadened emission spectra caused by Ostwald ripening at high temperature in InP-based QDs, Yang et al. developed an innovative quasi-shell growth strategy[186]. This approach involved the growth of a quasi-ZnSe shell at low temperature to passivate surface defects on the InP cores, thereby fundamentally inhibiting high-temperature ripening and promoting isotropic QD growth. The resulting InP/ZnSe/ZnS QDs exhibited exceptional uniformity, maintaining both an FWHM of 36 nm and a PL QY of 91% (Fig. 11(c)). These significant advances collectively demonstrate that synergistic regulation of temperature, precursor reaction kinetics, and core/shell interface engineering enables precise control over QD size distribution, surface defects, and shell quality, and provides a robust foundation for the morphological engineering of high-performance InP-based QDs.

2.4 Ligand engineering

Surface ligand engineering plays a crucial role in tailoring the properties of InP-based QDs. Post-synthesis treatment of carboxylate-capped InP QDs with alternative ligands enables precise modulation of their stability, optical characteristics, and charge transport properties, ultimately determining their performance in optoelectronic devices[25,42,190,191]. Calvin et al. systematically investigated how the alkyl chain length of native ligands (myristate, palmitate, and stearate) governs exchange thermodynamics[192]. Their work revealed that longer native ligands exhibit stronger endothermicity and slower exchange kinetics due to enhanced van der Waals interactions compared to their shorter counterparts. Notably, the introduction of bent-chain ligands (e.g., oleic acid (OA)) disrupts the tight ordering of linear ligands, increasing the entropy of the ligand shell and thereby driving the exchange reaction (Fig. 12(a)). The chain length of surface ligands critically regulates charge injection and energy transfer in InP-based QLEDs[25,133,191,193,194]. Park et al. revealed that long-chain ligands (such as OA) promote QD aggregation through stronger van der Waals interactions, which increases FRET. In contrast, short-chain ligands (e.g., hexanoic acid (HA)) weaken the coupling effect between QDs, significantly reducing FRET. Meanwhile, these short-chain ligands also decrease the insulating layer thickness on QD surfaces, substantially lowering charge transport barriers and improving charge injection efficiency[194] (Fig. 12(b)). This enhancement contributes to higher luminous efficiency and extended operational lifetime in QLEDs[195,196]. Won et al. further demonstrated that substituting long-chain OA with short-chain HA optimizes the interface between QDs and CTLs, leading to remarkable improvements in charge injection efficiency, device performance, and operational stability in QLEDs[25].

The thiol group (-SH) in thioalcohol, as a typical "soft base", demonstrates strong affinity for "soft acid" metal ions on QD surfaces[197,198]. This characteristic theoretically facilitates the formation of more stable and compact coordination bonds. Consequently, thiol ligands have been widely employed to reduce surface defect density and Auger recombination losses, thereby significantly enhancing the luminous efficiency and stability of QDs[39,42,199,200]. For example, Wang et al. employed cysteamine (CTA) molecules for post-treatment of QD films[42]. The -SH group in CTA binds to undercoordinated sites on the QD surface, effectively passivating defects. Additionally, CTA modification introduces a surface dipole moment, shifting the QD energy levels upward. This adjustment reduces the hole injection barrier while the interfacial dipole simultaneously suppresses excessive electron injection, resulting in more balanced carrier transport. Kim et al. provided further insights into the surface chemistry mechanism of thiol ligands[198]. Their research revealed that during QD surface modification, 1-octanethiol (1-OT) induces proton transfer, converting carboxylate ligands into carboxylic acid and thiolate. The carboxylic acid further dissociates to form carboxylate ligands, which act as X-type ligands with stronger binding affinity to the QD surface. Simultaneously, the thiolate replaces the original $Zn(OA)_2$ and solvent ligands on the QD surface through stronger anionic coordination. This dual mechanism effectively passivates surface defect states, lead-

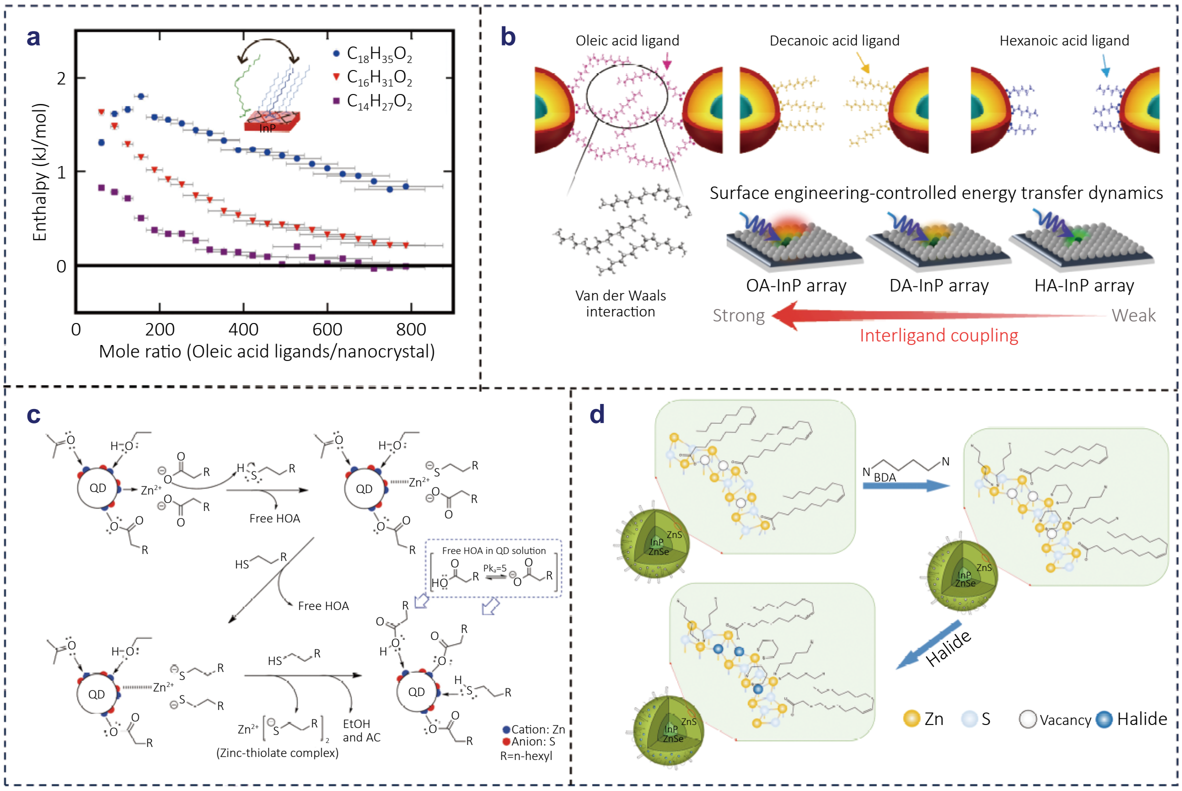

Fig. 12 | (a) Isothermal titration calorimetry data of OA titrations of InP-based QDs capped with stearate, palmitate, or myristate. (b) Schematic diagram of ligand structures on InP/ZnSe/ZnS QDs and chain-length-dependent energy transfer dynamics in ordered assemblies. (c) Schematic motif of Z-type ligand displacement via proton transfer by 1-OT ligand. (d) The schematic diagram of InP-based QDs passivated by the synergistic effect of BDA combined with zinc halides. Figure reproduced with permission from: (a) ref.[192], American Chemical Society; (b) ref.[194], MDPI; (c) ref.[198], John Wiley and Sons; (d) ref.[190], Springer Nature.

ing to a notable enhancement in the optical performance of InP-based QDs and the efficiency of QLEDs (Fig. 12(c)). Zeng et al. established a correlation between electron transfer efficiency and ligand chain length[201]. Their findings indicated that short-chain thiol ligands (e.g., OT) facilitate electron transfer and charge transport more effectively than long-chain thiol ligands (e.g., 1-DDT), thereby enhancing optoelectronic device performance. Similarly, when using benzenethiol for QD modification, the steric hindrance of its benzene ring results in low ligand coverage, poor solubility, and QD aggregation, leading to severely compromised device performance. In contrast, 4-phenylbutane-1-thiol (PBSH) features a butyl chain between its benzene ring and thiol group, providing flexibility and spatial accommodation[202]. This design achieves higher ligand coverage, improved solubility, and enhanced photochemical stability.

The photophysical properties of InP-based QDs are often limited by incomplete surface passivation, primarily caused by steric hindrance and electrostatic repulsion from bulky long-chain ligands[104,203]. These unpassivated surfaces lead to undercoordinated dangling bonds that create trap states, significantly reducing radiative recombination efficiency[204]. To overcome this challenge, researchers have developed innovative strategies employing short-chain organic ligands and inorganic metal halide ligands, which offer enhanced stability and minimal steric hindrance during both synthesis and post-synthesis treatments[25,39,190,205]. A notable advancement was demonstrated by Taylor et al., who achieved efficient surface passivation by combining inorganic $ZnCl_2$ with the short-chain organic ligand 1-OT. This synergistic approach effectively mitigated the steric limitations of conventional long-chain ligands, yielding purified QDs with a PL QY of 71% and a narrow FWHM of 33 nm[39]. Similarly, Chao et al. introduced a bifunctional ligand strategy by replacing native oleic acid with 1,4-butanediamine (BDA). The diamine structure of BDA not only facilitates strong anchoring of zinc atoms on the QD surfaces but also bridges adjacent QDs, thereby improving film morphology and charge transport. Further enhancement was achieved through the incorporation of zinc iodide, which passivated residual surface defects, suppressed hole traps, and extended the PL lifetime[190] (Fig. 12(d)). These developments highlight the critical role of tailored ligand engineering in optimizing the optoelectronic performance of InP-based QDs.

3 Development and challenges of InP-

based QLEDs

By systematically reviewing the basic preparation of InP-based QDs and the fine control of core/shell structure, it can be clearly seen that they play a key role in regulating the photophysical properties of QDs. Such meticulous control not only provides excellent stability and luminescence efficiency for QDs but also lays the foundation for their performance optimization in different application scenarios. Based on the unique advantages of core/shell QDs, researchers have developed diversified application systems including biological imaging[206−208], optoelectronic detection[209,210], and luminescent display[211,212]. Among them, QLEDs have garnered significant attention due to their revolutionary potential in the field of display technology[213,214]. The following will summarize the current development and existing problems of InP-based QLED devices, elucidating the practical application value of core/shell QDs in photoelectric conversion devices.

3.1 Research progress of red, green and blue-emitting InP-based QLEDs

In the earliest reported InP-based QLEDs, InP/ZnSeS QDs with a thick ZnSeS shell acted as the emitting layer[38]. However, the resulting QLEDs exhibited poor EQE of <0.1%, primarily due to the poor electron confinement of ZnSeS. Subsequently, more complicated synthesis processes were developed to synthesize InP-based QDs with large particle size and thick ZnS shells to confine electron wavefunction and suppress the FRET between closely packed QDs, and the red-emitting InP/ZnSe/ZnS QDs and green-emitting InP/GaP/ZnS//ZnS QDs-based QLEDs achieved a record EQE of >6% at that time[164,187] (Fig. 13(a)). Furthermore, by optimizing the carrier transport materials, as well as modifying the growth of core and shell through a stoichiometry-controlled synthesis scheme, Peng et al. demonstrated the high-performance core/shell QDs with near-unity PL QY, monoexponential decay dynamics, and thus the device exhibited a peak EQE of 12.2%, a maximum luminance of over 10,000 cd·m^{-2}, which registered a new record for InP-based QLEDs[185] (Fig. 13(b)). Excitingly, this record was recently refreshed by Won et al., who adopted HF to etch out the oxidative InP core surface and high-temperature ZnSe growth to suppress energy transfer and Auger recombination, and thus obtained InP/ZnSe/ZnS QDs with near-unity PL QY. By further replacing surface ligand with a shorter one for better charge injection, the optimized QLEDs showed a maximum luminance of 100,000 cd·m^{-2}, a peak EQE of 21.4%, and an extremely long T_{50} lifetime of 1,000,000 h at 100 cd·m^{-2} [25] (Fig. 13(c)). However, the peak EQE reported in previous works is usually achieved at a very low voltage (< 3 V) and low luminance (< 2000 cd·m^{-2})[25,86,185,187,215−217]. To address the problem, Li et al. thoroughly investigated the impacts of intrinsic electron delocalization and field-enhanced delocalization on exciton dynamics in InP-based QDs with different surroundings. Finally, a breakthrough EQE of 22.56% was achieved by reducing the effective E-field (at 2 V), and a record luminance of 136,090 cd·m^{-2} was achieved by suppressing the field-enhanced electron delocalization with an ultra-thick shell[154] (Fig. 13(d)).

Despite the rapid development of red-emitting InP-based QLEDs, the development of blue and green-emitting QLEDs is relatively slow. To elucidate the current state of the technology, we summarized the significant progress in the improvement of the performance of red, green, and blue-emitting InP-based QLEDs in Table 1, Table 2, and Table 3, respectively. Notably, blue-emitting InP-based QLEDs were not obtained until 2017[218], and even by 2022, the peak EQE remained as low as 2.8% —achieved through optimization strategies such as employing a thin hole transport layer (HTL), a high-refractive-index substrate, and substrate surface roughening[219]. In 2025, Yuan et al. utilized Cl$^-$ to balance the growth kinetics of different crystal facets of InP cores, enabling uniform shell epitaxy and producing QDs with reduced interfacial defects and elevated energy levels, ultimately achieving EQE of 4.1%[43]. Furthermore, the maximum luminance and operational lifetime of blue-emitting devices remain limited, reaching only 3,120 cd·m^{-2} and 228 h (at 100 cd·m^{-2}), respectively[165,220].

For green-emitting InP-based QLEDs, after 10 years of development from the first report of green-emitting InP-based QLEDs in 2011[38] to 2021[190], a peak EQE (16.3%) exceeding 15% for green-emitting QLEDs was achieved for the first time by modifying the InP/ZnSe/ZnS QD emitting layer with various alkyl diamines and zinc halides, which decreased electron mobility and enhanced hole transport (Fig. 14(a)). For practical displays, both high efficiency, high luminance, and exceptional operational lifetime are equally crucial. To address the lifetime challenge, an ultra-thin molybdenum trioxide (MoO_3) electric dipole layer was inserted at the interface of the hole injection layer (HIL) and HTL to form a positive built-in electric field due to its deep conduction band level. The result indicated that the strong electric fields were instrumental in efficient hole hopping and increasing the carrier recombination rate. Consequently, the green-emitting InP-based QLEDs achieved a recorded maximum luminance of 52,730 cd·m^{-2}. However, the T_{50} at 100 cd·m^{-2} was only 280.75 h[221] (Fig. 14(b)). Furthermore, by using ZnO/ZnS cascaded electron transport layer (ETL), electron injection is reduced and the exciton quenching is suppressed, resulting in an improved charge balance in the QD layer, and a long lifetime of 60,255 h at 100 cd·m^{-2} [222] (Fig. 14(c)). Despite these improvements, the performance metrics still lag behind those of red-emitting InP-based QLED counterparts. Therefore, by utilizing electrically excited transient absorption spectroscopy (EETA), we found that the low performance of green-emitting InP/ZnSeS/ZnS-based QLEDs originates from the ZnSeS interlayer, which imposes a high injection barrier, limiting

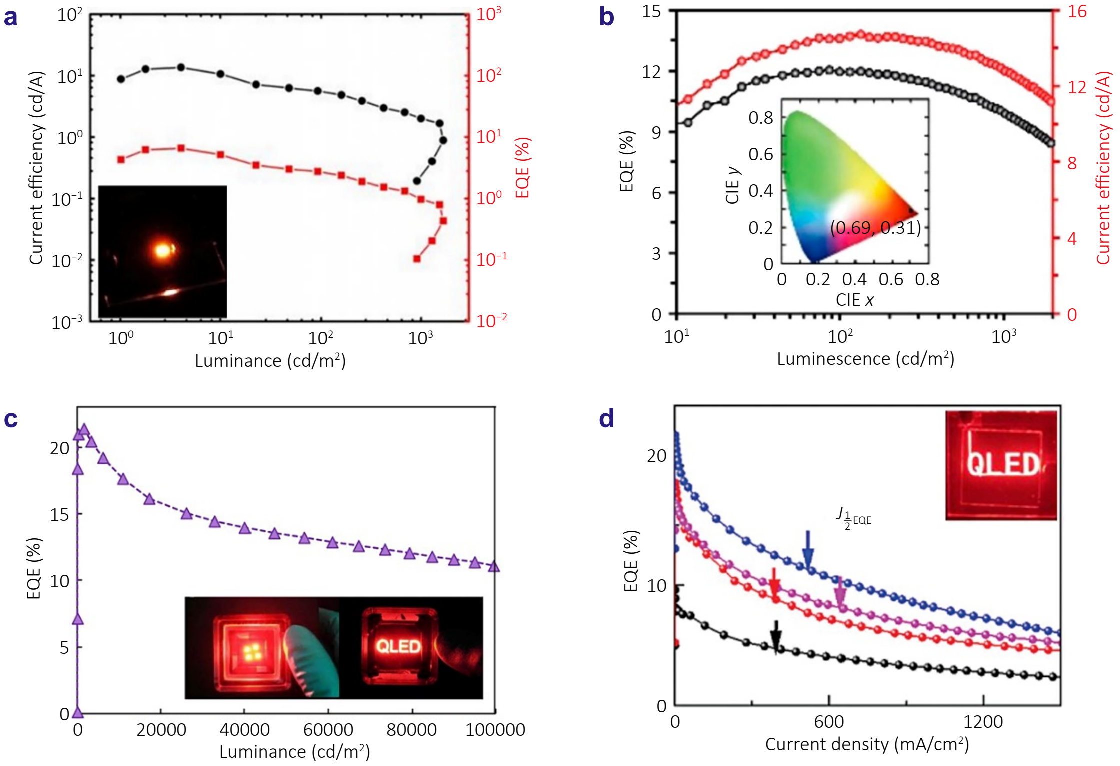

Fig. 13 | (a) Current efficiency and EQE versus luminance of the device. Inset: photograph of QLED. (b) EQE and current efficiency versus luminance of the optimal device. Inset: corresponding CIE coordinates. (c) EQE versus luminance of the optimal device. Inset: photographs of four-pixel QLED and text-patterned QLED. (d) EQE versus current density characteristics of the QLEDs fabricated from InP/ZnSe with different shell thicknesses. The short arrows show the current density at which the EQE decreased to half of the maximum EQE. Inset: photograph of text-patterned QLED. Figure reproduced with permission from: (a) ref.[187], (b) ref.[185], American Chemical Society; (c) ref.[25], Springer Nature; (d) ref.[154], John Wiley and Sons.

the electron concentration and trap saturation. To overcome this limitation, we replaced the conventional ZnSeS interlayer with an optimized, thickened ZnSe interlayer. This modification, supported by both experimental results and theoretical simulations, demonstrated simultaneous improvement in electron injection efficiency and reduction of leakage current. Therefore, an exceptional EQE of 26.68%, a record-breaking luminance of 270,000 cd·m^{-2}, and an impressive T_{95} operational lifetime of 1,240 h at an initial brightness of 1,000 cd·m^{-2} in green-emitting InP-based QLEDs emitting at 543 nm were achieved, representing the current world record in the field[26] (Fig. 14(d)).

3.2 Challenging of InP-based QLEDs

However, for further applications in ubiquitous information devices, such as large digital signage, window-integrated transparent information panels, and augmented reality (AR)/virtual reality (VR) devices, their pioneering applications require further innovation. The outdoor displays under intense sunlight should be operated at a high luminance of > 100,000 cd·m^{-2}. Unfortunately, although luminance >100,000 cd·m^{-2} has been reported for red and green-emitting InP-based QLEDs, such a high brightness is hardly practical due to the inferior device efficiency and stability at those levels[25,26,42,223]. Therefore, increasing the operational lifetime and efficiency under high brightness for red, green, and blue-emitting InP-based QLEDs is urgently needed. In order to improve device performance, it is still necessary to understand the reasons behind it.

(1) Challenges in achieving high-performance EL with small QDs: InP-based QDs with PL QYs exceeding 90% typically measure below 10 nm in size[185,187,190,221]. However, their EL performance suffers from poor stability. A key issue is that EL operation requires charge densities approximately four orders of magnitude higher than those needed for PL to achieve equivalent brightness levels. This significantly increases the likelihood of nonradiative Auger recombination processes, which in turn accelerate QD degradation. As a result, the rapid aging of these QDs under EL conditions severely limits their practicality for EL applications.

(2) Compared to Cd-based QDs, which have a conduction band (<−4.0 eV) and valence band (<−6.0 eV)[11−13], InP-based QDs exhibit relatively shallow energy levels, with their conduction band and valence band positioned at −3.0 eV to −3.7 eV and −5.1 eV to −5.7 eV, respectively[25,26,43]. So, the barrier potential (≈1 eV) between the conduction band of InP-based QD and lowest unoccupied molecular orbital

Table 1 | Summary of PL and EL parameters for red-emitting InP-based QLEDs.[a]

QD structure	PL/FWHM (nm)	PL QY (%)	Size (nm)	Device structure	EL/FWHM (nm)	EQE (%)	L (cd·m^{-2})	CE (cd/A)	Ref.
InP/ZnSeS/ZnS	607/63	82	7.2	ITO/PEDOT:PSS/TFB/QDs/ZnO/Al	619/-	2.5	2,849	4.2	ref.[242]
InP/ZnSe/ZnS	607/48	73	15.0	ITO/ZnO/QDs/CBP/HATCN/Al	607/48	6.6	1,600	13.6	ref.[187]
InP/ZnSe/ZnS	625/39	45	-	ITO/PEDOT:PSS/Poly-TPD/QDs/TPBi/LiF/Al	628/50	-	230	0.85	ref.[40]
InP/ZnSe/ZnS	618/42	93	7.8±0.5	ITO/PEDOT:PSS/poly-TPD/QDs/ZnMgO/Ag	630/-	12.2	>10,000	14.7	ref.[185]
InP/ZnSe/ZnS	626/38	80	-	ITO/ZnMgO/QDs/TCTA/TAPC/HATCN/Al	-/-	10.2	-	10.8	ref.[243]
InP/ZnSe/ZnS	630/35	~100	10.9	ITO/PEDOT:PSS/TFB/QDs/ZnMgO/Al	-/-	21.4	100,000	-	ref.[25]
InP/ZnS	630/-	54	7.6±0.9	ITO/PEDOT:PSS/TFB/QDs/ZnMgO/Al	633/-	4.24	5,595	3.59	ref.[217]
InP/ZnSeS/ZnS	609/53	77	6.3	ITO/PEDOT:PSS/F4-TCNQ/TFB/QDs/ZnMgO/Al	-/-	3.78	1,234	5.10	ref.[244]
-	610/49	32		ITO/ZnO/PEI/QDs/TPBi/CBP/MoO_3/Al	-/-	6.32	>1,000	8.54	ref.[215]
InP/ZnSe/ZnS	632/36	92	9.58	ITO/ZnMgO/QDs/TCTA/PCzAC/DBTA/PCBBiF/HATCN/Al	~660/38	21.8	23,300	23.46	ref.[245]
InP/ZnSeS/ZnS	616/63	81.8	7.33	ITO/PEDOT:PSS/F4-TCNQ/TFB/QDs/Cl@ZnMgO/Al	-/-	4.0	1,977	6.3	ref.[199]
InP/ZnSe/ZnS	630/45	-	-	ITO/PEDOT:PSS/TFB/QDs/ZnMgO@MPTES/ZnMgO/Al	630/52.3	14.70	3,301	19.20	ref.[246]
InP/ZnSe/ZnS	620/60	95		ITO/PEDOT:PSS/TFB/QDs/ZnO/Al	636/60	13.62	6,224	-	ref.[247]
InP/ZnSe/ZnS	630/35	95	10.8±0.9	ITO/PEDOT:PSS/TFB/TPD:QD/ZnMgO/Al	630/34	18.6	128,577	-	ref.[248]
InP/ZnS	626/-	86	-	ITO/NiO_x/Mg-NiO_x/poly-TPD/QDs/ZnMgO/Al	629/46	11.2	29,445	15.6	ref.[249]
InP/ZnSe/ZnS	620/36	>90	12	ITO/PEDOT:PSS/TFB/QDs/ZnMgO/Al	627/-	22.2	>110,000	-	ref.[28]
InP/ZnSe	623/38	92	12.26±2.2	ITO/PEDOT:PSS/TFB/QDs/ZnMgO/Al	-/-	22.56	136,090	26.70	ref.[154]
InP/ZnSe/ZnS	617/45	85	8.9	ITO/PEDOT:PSS/TFB/QDs/ZnMgO/Al	626/-	12.0	16,954	14.1	ref.[250]
InP/ZnSe/ZnS	620/49	90	7.6-7.8	ITO/PEDOT:PSS/TFB/QDs/ZnMgO/TPBi/LiF/Al	624/-	5.07	21,070	5.4	ref.[251]
InP/ZnSe/ZnS	621/44	86	8.8	ITO/PEDOT:PSS/TFB/QDs/ZnMgO/Al	629/50	8.9	13,395	8.8	ref.[252]
InP/ZnSe/ZnS	630/35	90	-	ITO/PEDOT:PSS/NiO_x/Poly-TPD/QDs/ZnMgO/Al	-/-	18.8	22,300	-	ref.[253]
InP/ZnSe/ZnS	-/-	-	-	ITO/ZnMgO/QD/DBTA/PCBBiF/HATCN/Al	-/-	10.2	8,391	9.5	ref.[228]
InP/ZnS	625/43	80	-	ITO/PEDOT:PSS/B-PTAA/QDs/ZMO/Ag	628/-	20.4	24,000	25.3	ref.[254]
InP/ZnSe/ZnS	-/-	-	-	ITO/ZnMgO/QD/DBTA/PCBBiF/HATCN/Al	632/-	16.7	4,878	16.4	ref.[255]
InP/ZnSe/ZnS	630/36	86	-	ITO/ZnO/QD/DBT/PCBBi/HATCN/Al	632/-	10.6	>8,000	10.4	ref.[256]
InP/ZnSe/ZnS	635/42	83.5	8	ITO/PEDOT:PSS/TFB/QDs/ZnMgO/Al	-/-	8.1	17,759	11.1	ref.[257]
InP/ZnSe/ZnS	627/-	-	~10.1	ITO/PEDOT:PSS/poly-TPD/QDs/CNT2T/LiF/Al	635/38	~15	12,000	-	ref.[258]
InP/ZnSe/ZnS	-	-	-	ITO/PEDOT:PSS/TFB/QDs/ZnMgO/Al	628/39	9.6	7,079	12.9	ref.[259]
InP/ZnSe/ZnSeS/ZnS	618/41	96	11.2	ITO/PEDOT:PSS/TFB/QDs/ZMO/Al	624/-	12.39	44,160	19.76	ref.[86]
InP/ZnSe/ZnSeS/ZnS	680/66	95	10.5	ITO/PEDOT:PSS/TFB/QDs/ZnO/Al	683/-	6.5	2,263	-	ref.[260]
InP/ZnSe	625/42	85	-	ITO/ZnO/CBP-QDs/PVK/Wo_3/Au	-/-	11.6	14,600	-	ref.[261]
InP/ZnSe/ZnS	-/-	-	-	Ag:PEI/PEDOT:PSS/TFB/QDs/ZnMgO/Al/Ag	633/36	15.96	25,606	28.04	ref.[262]
InP/ZnSe/ZnS	614/37	>90	12	ITO/PEDOT:PSS/PF8Cz/QDs/ZnMgO/Al	622/40	21.21	1,24,220	27.84	ref.[42]
InP/ZnSe/ZnS	614/37	~92	12	ITO/PEDOT:PSS/PF8Cz/QDs/PVP/ZnMgO/Al	624/41	23.5	4,850@EQE_{max}	37.70	ref.[263]
InP/ZnSe/ZnS	-/-	-	-	ITO/NiO_x/Poly-TPD/QD/ZnMgO/Al	635/-	19.9	45,200	-	ref.[264]
InP/ZnS	625/39	-	8.6	ITO/PEDOT:PSS/MoO_x/TFB/QD/ZnMgO/Al	626/39	17.8	43,567	-	ref.[265]
InP/ZnSe/ZnS	-/-	90	-	ITO/PEDOT:PSS/TFB:$Ir(mppy)_3$/QDs/PVP/ZnMgO/Al	626/38	17.1	43,000	23.6	ref.[266]
-	-/-	-	-	ITO/PEDOT:PSS/TFB/QDs/LiMgZnO/Al	631/44	11.8	7,477	14.3	ref.[267]
-	622/39	83	-	ITO/PEDOT:PSS/TFB/QDs/ZnMgO/Al	-/-	26.6	140,000	-	ref.[268]
-	617/37	-	-	ITO/ZnMgO/QD/TCTA/TAPC/HAT-CN/MoO_3/Al	620/37	11.01	22,692	16.68	ref.[269]
InP/ZnSe/ZnSeS/ZnS	602/52	93	10.8±0.8	ITO/PEDOT:PSS/TFB/QDs/ZnMgO/Al	-/-	11.8	6,325	-	ref.[270]
InP/ZnSe/ZnSeS/ZnS	614/36	>90	11.1	ITO/PEDOT:PSS/PF8Cz/QDs/ZnMgO/Al	628/38	20.9	94,127	25.0	ref.[271]

[a] L: luminance; CE: current efficiency.

Table 2 | Summary of PL and EL parameters for green-emitting InP-based QLEDs.

QD structure	PL/FWHM (nm)	PL QY (%)	Size (nm)	Device structure	EL/FWHM (nm)	EQE (%)	L ($cd \cdot m^{-2}$)	CE (cd/A)	Ref.
InP/ZnSeS	522/70	>50	5.3	ITO/PEDOT:PSS/poly-TPD/QDs/TPBi/LiF/Al	532/70	0.008	-	-	ref.[38]
InP/ZnSeS	-	-	4	ITO/PEDOT:PSS/poly-TPD/QDs/TPBi/LiF/Al	550/55	0.26	700	-	ref.[272]
InP/ZnSeS	500/50	72	4.5	ITO/ZnO/PFN/QDs/TCTA/MoO_3/ Al	518/64	3.46	3,900	10.9	ref.[273]
InP/ZnSe/ZnS	507/46	44	~2	ITO/PEDOT:PSS/poly-TPD/QDs/TPBi/Ca or Ag	521/53	-	448	1.5	ref.[274]
InP/ZnSeS/ZnS	525/65	-	7.4 ± 0.5	ITO/ZnMgO/QDs/TCTA/NPB/HATCN/Al	545/-	~1.5	10,490	4.44	ref.[275]
InP/ZnS	530/55	60.1	4	-	-/-	0.223	160	0.65	ref.[276]
InP/ZnSe/ZnS	533/37	65	-	ITO/PEDOT:PSS/poly-TPD/QDs/TPBi/LiF/Al	532/42	-	100	0.07	ref.[40]
InP/ZnSe/ZnS	556/65	58	-	ITO/PEDOT:PSS/poly-TPD/QDs/ TPBi/Ca or Ag	-/-	5.1	1,900	18.0	ref.[277]
InP/GaP/ZnS/ZnS	527/58	70	7.2±1.3	ITO/PEDOT:PSS/TFB/QDs/ZnO/Al	530/-	6.3	2,938	13.7	ref.[164]
InP/ZnMnS/ZnS	513/62	80	-	ITO/PEDOT:PSS/PVK/QDs/ZnMgO/Al	-/-	2.7	420	-	ref.[180]
-	531/34	82	-	ITO/PEDOT:PSS/poly-TPD/PVK/QDs/ZnMgO/ZnO/Al	-/-	13.6	13,900	-	ref.[278]
InP/ZnSeS	529/41	86	5–6	Ag/MoO_3/TCTA/CzSi/QDs/PFN/ZnO/Al	536/37	2.7	38,800	15.3	ref.[279]
InP/ZnSeS	537/43	82	4–5	ITO/PEDOT:PSS/TFB/QDs/ZnO/Al	545/45	0.904	1,593	2.98	ref.[280]
-	525/40	81	-	ITO/ZnO/QDs:TmPPPyTz/TCTA/MoO_3/Al	530/42	10	-	-	ref.[281]
InP/ZnSe/ZnS	533/36	97		ITO/PEDOT:PSS/TFB/QDs/ZnO/Al	540/40	6.88	4,884		ref.[247]
InP/ZnSeS/ZnS	518/46	67.5	7.0	ITO/PEDOT:PSS/TFB/QDs/ZnMgO/Al	-/-	1.68	725	4.79	ref.[80]
InP/ZnSeS/ZnS	517/45	95	5.38	ITO/ZnMgO/QDs/TCTA/MoO_3/Al	525/-	7.06	1,836	-	ref.[78]
-	533/41	60	-	ITO/ZnO/ZnMgO/QDs/TCTA/ NPB/HATCN/Ag	-/31	4.2	-	30.1	ref.[282]
InP/ZnSe/ZnS	535/39	86	8.6±1.2	ITO/ZnMgO/QDs/TCTA/MoO_3/Al	545/-	16.3	12,646	57.5	ref.[190]
InP/ZnSe/ZnS	-/40	87	7.2	ITO/PEDOT:PSS/TFB/QDs/MZO:PVP/Al	-/-	6.2	6,600	24.03	ref.[161]
InP/ZnSeS/ZnS	528/35	97	11.5	ITO/PEDOT:PSS/TFB/QDs/ZnMgO/Al	532/45	15.2	2,300	-	ref.[41]
InP/ZnSe/ZnS	531/38	87	8.6	ITO/PEDOT:PSS/TFB/QDs/ZnMgO/Al	545/-	9.3	13,445	36.6	ref.[250]
InP/ZnSe/ZnS	-/36	91	5.66±0.83	ITO/PEDOT:PSS/TFB/PVP/QDs/ZnO/Al	-/-	10.6	15,606	40.7	ref.[186]
InP/ZnSe/ZnS	526/46	90	-	ITO/PEDOT:PSS/TFB/QDs/ZnMgO/Al	535/49	7.8	4,955	25.8	ref.[283]
In(Zn)P/ZnSeS/ZnS	528/38	89	6.7	ITO/ZnO/ZnS/QD/DBTA/PCBBiF/HATCN/A	530/-	10.8	1,756	37.5	ref.[222]
InP/ZnSe/ZnS	535/43	54	-	ITO/PEDOT:PSS/PVK/QDs/ZnMgO/Al	538/-	15	10,010	-	ref.[284]
InP/ZnSeS	529/-	80	7	ITO/MoO_x/TCTA/PPO21/CBP:$Ir(ppy)_3$/TPBi/LiF/Al	533 / 27	9.64	40,700	68.0	ref.[285]
-	~532/41	~82	7.5–8.0	ITO/Cu:PMA/TFB/BFTP/QDs/ZnMgO/Al	535/43	8.46	18,356	-	ref.[286]
InP/ZnSeS/ZnS	526/36	91	6.31±0.48	ITO/PEDOT:PSS/Poly-TPD/QDs/ LiF/ZnMgO/Al	525/42	5.56	2,798	-	ref.[76]
InP/ZnSe/ZnS	532/36	90	6.5±0.2	ITO/PEDOT:PSS/PTAA/QDs/ZnMgO/Al	539/46	13.8	16,788	52.2	ref.[287]
InP/ZnS	-/-	-	5.0±0.2	ITO/LiF/PEDOT:PSS/PVK/QDs/ZnMgO/Al	530/-	9.14	32,380	-	ref.[288]
InP/ZnSeS/ZnS	-/33.7	95	-	ITO/PEDOT:PSS/TFB/QD/ZnMgO/Al	-/-	14.3	11,920	39.0	ref.[289]
InP/ZnS	525/-	70.3	4.8±0.2	ITO/PEDOT:PSS/PVK/QDs/ZnMgO/Al	535/-	7.39	52,730	-	ref.[221]
InZnP/ZnSeS/ZnS	532/39	79	-	ITO/s-FZO/QDs/DBTA/ PCBBiF/HAT-CN/Al	-/-	20.07	8,635	68.92	ref.[290]
InP/ZnS	532/43	67		ITO/NiO/PEDOT:PSS/poly-TPD/QDs/ZnMgO/Al	536/48	6.75	2,493	12.73	ref.[291]
InP/ZnSe/ZnS	534/44	91	8.1±1.0	ITO/PEDOT:PSS/PF8Cz/QDs/ZnMgO/Al	-/-	12.74	175,000	54.56	ref.[55]
InP/ZnSeS/ZnS	538/39	96	8.0	ITO/PEDOT:PSS/PF8Cz/QDs/ZnMgO/Al	-/-	21.43	255,985	90.45	ref.[223]
InP/ZnSe/ZnS	540/35	95	11.0±2.5	ITO/PEDOT:PSS/PF8Cz/QDs/ZnMgO/Al	543/-	26.68	277,000	112.56	ref.[26]
InP/ZnSeS/ZnS	525/36	93	8.9±0.9	ITO/PEDOT:PSS/TFB/QDs/ZnMgO/Al	-/-	4.6	13,000	-	ref.[292]
InP/ZnSe/ZnSeS/ZnS	509/50	88	6.9±0.1	ITO/PEDOT:PSS/TFB/QDs/ZnMgO/Al	-/-	7.5	3,842	-	ref.[270]
InP/ZnSeS/ZnS	-/-	>90	-	ITO/PEDOT:PSS/PF8Cz/QDs/ZnMgO/Al	-/-	26.3	-	108.3	ref.[293]

Table 3 | Summary of PL and EL parameters for blue-emitting InP-based QLEDs.

QD structure	PL/FWHM (nm)	PL QY (%)	Size (nm)	Device structure	EL/FWHM (nm)	EQE (%)	L (cd·m^{-2})	CE (cd/A)	Ref.
InP/ZnS	477/44	76	6.68±0.46	ITO/ZnMgO/QDs/CBP/MoO_3/Al	488/45	-	90	-	ref.[218]
InP/GaP/ZnS/ZnS	480/45	81	7.0±0.9	ITO/PEDOT:PSS/TFB/QDs/ZnO/Al	488/50	1.01	3,120	-	ref.[165]
InGaP/ZnSeS/ZnS	465/45	82	5.4–5.7	ITO/PEDOT:PSS/PVK/QDs/ZnMgO/Al	469/-	2.5	1,038	3.8	ref.[171]
InP/ZnS/ZnS	468/47	45	6.75±0.54	ITO/PEDOT:PSS/PVK/QDs/ZnMgO/Al	485/-	1.7	140	-	ref.[178]
InP/GaP/ZnS	485/52	45	6.3	ITO/PEDOT:PSS/PVK:poly-TPD/QDs/ZnO/Al	491/66	1.0	1,045	3.6	ref.[294]
InP/ZnSe/ZnS	465/42	43	4.8	ITO/PEDOT:PSS/TFB/QDs/ZnO/Al	484/46	1.47	125	-	ref.[247]
InP/ZnS/ZnS	468/47	45	6.75±0.54	ITO/PEDOT:PSS/MoO_3/PVK/QDs/ZnMgO/Al	485/-	2.1	165	-	ref.[295]
InGaP@ZnS	486/46	65	5.9	ITO/ZnO/PFN/QDs/TCTA/MoO_3/Al	491/-	0.20	74	-	ref.[296]
InP/ZnS	483/49	52	4.95±0.73	ITO/PEDOT:PSS/TFB/QDs/ZnMgO/Al	487/55	1.4	1,162	-	ref.[297]
InP/GaP/ZnS	484/45	71	5.9±0.9	ITO/PEDOT:PSS/PVK/QDs/TmPyPb/LiF/Al	-/-	0.09	690	0.15	ref.[298]
InP/ZnS	482/-	-	-	ITO/PEDOT:PSS/MoO_3/TFB/QDs/ZnMgO/Al	492/-	2.82	421	-	ref.[219]
InP/ZnS/ZnS	474/-	93	6.2±0.52	ITO/PEDOT:PSS/TFB/QDs/ZnMgO/Al	488/-	2.6	422	-	ref.[299]
InP/ZnS/ZnS	465/38	96	10.6	ITO/PEDOT:PSS/TFB/QDs/ZnO/Ag	472/43	0.15	91	0.19	ref.[300]
In(ZnGa)P/ZnSeS/ZnS	457/52	84	6.2	-	-	-	-	-	ref.[301]
InGaP/ZnS	475/56	42	-	-	-	-	-	-	ref.[162]
InP/ZnS/ZnS	452/51	-	-	ITO/PEDOT:PSS/TFB/IQDs/ZnMgO/Al	468/-	0.8	275	-	ref.[302]
InP/ZnS	474/45	73	4.45±0.82	ITO/PMA/TFB/QDs/ZnMgO/Al	483/	2.38	2,693	-	ref.[220]
InGaP/ZnS	470/40	67	6.34±0.60	ITO/ZnMgO/QDs/ CBP/MoOx/Al	477/-	0.56	-	-	ref.[303]
InP/ZnS	468/43	75	6.98±0.73	ITO/PEDOT:PSS/PF8Cz/QD/ZnMgO/Al	485/47	4.1	624	7.2	ref.[43]

(LUMO) (−2.2 eV−2.5 eV) of the commonly-used HTL materials (such as poly[(9,9-dioctylfluorenyl-2,7-diyl)-co-(4,4'-(*N*-(4-sec-butylphenyl) diphenylamine)] (TFB), poly[bis(4-phenyl)(4-butylphenyl)amine] (Poly-TPD), poly(9,9-dioctylfluorenyl-2,7-diyl)-alt-(9-(2-ethylhexyl)-carbazole-3,6-diyl)) (PF8Cz), etc.) is much less than that of Cd-based QDs (>1.5 eV)[25,26,224,225]. Moreover, InP-based QDs possess a smaller electron effective mass (0.07 m_0 versus 0.13 m_0) and a narrower bandgap (1.35 eV versus 1.74 eV) compared to their Cd-based counterparts[33]. Therefore, the effects of quantum confinement and blocking of electrons enabled by the shell and the HTL are both weaker, leading to more pronounced electron leakage and stronger coupling with trap states under an electric field. Especially under high voltage, electrons can be injected into higher energy states of QDs and remain trapped due to the phonon bottleneck. If these electrons can be well confined by the shell of QDs, they will relax to the ground state once they meet holes. However, the injected electrons cannot be well confined in InP-based QDs due to the shallow conduction band of InP-based QDs[42,222], leading to the injection of these high-energy electrons into the HTL. This electron leakage triggers irreversible HTL degradation through redox reactions, which subsequently elevates the operational voltage and leads to significant efficiency roll-off at high luminance levels, ultimately shortening the device's operational lifetime[13]. Moreover, the disparity in electron and hole transport mobilities results in unbalanced charge transport, allowing excess charges to traverse all device layers without recombination, generating substantial Joule heat. The thermal degradation will vary the electrical properties of the device, destroying the charge balance and shifting the recombination zone, and thus reducing the device's efficiency and lifetime[11].

(3) Significant advancements have been made in enhancing the PL QY of QDs and improving the radiative recombination rate within devices. However, the EQE remains substantially lower than their internal quantum efficiencies, primarily due to poor light extraction efficiency. Among the dominant loss mechanisms, waveguiding and substrate modes play a crucial role, arising from the refractive index mismatch between the metal electrode/glass substrate (lower refractive indices) and the functional layers (HTL, emitting layer, ETL). Additionally, a substantial portion of light is lost through total internal reflection (TIR) at material interfaces. When photons generated in high-refractive-index layers encounter low-refractive-index media (e.g., CTL/charge injection layers (CIL) to air), only those incident below the critical angle can escape. Consequently, the majority of internally generated photons become trapped, either propagating as waveguide modes, being absorbed by metallic electrodes, or dissipating as surface plasmon polaritons (SPP) resonance losses[226].

(4) The luminescence and degradation mechanisms of both red and green-emitting Cd-based QLEDs, as well as

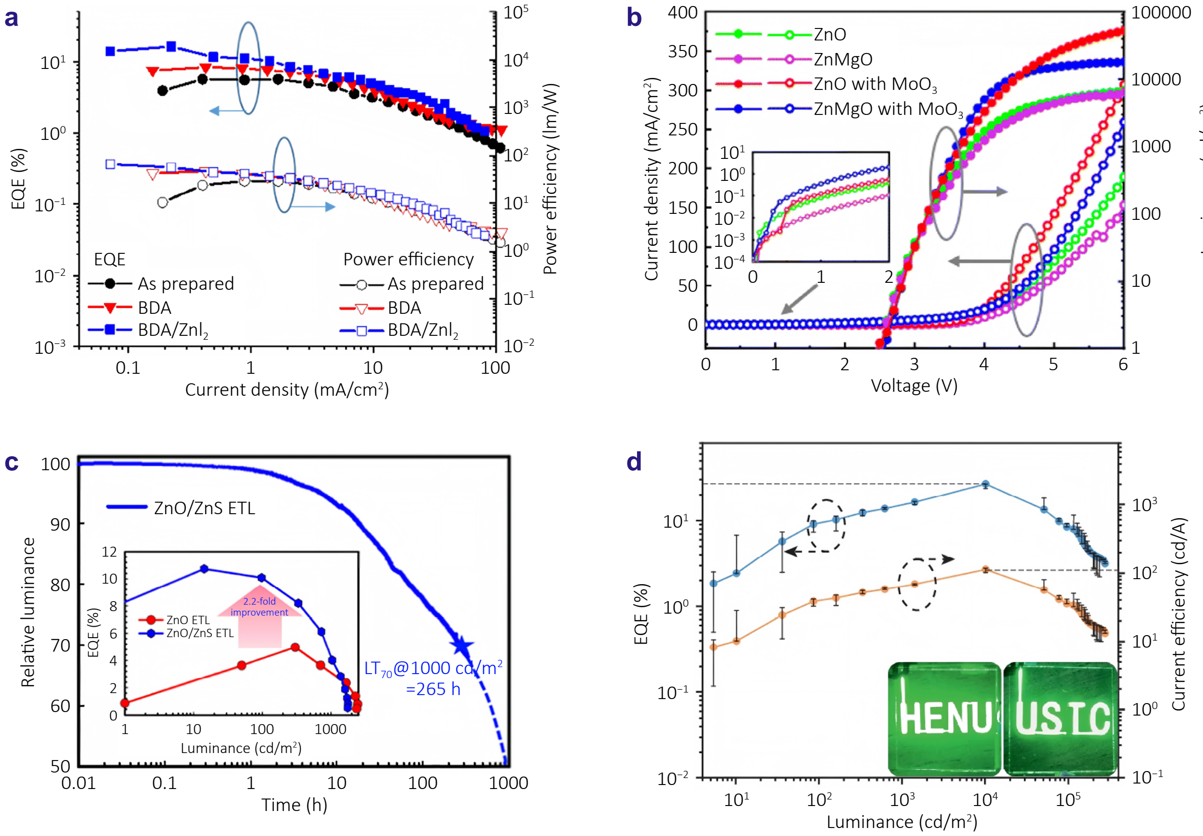

Fig. 14 | (a) EQE and power efficiency versus current density of the device. (b) Current density and luminance versus voltage of the device. Inset: current density versus voltage of the device in log scale in the low-voltage region. (c) Operational lifetime versus time of the device. Inset: EQE versus luminance of InP-based QLEDs using a ZnMgO ETL or a ZnO/ZnS ETL. (d) EQE and current efficiency versus luminance of the device. Inset: photographs of text-patterned QLEDs. Figure reproduced with permission from: (a) ref.[190], Springer Nature; (b) ref.[221], Royal Society of Chemistry; (c) ref.[222], American Chemical Society; (d) ref.[26], Springer Nature.

blue-emitting Cd-based QLEDs, have been extensively studied[13,224,227]. In contrast, the degradation pathways of InP-based QLEDs remain less understood and require further systematic exploration. Currently, the degradation of InP-based QLEDs may be attributed to several distinct mechanisms: exciton and charge-induced degradation, ligand detachment or charge injection imbalance. For example, Kwon et al. reported that the degradation of InP-based QLEDs is caused by the greater vulnerability of InP-based QDs to exciton and electron-exciton stress compared to the Cd-based QDs under an electric field, which significantly enhances the non-radiative Auger recombination process[228]. In addition, Lee et al. found that the evidence of InP-based QLED degradation is characterized by ligand detachment from the QD surface and deterioration of the hole-transporting material due to excessive electrons[229]. However, Chen et al. presented contradictory evidence suggesting that hole over-injection, rather than electron-related effects, dominates the degradation process in InP-based QLEDs[230]. These conflicting observations highlight a critical knowledge gap in our understanding of the fundamental degradation mechanisms in InP-based QLEDs. The current lack of a comprehensive theoretical framework significantly hinders the rational design and development of high-performance, stable InP-based QLEDs.

(5) The relatively poor performance of blue-emitting InP-based QLEDs is primarily constrained by both the intrinsic material properties and device-level mismatches[231]. To achieve blue emission, the QDs must be extremely small, resulting in a large specific surface area and a significant increase in surface defect states, which act as severe non-radiative recombination centers and substantially reduce luminescence efficiency[107,109]. Furthermore, the extremely small size induces high surface curvature and accumulated lattice mismatch strain, leading to defect generation during thick-shell epitaxial growth and making effective passivation challenging[165,178]. On the device level, their wide bandgap results in a deeper valence band and a shallower conduction band, exacerbating the energy level misalignment with adjacent CTLs[43,165]. This intensified mismatch creates significant charge injection barriers and imbalance, causing substantial leakage current and severe

non-radiative recombination, which ultimately degrades device efficiency. These issues collectively form the core bottlenecks in improving the performance of blue-emitting InP-based QLEDs.

4 Perspectives of InP-based QDs and corresponding QLEDs

For commercial displays, high efficiency and an extreme level of lifetime under harsh conditions as well as process reproducibility are critical for practical purposes. An important parameter to evaluate the efficiency of a QLED is η_{EQE}, which can be defined as $\eta_{EQE}= \eta_{rad}{}^{*}\eta_{rec}{}^{*}\eta_{ext}=$ IQE$^{*}\eta_{ext}$, where η_{rad} is the PL QY, η_{rec} is the recombination rate, η_{ext} is the light extraction rate (or light coupling), and IQE is the internal quantum efficiency[232,233]. Therefore, to maximize the η_{EQE} of QLEDs, the PL QY of QDs should obtain the values of unity, the number of effective electrons and holes injected into the emissive layers should be balanced to enhance the radiative recombination, and the released photons should be effectively extracted.

4.1 Fabrication of large-sized InP-based QDs with near-unity PL QY

To improve the electroluminescence stability of QDs, it is essential to increase their size. However, achieving a high PL QY in such large-sized QDs requires the careful design of key parameters to suppress non-radiative recombination pathways within the emitting layer. This can be accomplished through three primary strategies: First, defect reduction is critical. By optimizing synthetic conditions and designing appropriate core/shell structures, surface, interface, and crystalline defects can be minimized, thereby reducing nonradiative recombination centers[140]. Additionally, controlling graded or alloyed compositions and adjusting shell thickness can effectively suppress FRET between QDs[11,234]. Second, the charge injection balance and carrier recombination efficiency must be improved. Lowering the energy barrier for electron and hole injection helps achieve balanced charge distribution, mitigating Auger recombination. In addition, suppressing electron leakage is beneficial for improving carrier recombination efficiency, reducing the generation of Joule heating and the efficiency losses at high brightness levels[224,234]. Third, surface ligand engineering plays a vital role. Proper ligand selection and optimization can tailor energy levels, passivate surface defects, enhance QD stability, and balance charge injection in devices[39,42,190]. These modifications lead to significant improvements in both device efficiency and operational lifetime.

4.2 Increase the radiative recombination rate in the emitting layer

To realize long operational stability at high brightness, it is necessary to carefully select materials or the device structure to reduce Auger recombination, heat accumulation, and electron leakage simultaneously. The reported study found that tailoring core/shell QD heterostructures—particularly those with a smoothed core/shell interface or coating a thick shell—could reduce the overlap between the initial and the final state of the carrier excited during Auger recombination, and thus significantly suppress this non-radiative recombination pathway[235]. Minimizing heat accumulation is also an essential factor in prolonging the operation lifetime of QLEDs, which can be achieved by obtaining high luminance and high efficiency at low driving voltage. To achieve this purpose, enhancing the quasi-Fermi level splitting by using monolayers of large QDs (>20 nm) can increase the electron population per QD, leading to the improvement of radiative recombination and thus the luminance and efficiency at low driving voltage (Fig. 15(a)). To suppress electron leakage, it is necessary to insert an interface modification layer or increase the LUMO of HTL, as well as modify the shell materials of InP-based QDs to improve the energy level matching with the HOMO of the HTL. Additionally, enhancing electron injection by modifying electron transport materials is necessary to fill the defect states in the QD emitting layer, thereby enhancing the carrier radiative recombination efficiency (Fig. 15(b)).

4.3 Enhancing the light extraction efficiency in device

To improve the light extraction rate and efficiency of QLEDs, the most efficient approach is to decrease the refractive indices of the functional layer sandwiched between the anode and the cathode, or increase the refractive indices of the substrates. Another way to extract the trapped light is to optimize device structure, integrate the devices with a scattering layer or adopt a top-emitting structure, and so on. However, although significant improvement of device performance could be obtained based on the optimization of device structure, whether the luminous efficiency can be improved from directional light emission of QD materials is the fundamental solution, which can be realized by the oriented self-assembly[226]. On the one hand, QDs with oriented self-assembly can be realized with anisotropic shapes featuring either large aspect ratios or well-defined flat crystalline facets, such as nanorods, nanoplatelets, and QDs with flat exposed facets, which enable increased photon emission perpendicular to the device substrate, and thus enhance the photon out-coupling[236–238]. On the other hand, dipole-dipole interaction, which depends on the QD's size and chemical composition, is another important force that affects the self-assembly of nanocrystals. A previous study found that more ionic compounds lead to larger permanent dipole moments that facilitate the QD orientation[239]. This is an effective strategy to promote directional emission from each QD (Fig. 15(c)).

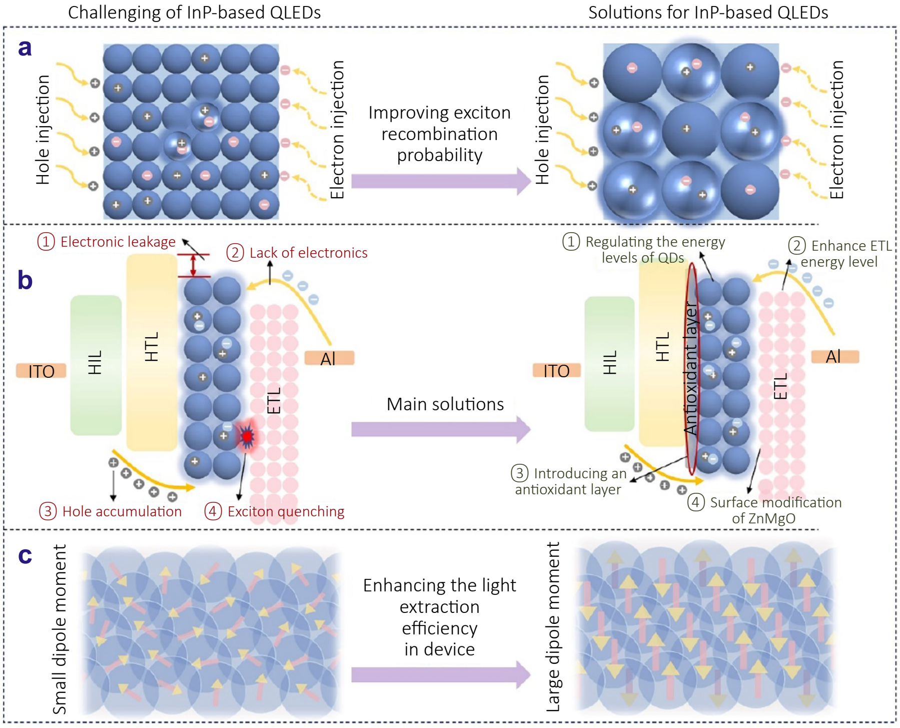

Fig. 15 | (a) Schematic diagram of improving exciton recombination probability through large-sized QDs. (b) The main problems and solutions affecting the performance of InP-based QLEDs. (c) Schematic diagram of the reverse parallel orientation arrangement of QDs with a permanent dipole moment.

4.4 Resolving the luminescence and aging mechanisms in InP-based QLEDs

The unresolved luminescence and aging mechanisms in InP-based QLEDs remain critical challenges hindering their commercialization and long-term stability. A comprehensive understanding of the interplay between QD surface chemistry, defect states, interfacial degradation under electrical stress and transport characteristics of carriers in devices is essential to develop stable InP-based QLEDs. For instance, in-situ X-ray photoelectron spectroscopy (XPS) and ultraviolet photoelectron spectroscopy (UPS) are necessary to directly track the chemical state evolution (e.g., oxidation of In/P, ligand desorption) and the shifts of energy level at the interface of QD/charge transport layer. This is crucial for identifying electrochemical reactions and interfacial dipole formation. Time-resolved and spatially-resolved EL mapping are necessary to detect the emergence of non-radiative recombination centers under electrical stress. Grazing-incidence small-angle X-ray scattering (GISAXS) can monitor the nanoscale morphological stability of the QD film under electrical stress, detecting QD aggregation or layer segregation. Conductive atomic force microscopy (C-AFM) and kelvin probe force microscopy (KPFM) can map the variations in current injection and surface potential across the QD layer, which helps in identifying "hot spots" for leakage current and localized degradation. The above advanced characterization techniques coupled with theoretical modeling, such as DFT, provide definitive guidelines for the design of core/shell structure, stable surface passivation and optimized device interfaces, ultimately paving the way for the commercialization of high-performance InP-based displays.

4.5 Enhancing the performance of blue-emitting InP-based QLEDs

To achieve high-performance blue-emitting InP-based QLEDs, coordinated optimization across the following three aspects is essential. First, precise control over synthesis conditions and precursor composition enables uniform manipulation of the core size, which serves as the foundation for obtaining narrow emission spectra[178,240]. The introduction of Ga to form InGaP alloys allows for bandgap widening while maintaining an appropriate QD size, thereby enabling stable blue emission[171]. Second, gradient shell structures should be developed to progressively mitigate lattice strain, thereby promoting epitaxial growth of thick and intact shells and achieving effective passivation of surface[140,147]. Finally, to address their wide bandgap characteristics, the combination of ligand-mediated energy level modulation and well-matched CTL designs optimizes charge carrier injection balance, suppresses leakage current and non-radiative recombination, and ultimately enhances device efficiency and stability[43,231,241].

5 Conclusions

In summary, this review provides a comprehensive analysis of the nucleation mechanisms underlying InP core formation and presents key optimization strategies for high-performance InP-based core/shell QDs and their corresponding QLEDs. We strongly believe that the full process of fine-tuning from materials to devices is necessary to realize high efficiency, high luminance, and long-lifetime InP-based QLEDs. Accordingly, we summarize the enhancement strategies from synthesis to device, including InP core engineering, core/shell engineering, ligand engineering and device architecture engineering. Although these strategies have improved the performance of InP-based QLEDs to some extent, there is still a significant gap in performance for practical display applications. Thus, we critically evaluate the remaining commercialization challenges of InP-based QLEDs in next-generation display and optoelectronic technologies, including the difficulty in achieving high-performance EL with small QDs, several issues caused by imbalanced carrier injection (namely, Auger recombination, Joule heating, and low carrier recombination efficiency), still-unresolved luminescence and aging mechanism, and the poor performance of blue-emitting InP-based QLEDs. Finally, we proposed potential pathways to overcome current limitations, providing insights for the future development of InP-based QLED technologies. To realize high-performance InP-based QLEDs, the following issues must be addressed: how to fabricate large-sized InP QD with near-unity PL QY, how to enhance the radiative recombination rate in the emitting layer, how to improve the light extraction efficiency in device, how to elucidate the luminescence and aging mechanisms in InP-based QLEDs through advanced characterization techniques, and how to enhance the performance of blue-emitting InP-Based QLEDs. In the near future, researchers will overcome existing limitations and usher in the maturation of InP-based QLED technology, which will firmly establish their critical role in lighting, display, and emerging applications.

References

1. Mashford BS, Stevenson M, Popovic Z et al. High-efficiency quantum-dot light-emitting devices with enhanced charge injection. *Nat Photonics* **7**, 407–412 (2013).
2. Wang SB, Li Y, Chen J et al. Development and challenges of indium phosphide-based quantum-dot light-emitting diodes. *J Photochem Photobiol C Photochem Rev* **55**, 100588 (2023).
3. Efros AL, Brus LE. Nanocrystal quantum dots: from discovery to modern development. *ACS Nano* **15**, 6192–6210 (2021).
4. Chen O, Wei H, Maurice A et al. Pure colors from core-shell quantum dots. *MRS Bull* **38**, 696–702 (2013).
5. Li B, Chen F, Xu HY et al. Advances in understanding quantum dot light-emitting diodes. *Nat Rev Electr Eng* **1**, 412–425 (2024).
6. Nguyen HA, Dixon G, Dou FY et al. Design rules for obtaining narrow luminescence from semiconductors made in solution. *Chem Rev* **123**, 7890–7952 (2023).
7. Zhang ZX, Ye YX, Pu CD et al. High-performance, solution-processed, and insulating-layer-free light-emitting diodes based on colloidal quantum dots. *Adv Mater* **30**, 1801387 (2018).
8. Dai XL, Deng YZ, Peng XG et al. Quantum-dot light-emitting diodes for large-area displays: towards the dawn of commercialization. *Adv Mater* **29**, 1607022 (2017).
9. Dai XL, Zhang ZX, Jin YZ et al. Solution-processed, high-performance light-emitting diodes based on quantum dots. *Nature* **515**, 96–99 (2014).
10. Yang YX, Zheng Y, Cao WR et al. High-efficiency light-emitting devices based on quantum dots with tailored nanostructures. *Nat Photonics* **9**, 259–266 (2015).
11. Liu BC, Lin QZ, Sun SQ et al. Tailored large-particle quantum dots with high color purity and excellent electroluminescent efficiency. *Sci Bull* **70**, 905–913 (2025).
12. Liu BC, Bao JJ, He W et al. Highly orientated asymmetrically strained CdZnSeS/ZnSeS/ZnS/CdZnS quantum dots for efficient green light-emitting diodes. *Nano Energy* **140**, 110982 (2025).
13. Zhang WJ, Li B, Chang C et al. Stable and efficient pure blue quantum-dot LEDs enabled by inserting an anti-oxidation layer. *Nat Commun* **15**, 783 (2024).
14. Liu Y, Gao YY, Yang Q et al. Breaking the size limitation of directly-synthesized PbS quantum dot inks toward efficient short-wavelength infrared optoelectronic applications. *Angew Chem Int Ed* **62**, e202300396 (2023).
15. Wei KY, Zhou T, Jiang YZ et al. Perovskite heteroepitaxy for high-efficiency and stable pure-red LEDs. *Nature* **638**, 949–956 (2025).
16. Yuan S, Dai LJ, Sun YQ et al. Efficient blue electroluminescence from reduced-dimensional perovskites. *Nat Photonics* **18**, 425–431 (2024).
17. Liu YT, Sun YY, Yan XH et al. Realizing low voltage-driven bright and stable quantum dot light-emitting diodes through energy landscape flattening. *Light Sci Appl* **14**, 50 (2025).
18. Shen ZR, Jin CD, Lin QL et al. Core/shell ZnMgO@MgLiO electron transport layer for high-performance green quantum dot light-emitting diodes toward rec.2020 standard. *Adv Funct Mater* e23266 (2025).
19. Chen J, Li Y, Yin Z et al. Phase transition and rapid temperature response of lead-free perovskite Cs-Cu-I nanocrystals enabled by their size. *J Mater Chem C* **11**, 13030–13038 (2023).
20. Chen J, Li JY, Yin T et al. Rb-doped $Cs_3Cu_2I_5$ perovskite nanocrystals as paper-based scintillator film for high-resolution X-ray imaging. *Adv Funct Mater* **35**, 2506331 (2025).
21. Reifsnyder DC, Ye XC, Gordon TR et al. Three-dimensional self-assembly of chalcopyrite copper indium diselenide nanocrystals into oriented films. *ACS Nano* **7**, 4307–4315 (2013).
22. Chen B, Zheng WL, Chun FJ et al. Synthesis and hybridization of $CuInS_2$ nanocrystals for emerging applications. *Chem Soc Rev* **52**, 8374–8409 (2023).
23. Cheng CY, Yu BB, Huang F et al. Near-unity quantum yield ZnSeTe quantum dots enabled by controlling shell growth for efficient deep-blue light-emitting diodes. *Adv Funct Mater* **34**, 2313811 (2024).
24. Wu QQ, Cao F, Yu WK et al. Homogeneous ZnSeTeS quantum dots for efficient and stable pure-blue LEDs. *Nature* **639**, 633–638 (2025).
25. Won YH, Cho O, Kim T et al. Highly efficient and stable InP/ZnSe/ZnS quantum dot light-emitting diodes. *Nature* **575**, 634–638 (2019).
26. Bian YY, Yan XH, Chen F et al. Efficient green InP-based QD-LED by controlling electron injection and leakage. *Nature* **635**, 854–859 (2024).
27. Hu RR, He FK, Hou RX et al. The narrow synthetic window for highly homogenous InP quantum dots toward narrow red emission. *Inorg Chem* **63**, 3516–3524 (2024).
28. Li HY, Zhang WJ, Bian YY et al. ZnF_2-assisted synthesis of highly luminescent InP/ZnSe/ZnS quantum dots for efficient and stable electroluminescence. *Nano Lett* **22**, 4067–4073 (2022).
29. Kim S, Kim SH, Hwang HU et al. Revisiting the role of oxidation in

stable and high-performance lead-free perovskite-IGZO junction field-effect transistors. *Nat Commun* **16**, 7427 (2025).
30. Gao M, Yang HW, Shen HB et al. Bulk-like ZnSe quantum dots enabling efficient ultranarrow blue light-emitting diodes. *Nano Lett* **21**, 7252–7260 (2021).
31. Brus LE. Electron-electron and electron-hole interactions in small semiconductor crystallites: the size dependence of the lowest excited electronic state. *J Chem Phys* **80**, 4403–4409 (1984).
32. Wang FD, Buhro WE. Determination of the rod-wire transition length in colloidal indium phosphide quantum rods. *J Am Chem Soc* **129**, 14381–14387 (2007).
33. Tamang S, Lincheneau C, Hermans Y et al. Chemistry of InP nanocrystal syntheses. *Chem Mater* **28**, 2491–2506 (2016).
34. Heath JR. Covalency in semiconductor quantum dots. *Chem Soc Rev* **27**, 65–71 (1998).
35. Thomas A, Nair PV, George Thomas K. InP quantum dots: an environmentally friendly material with resonance energy transfer requisites. *J Phys Chem C* **118**, 3838–3845 (2014).
36. Kumar BG, Sadeghi S, Melikov R et al. Structural control of InP/ZnS core/shell quantum dots enables high-quality white LEDs. *Nanotechnology* **29**, 345605 (2018).
37. Micic OI, Curtis CJ, Jones KM et al. Synthesis and characterization of InP quantum dots. *J Phys Chem* **98**, 4966–4969 (1994).
38. Lim J, Bae WK, Lee D et al. InP@ZnSeS, core@composition gradient shell quantum dots with enhanced stability. *Chem Mater* **23**, 4459–4463 (2011).
39. Taylor DA, Teku JA, Cho S et al. Importance of surface functionalization and purification for narrow FWHM and bright green-emitting InP core-multishell quantum dots via a two-step growth process. *Chem Mater* **33**, 4399–4407 (2021).
40. Ramasamy P, Ko KJ, Kang JW et al. Two-step "seed-mediated" synthetic approach to colloidal indium phosphide quantum dots with high-purity photo- and electroluminescence. *Chem Mater* **30**, 3643–3647 (2018).
41. Yu P, Cao S, Shan YL et al. Highly efficient green InP-based quantum dot light-emitting diodes regulated by inner alloyed shell component. *Light Sci Appl* **11**, 162 (2022).
42. Wang SB, Yang WY, Li Y et al. Stable and efficient red InP-based QLEDs through surface passivation strategies of quantum dots. *Nano Lett* **24**, 15781–15787 (2024).
43. Yuan CW, Wan Q, Liao XR et al. Improved synthesis of blue InP/ZnS quantum dots via dynamic chloride ion capping. *Nano Lett* **25**, 10846–10852 (2025).
44. LaMer VK, Dinegar RH. Theory, production and mechanism of formation of monodispersed hydrosols. *J Am Chem Soc* **72**, 4847–4854 (1950).
45. Kwon SG, Hyeon T. Formation mechanisms of uniform nanocrystals via hot-injection and heat-up methods. *Small* **7**, 2685–2702 (2011).
46. Peng XG, Wickham J, Alivisatos AP. Kinetics of II-VI and III-V colloidal semiconductor nanocrystal growth: "focusing" of size distributions. *J Am Chem Soc* **120**, 5343–5344 (1998).
47. Sugimoto T. Preparation of monodispersed colloidal particles. *Adv Colloid Interface Sci* **28**, 65–108 (1987).
48. Ramasamy P, Kim N, Kang YS et al. Tunable, bright, and narrow-band luminescence from colloidal indium phosphide quantum dots. *Chem Mater* **29**, 6893–6899 (2017).
49. Chen B, Li DY, Wang F. InP quantum dots: synthesis and lighting applications. *Small* **16**, 2002454 (2020).
50. Abe S, Čapek RK, De Geyter B et al. Tuning the postfocused size of colloidal nanocrystals by the reaction rate: from theory to application. *ACS Nano* **6**, 42–53 (2012).
51. Battaglia D, Peng XG. Formation of high quality InP and InAs nanocrystals in a noncoordinating solvent. *Nano Lett* **2**, 1027–1030 (2002).
52. Lucey DW, MacRae DJ, Furis M et al. Monodispersed InP quantum dots prepared by colloidal chemistry in a noncoordinating solvent. *Chem Mater* **17**, 3754–3762 (2005).
53. Xu ZH, Li Y, Li JZ et al. Formation of size-tunable and nearly monodisperse InP nanocrystals: chemical reactions and controlled synthesis. *Chem Mater* **31**, 5331–5341 (2019).
54. van Embden J, Chesman ASR, Jasieniak JJ. The heat-up synthesis of colloidal nanocrystals. *Chem Mater* **27**, 2246–2285 (2015).
55. Cheng YB, Li Q, Chen MY et al. High-brightness green InP-based QLEDs enabled by *in-situ* passivating core surface with zinc myristate. *Mater Futures* **3**, 025201 (2024).
56. Xia YN, Gilroy KD, Peng HC et al. Seed-mediated growth of colloidal metal nanocrystals. *Angew Chem Int Ed* **56**, 60–95 (2017).
57. Franke D, Harris DK, Chen O et al. Continuous injection synthesis of indium arsenide quantum dots emissive in the short-wavelength infrared. *Nat Commun* **7**, 12749 (2016).
58. Kim T, Park S, Jeong S. Diffusion dynamics controlled colloidal synthesis of highly monodisperse InAs nanocrystals. *Nat Commun* **12**, 3013 (2021).
59. Achorn OB, Franke D, Bawendi MG. Seedless continuous injection synthesis of indium phosphide quantum dots as a route to large size and low size dispersity. *Chem Mater* **32**, 6532–6539 (2020).
60. Franke D, Harris DK, Xie LS et al. The unexpected influence of precursor conversion rate in the synthesis of III-V quantum dots. *Angew Chem Int Ed* **54**, 14299–14303 (2015).
61. Harris DK, Bawendi MG. Improved precursor chemistry for the synthesis of III-V quantum dots. *J Am Chem Soc* **134**, 20211–20213 (2012).
62. Allen PM, Walker BJ, Bawendi MG. Mechanistic insights into the formation of InP quantum dots. *Angew Chem Int Ed* **49**, 760–762 (2010).
63. Cui J, Beyler AP, Marshall LF et al. Direct probe of spectral inhomogeneity reveals synthetic tunability of single-nanocrystal spectral linewidths. *Nat Chem* **5**, 602–606 (2013).
64. Buffard A, Dreyfuss S, Nadal B et al. Mechanistic insight and optimization of InP nanocrystals synthesized with aminophosphines. *Chem Mater* **28**, 5925–5934 (2016).
65. Gary DC, Terban MW, Billinge SJL et al. Two-step nucleation and growth of InP quantum dots via magic-sized cluster intermediates. *Chem Mater* **27**, 1432–1441 (2015).
66. Owen JS, Chan EM, Liu HT et al. Precursor conversion kinetics and the nucleation of cadmium selenide nanocrystals. *J Am Chem Soc* **132**, 18206–18213 (2010).
67. Ali A, Jiang W, Choi Y et al. Control of the reaction kinetics of monodispersed InP/ZnSeS/ZnS-based quantum dots using organophosphorus compounds for electroluminescent devices. *J Phys Chem Lett* **14**, 1656–1662 (2023).
68. Jun KW, Khanna PK, Hong KB et al. Synthesis of InP nanocrystals from indium chloride and sodium phosphide by solution route. *Mater Chem Phys* **96**, 494–497 (2006).
69. Liu ZP, Kumbhar A, Xu D et al. Coreduction colloidal synthesis of III-V nanocrystals: the case of InP. *Angew Chem Int Ed* **47**, 3540–3542 (2008).
70. Li L, Protière M, Reiss P. Economic synthesis of high quality InP nanocrystals using calcium phosphide as the phosphorus precursor. *Chem Mater* **20**, 2621–2623 (2008).
71. Gao SM, Lu J, Chen N et al. Aqueous synthesis of III-V semiconductor GaP and InP exhibiting pronounced quantum confinement. *Chem Commun* **4** , 3064–3065 (2002).
72. Yan P, Xie Y, Wang WZ et al. A low-temperature route to InP nanocrystals. *J Mater Chem* **9**, 1831–1833 (1999).
73. Amberger E, Salazar GRW. Mixed organometallic compounds of group V I. Synthesis of tris(trimethyl-group-IV)stibines. *J Organomet Chem* **8**, 111–114 (1967).
74. Joung S, Yoon S, Han CS et al. Facile synthesis of uniform large-sized InP nanocrystal quantum dots using tris(tert-butyldimethylsilyl)phosphine. *Nanoscale Res Lett* **7**, 93 (2012).
75. Gary DC, Glassy BA, Cossairt BM. Investigation of indium phosphide quantum dot nucleation and growth utilizing triarylsilylphos-

phine precursors. *Chem Mater* **26**, 1734–1744 (2014).

76. Zhao HB, Hu HL, Zheng JP et al. One-pot synthesis of InP multishell quantum dots for narrow-bandwidth light-emitting devices. *ACS Appl Nano Mater* **6**, 3797–3802 (2023).
77. Van Avermaet H, Schiettecatte P, Hinz S et al. Full-spectrum InP-based quantum dots with near-unity photoluminescence quantum efficiency. *ACS Nano* **16**, 9701–9712 (2022).
78. Liu P, Lou YJ, Ding SH et al. Green InP/ZnSeS/ZnS core multishelled quantum dots synthesized with aminophosphine for effective display applications. *Adv Funct Mater* **31**, 2008453 (2021).
79. Jo JH, Jo DY, Choi SW et al. Highly bright, narrow emissivity of InP quantum dots synthesized by aminophosphine: effects of double shelling scheme and Ga treatment. *Adv Opt Mater* **9**, 2100427 (2021).
80. Jiang W, Choi Y, Chae H. Efficient green indium phosphide quantum dots with tris(dimethylamino)-phosphine phosphorus precursor for electroluminescent devices. *J Mater Sci Mater Electron* **32**, 4686–4694 (2021).
81. Matsumoto T, Maenosono S, Yamaguchi Y. Organometallic synthesis of InP quantum dots using tris(dimethylamino)phosphine as a phosphorus source. *Chem Lett* **33**, 1492–1493 (2004).
82. Ryu E, Kim S, Jang E et al. Step-wise synthesis of InP/ZnS core-shell quantum dots and the role of zinc acetate. *Chem Mater* **21**, 573–575 (2009).
83. Tessier MD, Dupont D, De Nolf K et al. Economic and size-tunable synthesis of InP/ZnE (E = S, Se) colloidal quantum dots. *Chem Mater* **27**, 4893–4898 (2015).
84. Song WS, Lee HS, Lee JC et al. Amine-derived synthetic approach to color-tunable InP/ZnS quantum dots with high fluorescent qualities. *J Nanopart Res* **15**, 1750 (2013).
85. Tessier MD, De Nolf K, Dupont D et al. Aminophosphines: a double role in the synthesis of colloidal indium phosphide quantum dots. *J Am Chem Soc* **138**, 5923–5929 (2016).
86. Long R, Chen XP, Zhang XH et al. Carboxylic-free synthesis of InP quantum dots for highly efficient and bright electroluminescent device. *Adv Opt Mater* **11**, 2202594 (2023).
87. Xie RG, Peng XG. Synthetic scheme for high-quality InAs nanocrystals based on self-focusing and one-pot synthesis of InAs-based core-shell nanocrystals. *Angew Chem Int Ed* **47**, 7677–7680 (2008).
88. Xie RG, Li Z, Peng XG. Nucleation kinetics vs chemical kinetics in the initial formation of semiconductor nanocrystals. *J Am Chem Soc* **131**, 15457–15466 (2009).
89. Harrell SM, McBride JR, Rosenthal SJ. Synthesis of ultrasmall and magic-sized CdSe nanocrystals. *Chem Mater* **25**, 1199–1210 (2013).
90. Cossairt BM. Shining light on indium phosphide quantum dots: understanding the interplay among precursor conversion, nucleation, and growth. *Chem Mater* **28**, 7181–7189 (2016).
91. Ripberger HH, Sandeno SF, Eagle FW et al. Structure and reactivity of II-VI and III-V magic-sized clusters: understanding and expanding the scope of accessible form and function. *Acc Mater Res* **5**, 726–738 (2024).
92. Gary DC, Flowers SE, Kaminsky W et al. Single-crystal and electronic structure of a 1.3 nm indium phosphide nanocluster. *J Am Chem Soc* **138**, 1510–1513 (2016).
93. Friedfeld MR, Stein JL, Cossairt BM. Main-group-semiconductor cluster molecules as synthetic intermediates to nanostructures. *Inorg Chem* **56**, 8689–8697 (2017).
94. Brown RP, Gallagher MJ, Fairbrother DH et al. Synthesis and degradation of cadmium-free InP and InPZn/ZnS quantum dots in solution. *Langmuir* **34**, 13924–13934 (2018).
95. Kwon Y, Oh J, Lee E et al. Evolution from unimolecular to colloidal-quantum-dot-like character in chlorine or zinc incorporated InP magic size clusters. *Nat Commun* **11**, 3127 (2020).
96. Kwon Y, Kim S. Indium phosphide magic-sized clusters: chemistry and applications. *NPG Asia Mater* **13**, 37 (2021).
97. Jo JH, Jo DY, Lee SH et al. InP-based quantum dots having an InP core, composition-gradient ZnSeS inner shell, and ZnS outer shell with sharp, bright emissivity, and blue absorptivity for display devices. *ACS Appl Nano Mater* **3**, 1972–1980 (2020).
98. Thuy UTD, Reiss P, Liem NQ. Luminescence properties of In(Zn)P alloy core/ZnS shell quantum dots. *Appl Phys Lett* **97**, 193104 (2010).
99. Alexander E, Kick M, McIsaac AR et al. Understanding trap states in InP and GaP quantum dots through density functional theory. *Nano Lett* **24**, 7227–7235 (2024).
100. Yuan CW, Wan Q, Liao XR et al. Dual-mode strain relief via zinc acetate enables high-efficiency InP quantum dot light-emitting diodes. *Angew Chem Int Ed* **64**, e202509765 (2025).
101. Stein JL, Mader EA, Cossairt BM. Luminescent InP quantum dots with tunable emission by post-synthetic modification with lewis acids. *J Phys Chem Lett* **7**, 1315–1320 (2016).
102. Laufersky G, Bradley S, Frécaut E et al. Unraveling aminophosphine redox mechanisms for glovebox-free InP quantum dot syntheses. *Nanoscale* **10**, 8752–8762 (2018).
103. Koh S, Eom T, Kim WD et al. Zinc-phosphorus complex working as an atomic valve for colloidal growth of monodisperse indium phosphide quantum dots. *Chem Mater* **29**, 6346–6355 (2017).
104. Janke EM, Williams NE, She CX et al. Origin of broad emission spectra in InP quantum dots: contributions from structural and electronic disorder. *J Am Chem Soc* **140**, 15791–15803 (2018).
105. Kirkwood N, De Backer A, Altantzis T et al. Locating and controlling the Zn content in In(Zn)P quantum dots. *Chem Mater* **32**, 557–565 (2020).
106. Kim TG, Zherebetskyy D, Bekenstein Y et al. Trap passivation in indium-based quantum dots through surface fluorination: mechanism and applications. *ACS Nano* **12**, 11529–11540 (2018).
107. Hartley CL, Kessler ML, Dempsey JL. Molecular-level insight into semiconductor nanocrystal surfaces. *J Am Chem Soc* **143**, 1251–1266 (2021).
108. Vokhmintcev KV, Samokhvalov PS, Nabiev I. Charge transfer and separation in photoexcited quantum dot-based systems. *Nano Today* **11**, 189–211 (2016).
109. Houtepen AJ, Hens Z, Owen JS et al. On the origin of surface traps in colloidal II-VI semiconductor nanocrystals. *Chem Mater* **29**, 752–761 (2017).
110. Yang WX, Yang YW, Kaledin AL et al. Surface passivation extends single and biexciton lifetimes of InP quantum dots. *Chem Sci* **11**, 5779–5789 (2020).
111. Reiss P, Carrière M, Lincheneau C et al. Synthesis of semiconductor nanocrystals, focusing on nontoxic and earth-abundant materials. *Chem Rev* **116**, 10731–10819 (2016).
112. Virieux H, Le Troedec M, Cros-Gagneux A et al. InP/ZnS nanocrystals: coupling NMR and XPS for fine surface and interface description. *J Am Chem Soc* **134**, 19701–19708 (2012).
113. Cros-Gagneux A, Delpech F, Nayral C et al. Surface chemistry of InP quantum dots: a comprehensive study. *J Am Chem Soc* **132**, 18147–18157 (2010).
114. Stein JL, Holden WM, Venkatesh A et al. Probing surface defects of InP quantum dots using phosphorus Kα and Kβ X-ray emission spectroscopy. *Chem Mater* **30**, 6377–6388 (2018).
115. Choi Y, Hahm D, Bae WK et al. Heteroepitaxial chemistry of zinc chalcogenides on InP nanocrystals for defect-free interfaces with atomic uniformity. *Nat Commun* **14**, 43 (2023).
116. Cervilla A, Pérez-Pla F, Llopis E et al. Unusual oxidation of phosphines employing water as the oxygen atom source and tris(benzene-1, 2-dithiolate)molybdenum(VI) as the oxidant. A functional molybdenum hydroxylase analogue system. *Inorg Chem* **45**, 7357–7366 (2006).
117. Vikram A, Zahid A, Bhargava SS et al. Unraveling the origin of interfacial oxidation of InP-based quantum dots: implications for bioimaging and optoelectronics. *ACS Appl Nano Mater* **3**,

12325–12333 (2020).

118. Vikram A, Zahid A, Bhargava SS et al. Mechanistic insights into size-focused growth of indium phosphide nanocrystals in the presence of trace water. *Chem Mater* **32**, 3577–3584 (2020).
119. Tessier MD, Baquero EA, Dupont D et al. Interfacial oxidation and photoluminescence of InP-based core/shell quantum dots. *Chem Mater* **30**, 6877–6883 (2018).
120. Mićić OI, Sprague J, Lu ZH et al. Highly efficient band-edge emission from InP quantum dots. *Appl Phys Lett* **68**, 3150–3152 (1996).
121. Kim Y, Chang JH, Choi H et al. III-V colloidal nanocrystals: control of covalent surfaces. *Chem Sci* **11**, 913–922 (2020).
122. Adam S, Talapin DV, Borchert H et al. The effect of nanocrystal surface structure on the luminescence properties: photoemission study of HF-etched InP nanocrystals. *J Chem Phys* **123**, 084706 (2005).
123. Hughes KE, Stein JL, Friedfeld MR et al. Effects of surface chemistry on the photophysics of colloidal InP nanocrystals. *ACS Nano* **13**, 14198–14207 (2019).
124. Pu YC, Fan HC, Chang JC et al. Effects of interfacial oxidative layer removal on charge carrier recombination dynamics in InP/ZnSe$_x$S$_{1\text{-}x}$ core/shell quantum dots. *J Phys Chem Lett* **12**, 7194–7200 (2021).
125. Ubbink RF, Almeida G, Iziyi H et al. A water-free in situ HF treatment for ultrabright InP quantum dots. *Chem Mater* **34**, 10093–10103 (2022).
126. Siramdas R, McLaurin EJ. InP nanocrystals with color-tunable luminescence by microwave-assisted ionic-liquid etching. *Chem Mater* **29**, 2101–2109 (2017).
127. Lovingood DD, Strouse GF. Microwave induced in-situ active ion etching of growing InP nanocrystals. *Nano Lett* **8**, 3394–3397 (2008).
128. Chandrasiri HB, Kim EB, Snee PT. Sterically encumbered tris(trialkylsilyl) phosphine precursors for quantum dot synthesis. *Inorg Chem* **59**, 15928–15935 (2020).
129. Valleix R, Zhang W, Jordan AJ et al. Metal fluorides passivate II-VI and III-V quantum dots. *Nano Lett* **24**, 5722–5728 (2024).
130. Sun Z, Hou QG, Kong JH et al. Surface passivation toward multiple inherent dangling bonds in indium phosphide quantum dots. *Inorg Chem* **63**, 6396–6407 (2024).
131. Stam M, Almeida G, Ubbink RF et al. Near-unity photoluminescence quantum yield of core-only InP quantum dots *via* a simple postsynthetic InF$_3$ treatment. *ACS Nano* **18**, 14685–14695 (2024).
132. Calvin JJ, Swabeck JK, Sedlak AB et al. Thermodynamic investigation of increased luminescence in indium phosphide quantum dots by treatment with metal halide salts. *J Am Chem Soc* **142**, 18897–18906 (2020).
133. Kirkwood N, Monchen JOV, Crisp RW et al. Finding and fixing traps in II-VI and III-V colloidal quantum dots: the importance of Z-type ligand passivation. *J Am Chem Soc* **140**, 15712–15723 (2018).
134. Xu S, Ziegler J, Nann T. Rapid synthesis of highly luminescent InP and InP/ZnS nanocrystals. *J Mater Chem* **18**, 2653–2656 (2008).
135. Li L, Reiss P. One-pot synthesis of highly luminescent InP/ZnS nanocrystals without precursor injection. *J Am Chem Soc* **130**, 11588–11589 (2008).
136. Park J, Kim S, Kim S et al. Fabrication of highly luminescent InP/Cd and InP/CdS quantum dots. *J Lumin* **130**, 1825–1828 (2010).
137. Song KZ, He XH, Chen ZY et al. Bright InP quantum dots by Ga-doping for red emitters. *Nano Res* **17**, 6721–6733 (2024).
138. Gwak N, Shin S, Yoo H et al. Highly luminescent shell-less indium phosphide quantum dots enabled by atomistically tailored surface states. *Adv Mater* **36**, 2404480 (2024).
139. Chen PR, Hoang MS, Lai KY et al. Bifunctional metal oleate as an alternative method to remove surface oxide and passivate surface defects of aminophosphine-based InP quantum dots. *Nanomaterials* **12**, 573 (2022).
140. Chen HS, Chen CY, Wu YC. High-performance giant InP quantum dots with stress‐released morphological ZnSe-ZnSeS-ZnS shell. *Adv Mater* **37**, 2407026 (2025).
141. Kim T, Won YH, Jang E et al. Negative trion auger recombination in highly luminescent InP/ZnSe/ZnS quantum dots. *Nano Lett* **21**, 2111–2116 (2021).
142. Sung YM, Kim TG, Yun DJ et al. Increasing the energy gap between band-edge and trap states slows down picosecond carrier trapping in highly luminescent InP/ZnSe/ZnS quantum dots. *Small* **17**, 2102792 (2021).
143. Park J, Won YH, Han Y et al. Tuning hot carrier dynamics of InP/ZnSe/ZnS quantum dots by shell morphology control. *Small* **18**, 2105492 (2022).
144. Lee Y, Jo DY, Kim T et al. Effectual interface and defect engineering for auger recombination suppression in bright InP/ZnSeS/ZnS quantum dots. *ACS Appl Mater Interfaces* **14**, 12479–12487 (2022).
145. Hou QG, Huang YX, Kong JH et al. Shell composition-mediated band alignment and defect engineering in indium phosphide-based core/shell quantum dots. *J Phys Chem C* **129**, 6890–6900 (2025).
146. Vurgaftman I, Meyer JR, Ram-Mohan LR. Band parameters for III-V compound semiconductors and their alloys. *J Appl Phys* **89**, 5815–5875 (2001).
147. Hahm D, Chang JH, Jeong BG et al. Design principle for bright, robust, and color-pure InP/ZnSe$_x$S$_{1-x}$/ZnS heterostructures. *Chem Mater* **31**, 3476–3484 (2019).
148. Jang E, Kim Y, Won YH et al. Environmentally friendly InP-based quantum dots for efficient wide color gamut displays. *ACS Energy Lett* **5**, 1316–1327 (2020).
149. Yang SJ, Oh JH, Kim S et al. Realization of InP/ZnS quantum dots for green, amber and red down-converted LEDs and their color-tunable, four-package white LEDs. *J Mater Chem C* **3**, 3582–3591 (2015).
150. Cui ZJ, Mei SL, Wen ZQ et al. Synergistic effect of halogen ions and shelling temperature on anion exchange induced interfacial restructuring for highly efficient blue emissive InP/ZnS quantum dots. *Small* **18**, 2108120 (2022).
151. Reiss P, Protière M, Li L. Core/shell semiconductor nanocrystals. *Small* **5**, 154–168 (2009).
152. Lange H, Kelley DF. Spectroscopic effects of lattice strain in InP/ZnSe and InP/ZnS nanocrystals. *J Phys Chem C* **124**, 22839–22844 (2020).
153. Gong K, Kelley DF. A predictive model of shell morphology in CdSe/CdS core/shell quantum dots. *J Chem Phys* **141**, 194704 (2014).
154. Li HY, Bian YY, Zhang WJ et al. High performance InP-based quantum dot light-emitting diodes via the suppression of field-enhanced electron delocalization. *Adv Funct Mater* **32**, 2204529 (2022).
155. Cooper JK, Gul S, Lindley SA et al. Tunable photoluminescent core/shell Cu$^+$ -doped ZnSe/ZnS quantum dots codoped with Al^{3+}, Ga^{3+}, or In^{3+}. *ACS Appl Mater Interfaces* **7**, 10055–10066 (2015).
156. Jana S, Srivastava BB, Acharya S et al. Prevention of photooxidation in blue-green emitting Cu doped ZnSe nanocrystals. *Chem Commun* **46**, 2853–2855 (2010).
157. Jia J, Xue P, Hu XY et al. Electron-transfer cascade from CdSe@ZnSe core-shell quantum dot accelerates photoelectrochemical H$_2$ evolution on TiO$_2$ nanotube arrays. *J Catal* **375**, 81–94 (2019).
158. Zhang JK, Li JZ, Ye ZK et al. Hot-electron-induced photochemical properties of CdSe/ZnSe core/shell quantum dots under an

ambient environment. *J Am Chem Soc* **145**, 13938–13949 (2023).

159. Respekta D, Schiettecatte P, Giordano L et al. Energy-level structure and band alignment in InP/ZnSe core/shell quantum dots. *ACS Nano* **19**, 19831–19840 (2025).
160. Kim Y, Ham S, Jang H et al. Bright and uniform green light emitting InP/ZnSe/ZnS quantum dots for wide color gamut displays. *ACS Appl Nano Mater* **2**, 1496–1504 (2019).
161. Sun ZJ, Wu QQ, Wang S et al. Suppressing the cation exchange at the core/shell interface of InP quantum dots by a selenium shielding layer enables efficient green light-emitting diodes. *ACS Appl Mater Interfaces* **14**, 15401–15406 (2022).
162. Yoo D, Choi MJ. Asymmetric metal-carboxylate complexes for synthesis of InGaP alloyed quantum dots with blue emission. *ACS Nano* **18**, 16051–16058 (2024).
163. Srivastava V, Kamysbayev V, Hong L et al. Colloidal chemistry in molten salts: synthesis of luminescent $\mathrm{In}_{1\text{-}x}\mathrm{Ga}_x\mathrm{P}$ and $\mathrm{In}_{1\text{-}x}\mathrm{Ga}_x\mathrm{As}$ quantum dots. *J Am Chem Soc* **140**, 12144–12151 (2018).
164. Zhang H, Hu N, Zeng ZP et al. High-efficiency green InP quantum dot-based electroluminescent device comprising thick-shell quantum dots. *Adv Opt Mater* **7**, 1801602 (2019).
165. Zhang H, Ma XY, Lin QL et al. High-brightness blue InP quantum dot-based electroluminescent devices: the role of shell thickness. *J Phys Chem Lett* **11**, 960–967 (2020).
166. Kim S, Kim T, Kang M et al. Highly luminescent InP/GaP/ZnS nanocrystals and their application to white light-emitting diodes. *J Am Chem Soc* **134**, 3804–3809 (2012).
167. Park JP, Lee JJ, Kim SW. Highly luminescent InP/GaP/ZnS QDs emitting in the entire color range via a heating up process. *Sci Rep* **6**, 30094 (2016).
168. Hudson MH, Gupta A, Srivastava V et al. Synthesis of $\mathrm{In}_{1\text{-}x}\mathrm{Ga}_x\mathrm{P}$ quantum dots in Lewis basic molten salts: the effects of surface chemistry, reaction conditions, and molten salt composition. *J Phys Chem C* **126**, 1564–1580 (2022).
169. Pietra F, Kirkwood N, De Trizio L et al. Ga for Zn cation exchange allows for highly luminescent and photostable InZnP-based quantum dots. *Chem Mater* **29**, 5192–5199 (2017).
170. Kim M, Shin WH, Bang J. Highly luminescent and stable green-emitting In(Zn,Ga)P/ZnSeS/ZnS small-core/thick-multishell quantum dots. *J Lumin* **205**, 555–559 (2019).
171. Kim KH, Jo JH, Jo DY et al. Cation-exchange-derived InGaP alloy quantum dots toward blue emissivity. *Chem Mater* **32**, 3537–3544 (2020).
172. Wegner KD, Pouget S, Ling WL et al. Gallium-a versatile element for tuning the photoluminescence properties of InP quantum dots. *Chem Commun* **55**, 1663–1666 (2019).
173. Kim S, Lee K, Kim S et al. Origin of photoluminescence from colloidal gallium phosphide nanocrystals synthesized via a hot-injection method. *RSC Adv* **5**, 2466–2469 (2015).
174. Bae WK, Char K, Hur H et al. Single-step synthesis of quantum dots with chemical composition gradients. *Chem Mater* **20**, 531–539 (2008).
175. Bae WK, Nam MK, Char K et al. Gram-scale one-pot synthesis of highly luminescent blue emitting $\mathrm{Cd}_{1\text{-}x}\mathrm{Zn}_x\mathrm{S}$/ZnS nanocrystals. *Chem Mater* **20**, 5307–5313 (2008).
176. Lee SH, Kim Y, Jang H et al. The effects of discrete and gradient mid-shell structures on the photoluminescence of single InP quantum dots. *Nanoscale* **11**, 23251–23258 (2019).
177. Kim HS, Kim Y, Cho S et al. Off-state-free and stable InP/ZnSe/ZnS quantum dots enabled by effectively suppressing the leakage of charge carriers. *J Phys Chem C* **128**, 3343–3350 (2024).
178. Zhang WD, Ding SH, Zhuang WD et al. InP/ZnS/ZnS core/shell blue quantum dots for efficient light‐emitting diodes. *Adv Funct Mater* **30**, 2005303 (2020).
179. Hassinen A, Moreels I, De Nolf K et al. Short-chain alcohols strip X-type ligands and quench the luminescence of PbSe and CdSe quantum dots, acetonitrile does not. *J Am Chem Soc* **134**, 20705–20712 (2012).
180. Zhang WD, Zhuang WD, Liu RH et al. Double-shelled InP/ZnMnS/ZnS quantum dots for light-emitting devices. *ACS Omega* **4**, 18961–18968 (2019).
181. Okamoto A, Bai H, Toda S et al. Controlling thickness of ZnSe intermediate shell narrows FWHM of green-emitting spectra of InP/ZnSe/ZnS multi-shell quantum dots. *ChemNanoMat* **9**, e202200534 (2023).
182. Ji BT, Koley S, Slobodkin I et al. ZnSe/ZnS core/shell quantum dots with superior optical properties through thermodynamic shell growth. *Nano Lett* **20**, 2387–2395 (2020).
183. Zhao JX, Chen B, Wang F. Shedding light on the role of misfit strain in controlling core-shell nanocrystals. *Adv Mater* **32**, 2004142 (2020).
184. Zhdanov VP. Relaxation of a dislocation in a nanocrystallite. *Phys Lett A* **383**, 744–747 (2019).
185. Li Y, Hou XQ, Dai XL et al. Stoichiometry-controlled InP-based quantum dots: synthesis, photoluminescence, and electroluminescence. *J Am Chem Soc* **141**, 6448–6452 (2019).
186. Wu QQ, Cao F, Wang S et al. Quasi-shell-growth strategy achieves stable and efficient green InP quantum dot light-emitting diodes. *Adv Sci* **9**, 2200959 (2022).
187. Cao F, Wang S, Wang FJ et al. A layer-by-layer growth strategy for large-size InP/ZnSe/ZnS core-shell quantum dots enabling high-efficiency light-emitting diodes. *Chem Mater* **30**, 8002–8007 (2018).
188. Liu LP, Zhuang ZB, Xie T et al. Shape control of CdSe nanocrystals with zinc blende structure. *J Am Chem Soc* **131**, 16423–16429 (2009).
189. Ji BT, Panfil YE, Waiskopf N et al. Strain-controlled shell morphology on quantum rods. *Nat Commun* **10**, 2 (2019).
190. Chao WC, Chiang TH, Liu YC et al. High efficiency green InP quantum dot light-emitting diodes by balancing electron and hole mobility. *Commun Mater* **2**, 96 (2021).
191. Zhao TS, Zhao QH, Lee J et al. Engineering the surface chemistry of colloidal InP quantum dots for charge transport. *Chem Mater* **34**, 8306–8315 (2022).
192. Calvin JJ, O'Brien EA, Sedlak AB et al. Thermodynamics of composition dependent ligand exchange on the surfaces of colloidal indium phosphide quantum dots. *ACS Nano* **15**, 1407–1420 (2021).
193. Park SA, Jung WH, Yoo JY et al. Electrical resonant effects of ligands on the luminescent properties of InP/ZnSeS/ZnS quantum dots and devices configured therefrom. *Org Electron* **87**, 105955 (2020).
194. Park J, Kim T, Kim D. Charge injection and energy transfer of surface-engineered InP/ZnSe/ZnS quantum dots. *Nanomaterials* **13**, 1159 (2023).
195. Pietryga JM, Park YS, Lim J et al. Spectroscopic and device aspects of nanocrystal quantum dots. *Chem Rev* **116**, 10513–10622 (2016).
196. Yang ZW, Gao MY, Wu WJ et al. Recent advances in quantum dot-based light-emitting devices: challenges and possible solutions. *Mater Today* **24**, 69–93 (2019).
197. Nunes FS, Da Silva Bonifácio L, Araki K et al. Interaction of 2-and 4-mercaptopyridine with pentacyanoferrates and gold nanoparticles. *Inorg Chem* **45**, 94–101 (2006).
198. Kim J, Kim Y, Park K et al. Ligand effect in 1-octanethiol passivation of InP/ZnSe/ZnS quantum dots-evidence of incomplete surface passivation during synthesis. *Small* **18**, 2203093 (2022).
199. Jiang W, Chae H. Efficiency enhancement of tris(dimethylamino)-phosphine-based red indium phosphide quantum-dot light-emitting

diodes via chlorine-doped ZnMgO electron transport layers. *J Phys Chem C* **124**, 25221–25228 (2020).

200. Fukuda T, Sasaki H. Improvement in luminance of light-emitting diode using InP/ZnS quantum dot with 1-dodecanethiol ligand. *Jpn J Appl Phys* **57**, 03EH06 (2018).
201. Zeng SJ, Li ZB, Tan WJ et al. Ultrafast electron transfer dynamics affected by ligand chain length in InP/ZnS core/shell quantum dots. *J Phys Chem C* **126**, 9091–9098 (2022).
202. Choi HS, Janietz S, Roddatis V et al. Enhanced electroluminescence via a nanohybrid material consisting of aromatic ligand-modified InP quantum dots and an electron-blocking polymer as the single active layer in quantum dot-LEDs. *Nanomaterials* **12**, 408 (2022).
203. Boles MA, Ling D, Hyeon T et al. Erratum: the surface science of nanocrystals. *Nat Mater* **15**, 364 (2016).
204. Heuer-Jungemann A, Feliu N, Bakaimi I et al. The role of ligands in the chemical synthesis and applications of inorganic nanoparticles. *Chem Rev* **119**, 4819–4880 (2019).
205. Kim T, Kim KH, Kim S et al. Efficient and stable blue quantum dot light-emitting diode. *Nature* **586**, 385–389 (2020).
206. García De Arquer FP, Talapin DV, Klimov VI et al. Semiconductor quantum dots: technological progress and future challenges. *Science* **373**, eaaz8541 (2021).
207. McHugh KJ, Jing LH, Behrens AM et al. Biocompatible semiconductor quantum dots as cancer imaging agents. *Adv Mater* **30**, 1706356 (2018).
208. Ding CP, Huang YJ, Shen ZY et al. Synthesis and bioapplications of Ag_2S quantum dots with near-infrared fluorescence. *Adv Mater* **33**, 2007768 (2021).
209. Deng YH, Pang C, Kheradmand E et al. Short-wave infrared colloidal QD photodetector with nanosecond response times enabled by ultrathin absorber layers. *Adv Mater* **36**, 2402002 (2024).
210. Wang YJ, Peng LC, Schreier J et al. Silver telluride colloidal quantum dot infrared photodetectors and image sensors. *Nat Photonics* **18**, 236–242 (2024).
211. Chen S, Xu H. Electroluminescent materials toward near ultraviolet region. *Chem Soc Rev* **50**, 8639–8668 (2021).
212. Lan XZ, Chen ML, Hudson MH et al. Quantum dot solids showing state-resolved band-like transport. *Nat Mater* **19**, 323–329 (2020).
213. Meng TT, Zheng YT, Zhao DL et al. Ultrahigh-resolution quantum-dot light-emitting diodes. *Nat Photonics* **16**, 297–303 (2022).
214. Zhang H, Su Q, Chen SM. Recent progress in the device architecture of white quantum-dot light-emitting diodes. *J Inf Disp* **20**, 169–180 (2019).
215. Wang YC, Chen ZJ, Wang T et al. Efficient structure for InP/ZnS-based electroluminescence device by embedding the emitters in the electron-dominating interface. *J Phys Chem Lett* **11**, 1835–1839 (2020).
216. Lampande R, Shin DH, Naik MN et al. 51-2: High efficiency and long lifetime InP-based red quantum dot light-emitting diodes. *SID Symp Dig Tech Pap* **51**, 750–753 (2020).
217. Chen F, Lv P, Li X et al. Highly-efficient and all-solution-processed red-emitting InP/ZnS-based quantum-dot light-emitting diodes enabled by compositional engineering of electron transport layers. *J Mater Chem C* **7**, 7636–7642 (2019).
218. Pallares RM, Su XD, Lim SH et al. Fine-tuning of gold nanorod dimensions and plasmonic properties using the Hofmeister effects. *J Mater Chem C* **4**, 53–61 (2016).
219. Mei GD, Tan YZ, Sun JY et al. Light extraction employing optical tunneling in blue InP quantum dot light-emitting diodes. *Appl Phys Lett* **120**, 091101 (2022).
220. Wang W, Zhang SZ, Huo ST et al. Controllable nucleation and growth of blue InP quantum dots enable efficient and bright light-emitting diodes. *Adv Opt Mater* **13**, 2500294 (2025).
221. Zhang TQ, Liu P, Zhao FQ et al. Electric dipole modulation for boosting carrier recombination in green InP QLEDs under strong electron injection. *Nanoscale Adv* **5**, 385–392 (2023).
222. Mude NN, Khan Y, Thuy TT et al. Stable ZnS electron transport layer for high-performance inverted cadmium-free quantum dot light-emitting diodes. *ACS Appl Mater Interfaces* **14**, 55925–55932 (2022).
223. Chen MY, Li Q, Bian YY et al. High-efficiency and stable green InP-QLED enabled by lowering electron injection barrier. *Adv Opt Mater* **13**, 2402555 (2025).
224. Deng YZ, Peng F, Lu Y et al. Solution-processed green and blue quantum-dot light-emitting diodes with eliminated charge leakage. *Nat Photonics* **16**, 505–511 (2022).
225. Chen HT, Ding K, Fan LW et al. All-solution-processed quantum dot light emitting diodes based on double hole transport layers by hot spin-coating with highly efficient and low turn-on voltage. *ACS Appl Mater Interfaces* **10**, 29076–29082 (2018).
226. Xu HY, Song JJ, Zhou PH et al. Dipole-dipole-interaction-assisted self-assembly of quantum dots for highly efficient light-emitting diodes. *Nat Photonics* **18**, 186–191 (2024).
227. Wang XZ, Gao Y, Liu XN et al. Strong high-energy exciton electroluminescence from the light holes of polytypic quantum dots. *Nat Commun* **15**, 6334 (2024).
228. Shin DH, Lampande R, Kim SJ et al. Understanding the origin of degradation of InP-quantum dot light-emitting diodes. *Adv Elect Mater* **8**, 2200256 (2022).
229. Ryu H, Shin D, Yoon B et al. Direct evidence of excessive charge-carrier-induced degradation in InP quantum-dot light-emitting diodes. *ACS Appl Mater Interfaces* **17**, 1408–1419 (2025).
230. Su Q, Zhang H, Chen SM. Identification of excess charge carriers in InP-based quantum-dot light-emitting diodes. *Appl Phys Lett* **117**, 053502 (2020).
231. Ali A, Hussain I, Seo H et al. Exploring the recent progress in InP quantum dots and QLEDs: advances in synthesis, architecture, and applications. *Laser Photonics Rev* **19**, e01169 (2025).
232. Bozyigit D, Wood V. Challenges and solutions for high-efficiency quantum dot-based LEDs. *MRS Bull* **38**, 731–736 (2013).
233. Shirasaki Y, Supran GJ, Bawendi MG et al. Emergence of colloidal quantum-dot light-emitting technologies. *Nat Photonics* **7**, 13–23 (2013).
234. Liu BC, Guo Y, Su Q et al. Cadmium-doped zinc sulfide shell as a hole injection springboard for red, green, and blue quantum dot light‐emitting diodes. *Adv Sci* **9**, 2104488 (2022).
235. Gao Y, Li B, Liu XN et al. Minimizing heat generation in quantum dot light-emitting diodes by increasing quasi-Fermi-level splitting. *Nat Nanotechnol* **18**, 1168–1174 (2023).
236. Nam S, Oh N, Zhai Y et al. High efficiency and optical anisotropy in double-heterojunction nanorod light-emitting diodes. *ACS Nano* **9**, 878–885 (2015).
237. Gao YN, Weidman MC, Tisdale WA. CdSe nanoplatelet films with controlled orientation of their transition dipole moment. *Nano Lett* **17**, 3837–3843 (2017).
238. Wang YH, Pu CD, Lei HR et al. CdSe@CdS dot@platelet nanocrystals: controlled epitaxy, monoexponential decay of two-dimensional exciton, and nonblinking photoluminescence of single nanocrystal. *J Am Chem Soc* **141**, 17617–17628 (2019).
239. Nann T, Schneider J. Origin of permanent electric dipole moments in wurtzite nanocrystals. *Chem Phys Lett* **384**, 150–152 (2004).
240. Wu YC, Lee HY, Chen HS. Pre-shell protection suppresses facet-selective core digestion in InP quantum dots for high-yield and uniform core/shell structures. *ACS Appl Mater Interfaces* **17**, 61509–61518 (2025).
241. Mi GH, Yao YS, Yang Q et al. Synergistic surface under-coordinated sites and ligand engineering of colloidal quantum dots for

high-efficiency bifunctional photoelectrochemical devices. *Adv Funct Mater* e20672 (2025).
242. Jo JH, Kim JH, Lee KH et al. High-efficiency red electroluminescent device based on multishelled InP quantum dots. *Opt Lett* **41**, 3984–3987 (2016).
243. Lee CY, Naik Mude N, Lampande R et al. Efficient cadmium-free inverted red quantum dot light-emitting diodes. *ACS Appl Mater Interfaces* **11**, 36917–36924 (2019).
244. Kim H, Lee W, Moon H et al. Interlayer doping with p-type dopant for charge balance in indium phosphide (InP)-based quantum dot light-emitting diodes. *Opt. Express* **27**, A1287–A1296 (2019).
245. Yeom JE, Shin DH, Lampande R et al. Good charge balanced inverted red InP/ZnSe/ZnS-quantum dot light-emitting diode with new high mobility and deep HOMO level hole transport layer. *ACS Energy Lett* **5**, 3868–3875 (2020).
246. Kim BH, Acharya KP, Titov A et al. 23.3: Charge injection control of cadmium-free quantum dot light-emitting diodes. *SID Symp Dig Tech Pap* **52**, 147–150 (2021).
247. Yu P, Shan YL, Cao S et al. Inorganic solid phosphorus precursor of sodium phosphaethynolate for synthesis of highly luminescent InP-based quantum dots. *ACS Energy Lett* **6**, 2697–2703 (2021).
248. Han MG, Lee Y, Kwon HI et al. InP-based quantum dot light-emitting diode with a blended emissive layer. *ACS Energy Lett* **6**, 1577–1585 (2021).
249. Li QY, Cao S, Yu P et al. Boosting electroluminescence performance of all solution processed InP based quantum dot light emitting diodes using bilayered inorganic hole injection layers. *Photonics Res* **10**, 2133–2139 (2022).
250. Yoon SY, Lee YJ, Yang H et al. Performance enhancement of InP quantum dot light-emitting diodes via a surface-functionalized ZnMgO electron transport layer. *ACS Energy Lett* **7**, 2247–2255 (2022).
251. Yoo JY, Jung WH, Kim HJ et al. Efficient InP/ZnSe/ZnS quantum dot shelling and the effect of a bi-layered organic-inorganic electron-transport layer on the performance of quantum dot light-emitting diode devices. *Org Electron* **108**, 106569 (2022).
252. Choi SW, Kim HM, Yoon SY et al. Aminophosphine-derived, high-quality red-emissive InP quantum dots by the use of an unconventional in halide. *J Mater Chem C* **10**, 2213–2222 (2022).
253. Lee S, Park SM, Jung ED et al. Dipole engineering through the orientation of interface molecules for efficient InP quantum dot light-emitting diodes. *J Am Chem Soc* **144**, 20923–20930 (2022).
254. Du WX, Cheng CY, Tian JJ. Efficient solution-processed InP quantum-dots light-emitting diodes enabled by suppressing hole injection loss. *Nano Res* **16**, 7511–7517 (2023).
255. Mude NN, Kim SJ, Lampande R et al. An efficient organic and inorganic hybrid interlayer for high performance inverted red cadmium-free quantum dot light-emitting diodes. *Nanoscale Adv* **4**, 904–910 (2022).
256. Mude NN, Yang HI, Thuy TT et al. Performance enhancement by sol-gel processed Ni-doped ZnO layer in InP-based quantum dot light-emitting diodes. *Org Electron* **112**, 106696 (2023).
257. Bai JY, Hu HL, Yu YS et al. Achieving high performance InP quantum dot light-emitting devices by using inkjet printing. *Org Electron* **113**, 106705 (2023).
258. Wang YK, Wan HY, Xu J et al. Bifunctional electron-transporting agent for red colloidal quantum dot light-emitting diodes. *J Am Chem Soc* **145**, 6428–6433 (2023).
259. Heo D, Chang JH, Shin D et al. Modified zinc magnesium oxide for optimal charge‐injection balance in InP quantum dot light‐emitting diodes. *Adv Opt Mater* **11**, 2202256 (2023).
260. Huang P, Liu XN, Jin GY et al. Deep-red InP core-multishell quantum dots for highly bright and efficient light-emitting diodes. *Adv Opt Mater* **11**, 2300612 (2023).
261. Nasrud D, Fawad S, Sajid H et al. Solution processed light emitting diode based on InP quantum dots with hybrid emissive layer. *J Phys Conf Ser* **2613**, 012001 (2023).
262. Jeon Y, Sim S, Shin D et al. All-solution-processed top-emitting InP quantum dot light-emitting diode with polyethylenimine interfacial layer. *Adv Elect Mater* **10**, 2400195 (2024).
263. Wang SB, Yang WY, Li Y et al. Efficient and long lifetime red InP-based QLEDs enabled by simultaneously improved carrier injection balance and depressed leakage. *Adv Opt Mater* **13**, 2402677 (2025).
264. Wan HY, Jung ED, Zhu T et al. Nickel oxide hole injection layers for balanced charge injection in quantum dot light-emitting diodes. *Small* **20**, 2402371 (2024).
265. Li QY, Cao S, Bi YH et al. Dipole modulation engineering enhances structural order of PEDOT: PSS for efficient and stable InP-based QLEDs. *ACS Appl Mater Interfaces* **16**, 70728–70736 (2024).
266. Wang H, Zhao LJ, Bao X et al. Efficiency enhancement of InP-based quantum dot light-emitting diodes by introducing a phosphorescent-dye sensitizer in a hole transport layer. *ACS Photonics* **12**, 1999–2006 (2025).
267. Lu XF, Meng FY, Chen XH et al. Efficient InP-based quantum dot light-emitting diodes using LiMgZnO electron transport materials. *ACS Appl Nano Mater* **8**, 6877–6885 (2025).
268. Li H, Zhang JY, Wen W et al. Highly efficient light-emitting diodes via self-assembled InP quantum dots. *Nat Commun* **16**, 4257 (2025).
269. Bae Y, Lee J, Lee K et al. Charge generation junction for efficient hole injection in InP-based quantum dot light-emitting diodes. *ACS Appl Electron Mater* **7**, 4493–4500 (2025).
270. Ali A, Rehman F, Das T et al. Experimental and first-principles analyses of oxidative defect removal in eco-friendly InP quantum dot synthesis via *in situ* HF etching. *Chem Eng J* **511**, 162134 (2025).
271. Hou RX, Hu RR, Zhang XT et al. Simultaneous achievement of high efficiency and brightness at low bias in red InP/ZnSe/ZnSeS/ZnS quantum dot light-emitting diodes. *J Power Sources* **632**, 236355 (2025).
272. Yang XY, Divayana Y, Zhao DW et al. A bright cadmium-free, hybrid organic/quantum dot white light-emitting diode. *Appl Phys Lett* **101**, 233110 (2012).
273. Lim J, Park M, Bae WK et al. Highly efficient cadmium-free quantum dot light-emitting diodes enabled by the direct formation of excitons within InP@ZnSeS quantum dots. *ACS Nano* **7**, 9019–9026 (2013).
274. Ippen C, Greco T, Kim Y et al. Color tuning of indium phosphide quantum dots for cadmium-free quantum dot light-emitting devices with high efficiency and color saturation. *J Soc Inf Disp* **23**, 285–293 (2015).
275. Wang HC, Zhang H, Chen HY et al. Cadmium-free InP/ZnSeS/ZnS heterostructure-based quantum dot light-emitting diodes with a ZnMgO electron transport layer and a brightness of over 10 000 cd m^{-2}. *Small* **13**, 1603962 (2017).
276. Kuo TR, Hung ST, Lin YT et al. Green synthesis of InP/ZnS core/shell quantum dots for application in heavy-metal-free light-emitting diodes. *Nanoscale Res Lett* **12**, 537 (2017).
277. Kim Y, Heyne B, Geßner A et al. P-110: efficient InP-based quantum dot light emitting diodes utilizing a crosslinkable hole transport layer. *SID Symp Dig Tech Pap* **49**, 1625–1628 (2018).
278. Moon H, Lee W, Kim J et al. Composition-tailored ZnMgO nanoparticles for electron transport layers of highly efficient and bright InP-based quantum dot light emitting diodes. *Chem Commun* **55**, 13299–13302 (2019).
279. Lee T, Hahm D, Kim K et al. Highly efficient and bright inverted top-emitting InP quantum dot light-emitting diodes introducing a hole-suppressing interlayer. *Small* **15**, 1905162 (2019).
280. Shin DW, Suh YH, Lee S et al. Waterproof flexible InP@ZnSeS quantum dot light-emitting diode. *Adv Opt Mater* **8**, 1901362 (2020).

281. Iwasaki Y, Motomura G, Ogura K et al. Efficient green InP quantum dot light-emitting diodes using suitable organic electron-transporting materials. *Appl Phys Lett* **117**, 111104 (2020).
282. Li D, Feng JW, Zhu YQ et al. Enhanced efficiency of top-emission InP-based green quantum dot light-emitting diodes with optimized angular distribution. *Nano Res* **14**, 4243–4249 (2021).
283. Wang YM, Wu QQ, Wang L et al. Boosting the efficiency and stability of green InP quantum dot light emitting diodes by interface dipole modulation. *J Mater Chem C* **10**, 8192–8198 (2022).
284. Gao PL, Zhang Y, Qi P et al. Efficient InP green quantum-dot light-emitting diodes based on organic electron transport layer. *Adv Opt Mater* **10**, 2202066 (2022).
285. Kim J, Hong A, Hahm D et al. Realization of highly efficient InP quantum dot light - emitting diodes through In-depth investigation of exciton-harvesting layers. *Adv Opt Mater* **11**, 2300088 (2023).
286. Li LF, Luo YN, Wu QQ et al. Efficient and bright green InP quantum dot light-emitting diodes enabled by a self-assembled dipole interface monolayer. *Nanoscale* **15**, 2837–2842 (2023).
287. Wu QQ, Wang L, Cao F et al. Bridging chloride anions enables efficient and stable InP green quantum-dot light-emitting diodes. *Adv Opt Mater* **11**, 2300659 (2023).
288. Zhang TQ, Zhao FQ, Liu P et al. Understanding and hindering the electron leakage in green InP quantum-dot light-emitting diodes. *Adv Photonics Res* **4**, 2300146 (2023).
289. Shin S, Gwak N, Yoo H et al. Fluoride-free synthesis strategy for luminescent InP cores and effective shelling processes via combinational precursor chemistry. *Chem Eng J* **466**, 143223 (2023).
290. Truong Thi T, Mude NN, Vergineya SN et al. Optimization the potential of solution process fluorine passivated zinc oxide electron transport layer for stable InP-quantum dot light emitting diodes. *Org Electron* **132**, 107098 (2024).
291. Wang LS, Fan Z, Liu DY et al. Modified charge injection in green InP quantum dot light-emitting diodes utilizing a plasma-enhanced NiO buffer layer. *J Phys Chem C* **128**, 3985–3993 (2024).
292. Lin OY, Bian YY, Chen J et al. *In-situ* etching assisted synthesis of high performance green InP-based quantum dots for QLEDs. *Nano Res* **18**, 94907735 (2025).
293. Yuan CW, Wan Q, Liao XR et al. Dual-mode strain relief via zinc acetate enables high-efficiency InP quantum dot light-emitting diodes. *Angew Chem* **137**, e202509765 (2025).
294. Lee W, Lee C, Kim B et al. Synthesis of blue-emissive InP/GaP/ZnS quantum dots via controlling the reaction kinetics of shell growth and length of capping ligands. *Nanomaterials* **10**, 2171 (2020).
295. Tan YZ, Zhang WD, Xiao XT et al. Enhancing hole injection by electric dipoles for efficient blue InP QLEDs. *Appl Phys Lett* **119**, 221105 (2021).
296. Kim Y, Yang K, Lee S. Highly luminescent blue-emitting In$_{1-x}$Ga$_x$P@ZnS quantum dots and their applications in QLEDs with inverted structure. *J Mater Chem C* **8**, 7679–7687 (2020).
297. Suh YH, Lee S, Jung SM et al. Engineering core size of InP quantum dot with incipient ZnS for blue emission. *Adv Opt Mater* **10**, 2102372 (2022).
298. Shen C, Zhu YQ, Tao H et al. Blue-emitting InP/GaP/ZnS quantum dots with enhanced stability by siloxane capping: implication for electroluminescent devices. *ACS Appl Nano Mater* **5**, 2801–2811 (2022).
299. Zhang WD, Tan YZ, Duan XJ et al. High quantum yield blue InP/ZnS/ZnS quantum dots based on bromine passivation for efficient blue light-emitting diodes. *Adv Opt Mater* **10**, 2200685 (2022).
300. Yang ZW, Lin GL, Bai JY et al. Inkjet-printed blue InP/ZnS/ZnS quantum dot light-emitting diodes. *Chem Eng J* **450**, 138413 (2022).
301. Jiang XJ, Zhang ZB, Fan Z et al. A double Zn and Ga modification strategy for highly efficient deep blue InP/ZnSeS/ZnS quantum dots. *ACS Appl Nano Mater* **7**, 18714–18723 (2024).
302. Zhang WD, Duan XJ, Chen L et al. Synthesis of deep blue InP quantum dots via HF etching for light-emitting diodes. *ACS Appl Electron Mater* **7**, 5061–5068 (2025).
303. Kim T, Kim SY, Lee S et al. Gallium incorporation in blue-emitting In$_{1-x}$Ga$_x$P alloy quantum dots facilitated by monomeric gallium precursors. *Inorg Chem Front* **12**, 3898–3908 (2025).

Acknowledgements

We are grateful for financial support from the National Key Research and Development Program of China [Grant No. 2022YFB3602901], Beijing Natural Science Foundation [Grant No. Z220007], the National Natural Science Foundation of China [Grant No.62574076], the National Key R&D Program of China [Grant No. 2023YFE0205000], the Zhongyuan High Level Talents Special Support Plan [Grant No. 244200510009],and the Technological Innovation 2030-Major Projects [Grant No. 2024ZD0604000].

Author contributions

A. W. Tang and F. Chen conceived the idea and initiated the project. Y. Y. Bian and Q. Li organized the contents of InP-based QDs. Y. Y. Bian and F. Chen mainly wrote this manuscript. F. Chen, C. H. Yang, H. B. Shen and A. W. Tang contributed to the discussion and the revision of the manuscript.

Competing interests

The authors declare no competing financial interests.

Published by Editorial Office of *Opto-Electronic Advance*, Institute of Optics and Electronics, Chinese Academy of Sciences.